

DESIGN AND EVALUATION OF GAMMA IMAGING SYSTEMS
OF COMPTON AND HYBRID CAMERAS

By

YUXIN FENG

A DISSERTATION PRESENTED TO THE GRADUATE SCHOOL
OF THE UNIVERSITY OF FLORIDA IN PARTIAL FULFILLMENT
OF THE REQUIREMENTS FOR THE DEGREE OF
DOCTOR OF PHILOSOPHY

UNIVERSITY OF FLORIDA

2009

© 2009 Yuxin Feng

To my wife, my son, and my parents.

ACKNOWLEDGMENTS

I would like to express my gratitude to those who have contributed to this work. First, I would like to deeply thank my academic advisors, Professor James Edward Baciak, Jr., for his support, excellent guidance, and encouragement to complete my Ph.D. I also would like to express my thanks to my dissertation committee members: Professor Alireza Haghighat, Professor David R. Gilland, and Professor Bernard A. Mair for their careful review of my research proposal, dissertation, and thoughtful suggestions. I would like to thank Professor Rebecca Detwiler for her helpful discussion and suggestions.

In addition, I would like to thank the faculty in the University of Florida Proton Therapy Institute (UFPTI) collaboration for the Compton camera project: Professor Zuofeng Li for helpful discussion on proton therapy.

I enjoyed the wonderful time with my former and current lab-mates: Lintereur, Azaree and Victoria Spring Cornelison who have read my manuscripts and provided helpful suggestions and corrections.

Most importantly, I would like to thank my parents and all of my family for their unconditioned love, infinite supports, and encouragement. Without them, I would never have chance to fulfill my dream. I also thank my son, Gabriel, who fills my life with fun, bright, and happy. Finally, I would like to express my gratitude to my wife, Qiong, whose love and support made this possible.

TABLE OF CONTENTS

	<u>page</u>
ACKNOWLEDGMENTS	4
LIST OF TABLES	7
LIST OF FIGURES	8
ABSTRACT	12
CHAPTER	
1 INTENTION AND OBJECTIVES.....	14
2 COMPTON CAMERA.....	22
Compton Scattering	25
Efficiency.....	27
Angular Uncertainty	31
Geometrical Uncertainty	31
Energy Resolution	34
Doppler Broadening	37
Optimization of Geometries	38
3 CODED APERTURES.....	40
Aperture Patterns	41
Optimum and Simple Configurations.....	45
Geometries Design.....	47
Active Coded Aperture Cameras	49
4 IMAGE RECONSTRUCTION ALGORITHMS	51
The Simple Back-Projection Algorithm	51
Filtered Back-Projection Algorithm	54
Iterative Approach	57
Decoding Coded Aperture Images.....	59
LABR ₃ :CE SCINTILLATION DETECTOR.....	61
Scintillation Mechanisms.....	62
Spectroscopy with LaBr ₃ :Ce Detectors	63
Timing Properties of LaBr ₃ :Ce.....	65

5	EXPERIMENT AND HARDWARE	68
	LaBr ₃ Detector	68
	Data Acquisition Hardware	69
	Experiment.....	72
	Spectroscopy.....	73
	Image	74
	Conclusions.....	78
6	DESIGNS AND SIMULATION OF HYBRID CAMERA	79
	Optimization of Compton Camera	80
	Coded Aperture.....	83
	Prototype Hybrid Gamma Camera and Simulation	85
	Discussion.....	93
	Conclusions.....	94
7	DESIGN OF A COMPTON IMAGING CAMERA FOR MEDICAL APPLICATIONS.....	95
	Introduction.....	95
	High Resolution Compton Cameras for High Energy Photons	97
	Compton Camera Approach	99
	Image Reconstruction	103
	Results and Discussion	105
	Conclusions.....	109
8	CONCLUSIONS & FUTURE WORKS	111
APPENDIX		
A	CODES FOR HYBRID CAMERA IN GEANT	115
B	CODES FOR COMPTON CAMER IN GEANT	132
C	AN EXAMPLE OF IMAGE RECONSTRUCTION CODES	148
D	AN EXAMPLE OF RESPONSE MATRIXES GENERATION CODES	152
LIST OF REFERENCES.....		160
BIOGRAPHICAL SKETCH		168

LIST OF TABLES

<u>Table</u>		<u>page</u>
5-1	Comparison of scintillation crystals.....	61

LIST OF FIGURES

<u>Figure</u>	<u>page</u>
1-1 Structure of IBIS is shown in (a) that combine coded mask on the top shown in (b) and a Compton imager composed of ISGRI and PICsIT on the bottom shown in (c).	17
2-2 The cross sections of photon interaction with LaBr_3 as function of the energy of incident photon.....	25
2-3 The Feynman diagram for the Compton scattering process.	26
2-4 Slab geometry used for numerical calculation.....	28
2-5 For a photon at 662 keV, the probability of observing a single Compton scatter event as a function of the thickness of scattering detectors.....	30
2-6 The configuration of one scattering detector and one absorbing detector.	32
2-7 Angular uncertainties as function of distance between the scattering and absorbing detectors.	33
2-8 The energy spectrum of Cs-137 observed with LaBr_3	35
2-9 The fitting of energy resolution as a function of energy.....	35
2-10 Angular uncertainty included from the uncertainty of energy measurement.	36
2-11 Comparison between Doppler broadening of Si and LaBr_3	36
2-12 Doppler broadening effects in angular uncertainty as function of scattering angle.	37
2-13 (a) The efficiency as a function of angular uncertainty, (b) angular uncertainty as a function of thickness.	38
3-1 The illustration of coded aperture cameras.	40
3-2 Fresnel zones coded aperture on the left and random pinhole on the right	41
3-3 Schematic drawings of the two types of 'optimum' configurations discussed . The left configuration is called 'cyclic.'.....	46
3-4 Schematic drawing of the 'simple' configuration . The sizes of the mask and detector are equal.....	47
3-5 SPI Mask is the tungsten alloy elements on top of the support structure	47
4-1 The geometry of a Compton scattering event.....	51

4-2	Examples of two-hit event mapped onto hemisphere.....	52
4-3	The image of a beam of photons one with energy of 662 keV at a polar angle of 30° and an azimuthal angle of $\varphi = 40^\circ$	53
4-4	The two coincident hits in Compton camera.....	58
5-1	LaBr ₃ Crystal and its Hexagonal structure of LaBr ₃	62
5-2	a) Binary V_k and electron diffusion, and b) STE migration in the scintillation process.....	63
5-3	The energy resolution at 662 keV as function of temperature on left and BrillanCe 380 detector on right.....	64
5-4	The energy spectrum of ²² Na.....	64
5-5	The fitting of energy resolution as a function of energy.....	65
5-6	Background spectrum measured with BrillanCe 380 LaBr ₃ detector in 10 hours.....	66
5-7	Temperature dependence of LaBr ₃ :5% Ce ³⁺ scintillation decay curves. The solid curves are drawn to guide the eye and are not fitted curves [61]......	66
6-1	The sketch of experimental setup.....	68
6-2	²³² Th Spectra from LaBr ₃ :Ce (upper) and NaI(Tl) (lower).....	69
6-3	The picture of NI PCI-MIO-16E-1 card and block diagram.....	70
6-4	SCB-68 printed circuit diagram.....	71
6-5	The configuration mimicked in the experiment with two detectors. The center detector was the primary scattering detector.....	73
6-6	The energy spectra of coincident events in the two detectors.....	74
6-7	The image reconstructed with back-projection method on the top and the zoomed in image on the bottom.....	75
6-8	The calculated efficiency map of the system as function of the original position of incident photons.....	77
6-9	The reconstructed image with EML iterative method.....	78
7-1	The configuration of the hybrid gamma camera used for evaluation with Monte Carlo simulation.....	82

7-3	The shadows of the scattering detectors on the 10 x 10 array of absorbing detectors when the camera was centered at (0, 0, 0) and irradiated by a point source at (250cm, 0 cm, 1500 cm).	85
7-4	The image reconstructed by decoded the shading pattern on the bottom layer resolved with the detector array approach. On the top it was obtained from 2×10^4 events at 662 keV; on the bottom layer resolved with the detector array approach form 2×10^5 events at 662 keV.....	86
7-5	The image reconstructed by decoded the shading pattern from 2×10^4 events at 100 keV.....	87
7-6	The reconstructed image of the same two sources at 662 keV with back-projection method implemented in Compton camera approach.	87
7-7	The image reconstructed with back-projection method is on the left. The image on the right is obtained with filtered back-projection method.....	90
7-8	The efficiency of the hybrid camera as function of the original location of incident photons with 100 keV on XY plan at $z = 1500$ cm.....	92
7-9	The reconstructed image of 100 keV photons from two-hit events.....	92
8-1	The comparison the dose delivery with proton and photon beams. Adapted from http://www2.massgeneral.org/cancer/about/providers/radiation/proton/principles.asp	96
8-2	The energy spectrum of the prompt gamma emission induced by 200 MeV proton beam in water.....	96
8-3	The configuration of the Compton camera is on the left. The sizes of detectors and the pixel are on the right.	98
8-4	The efficiency of single Compton scattering as function of thickness of the detector.	99
8-5	The relative efficiency as function of scattering angle for LaBr_3 Compton imaging system.	100
8-6	The angular uncertainty induced from positioning as function of the distance between detectors.....	101
8-7	The angular uncertainty induced from uncertainty in measurement of energies as function of scattering angle.....	102
8-8	The angular uncertainty induced from Doppler broadening.....	102
8-9	The point source and the Camera setup for simulation on the left. The point source reconstructed with OSEML from two-hit events on the right.	105

8-10	The map of the Compton camera as function of the original location of incident photons on XY plan at $z=15$ cm.	106
8-11	3-D image reconstruction of a point source with OSEML algorithm. The different slices correspond to different depths.....	107
8-12	The converge seed of OSEML algorithm increased with decreasing of the size of subset.....	107
8-13	The images reconstructed with OSEML algorithm for 2×10^7 incident photons at 511 keV on the left and 2.2 MeV on the right.	108
8-14	Two orthogonal Compton cameras with the same configuration of Figure 8-4.	109

Abstract of Dissertation Presented to the Graduate School
of the University of Florida in Partial Fulfillment of the
Requirements for the Degree of Doctor of Philosophy

DESIGN AND EVALUATION OF GAMMA IMAGING SYSTEMS
OF COMPTON AND HYBRID CAMERAS

By

Yuxin Feng

May, 2009

Chair: James E. Baciaak
Major: Nuclear Engineering Sciences

Systems for imaging and spectroscopy of gamma-ray emission have been widely applied in environment and medicine applications. The superior performance of $\text{LaBr}_3:\text{Ce}$ detectors established them as excellent candidates for imaging and spectroscopy of gamma-rays. In this work, Compton cameras and hybrid cameras with a two-plane array of $\text{LaBr}_3:\text{Ce}$ detectors, one for the scattering and one for the absorbing detector arrays were designed and investigated.

The feasibility of using LaBr_3 in Compton cameras was evaluated with a bench top experiment in which two $\text{LaBr}_3:\text{Ce}$ detectors were arranged to mimic a Compton camera with one scattering and eight absorbing detectors.

In the hybrid system the combination of the imaging methods of Compton and coded aperture cameras enables the system to cover the energy range of approximately 100 keV to a few MeV with good efficiency and angular resolution. The imaging performance of the hybrid imaging system was evaluated via Monte Carlo simulations. The image reconstruction algorithms of direct back-projections were applied for instant or real time imaging applications; this imaging system is capable of achieving an angular resolution of approximately 0.3 radians (17°). With image reconstruction algorithms of Expectation Maximized Likelihood, the image quality was improved to approximately 0.1 radians (or 6°).

For medical applications in proton therapy, a Compton camera system to image the gamma-ray emission during treatment was designed and investigated. Gamma rays and X-rays emitted during treatment illustrate the energy deposition along the path of the proton beams and provide an opportunity for online dose verification. This Compton camera is designed to be capable of imaging gamma rays in 3D and is one of the candidates for imaging gamma emission during the treatment of proton therapy beside of the approach of positron emission tomography.

In order to meet the requirement for spatial resolution of approximately 5 mm or less to meaningfully verify the dose via imaging gamma rays of 511 keV to 2 MeV, position sensing techniques with pixilated LaBr_3 (Ce) crystal were applied in each detector. The pixilated LaBr_3 (Ce) crystal was used in both the scattering and absorbing detectors. Image reconstruction algorithms of OS-EML were applied to obtain 3D images.

CHAPTER 1 INTENTION AND OBJECTIVES

Radiation detection and measurement have many applications in nondestructive diagnosis, radiology, radiation therapy, etc. The Gamma camera is one of the most important instruments that has the capability of spatially resolving gamma-ray sources. Usually, gamma camera performance is evaluated based on spatial resolution, energy resolution, time resolution, and efficiency. However, a camera capable of performance that is suitable for all applications is not practical due to limitations such as technique and budget. Therefore, it is critical to design gamma cameras according to a particular application.

Historically, imaging techniques employ straight-line ray optics. One example of an imaging technique that uses straight-line ray optics is the grazing incidence reflection approach, which has been applied to image low energy x-rays in ASCA and Chandra [1, 2]. However, this approach is infeasible for photons above approximately 20 keV due to the penetration power of higher energy gamma-rays. There are two alternative collimation approaches for imaging high energy photons: mechanical collimation and electronic collimation. Mechanical collimation involves integrating collimators with detectors to generate a spatially differential response [3]. These alternative techniques are referred to as multiplexing techniques. One common signature of multiplexing techniques is that the direction of the incoming rays is modulated (or coded) spatially or temporally before detection. The image of the source is reconstructed by decoding the observation after detection.

Multiplexing techniques can be further divided in two classes: those based on temporal and those on spatial multiplexing [3]. A simple example of temporal multiplexing is the scanning collimator that was used in The Large Area Counter (LAC) of the Japanese X-ray satellite Ginga

[4]. Examples of spatial multiplexing techniques are pinholes or multi-pinhole collimation in small animal SPECT, and coded apertures in Gamma-ray telescopes.

The spatial multiplexing techniques can be divided into two subclasses. In the first subclass, two or more collimator grids, widely separated, are placed in front of a detector. In the second subclass, one or more arrays of opaque and transparent elements are placed in front of a detector. It is difficult to achieve both high resolution and high efficiency with the first subclass of collimators because the thick collimators and septals required to attenuate the gamma-rays lead to low efficiency and heavy weight. Instruments of the second subclass are referred to as 'coded-aperture systems' these systems improve efficiency while preserving spatial resolution in the middle energy range (around a few hundreds of keV). However, coded-aperture systems still suffer from the high penetration power of gamma-rays of a few MeV.

The second approach, the "electronic collimator", utilizes the relationship between the direction of incident photons and the properties of events with multi-coincident hits. Two typical examples of electronic collimation systems are positron emission tomography (PET) and the Compton camera. In PET, a pair of coincident hits is attributed to two 511 keV photons from an annihilation event that are emitted in opposite directions. The line connecting the positions of the pair indicates the location of annihilation. The second example of electronic collimation is the Compton camera, in which the direction of an incident photon is derived from the measurements of Compton scattering events. With the measured positions of Compton scattering and absorption of the scattered photon as well as the energies of the recoil electron and scattered photon, the direction of the incident photon can be constrained on the surface of a cone. This is based on the Compton relationship between the scattering angle and the energies of the incident and scattered photons. Compton camera and coded aperture systems have been successfully used

in gamma/x-ray astrophysics to resolve celestial sources from a few hundred keV to a few MeV. However, systems for nuclear medicine, industry, and homeland security applications are still being developed.

Historically, high energy astrophysics is one of the areas where Compton cameras have been well developed. One of the typical examples of Compton telescopes used in astrophysics is the imaging Compton telescope (COMPTEL) on board the Compton Gamma-Ray Observatory (CGRO) [5]. The Compton telescope utilizes Compton events within two layers of gamma-ray detectors to reconstruct an image of a gamma-ray source in the energy range 1 to 30 MeV. The telescope has a wide field of view of 60° , angular resolution of $1^\circ - 3^\circ$, and energy resolution of $5\% - 10\%$. COMPTEL accomplished a major break through in gamma-ray astronomy.

Following the successful mission of CGRO, new Compton telescopes have been developed with more advanced techniques and higher levels of performance than that of COMPTEL, such as the Imager on Board Integral Satellite (IBIS). IBIS is composed of two detector layers (ISGRI and PICsIT) on board the International Gamma Ray Astrophysics Laboratory (INTEGRAL) [6], as seen in Figure 1-1. In addition, IBIS is a hybrid camera, integrating coded aperture and Compton imaging. IBIS was optimized for high-angular resolution ($12'$), a wide field of view (FOV = $29^\circ \times 29^\circ$), and moderate energy resolution point source imaging. ISGRI is a low-energy detector made of CdTe, and it operates in the energy range of 15 keV – 1 MeV. PICsIT is a high-energy detector made of CsI which operates in the energy range of 175 keV – 10 MeV [6]. The hybrid design allows IBIS to achieve the desired performance level over a broad range of energy: 15 keV to 10 MeV. The hybrid design takes advantage of higher efficiency and superior angular resolution of Compton cameras compared to conventional gamma cameras with mechanical collimators [6]

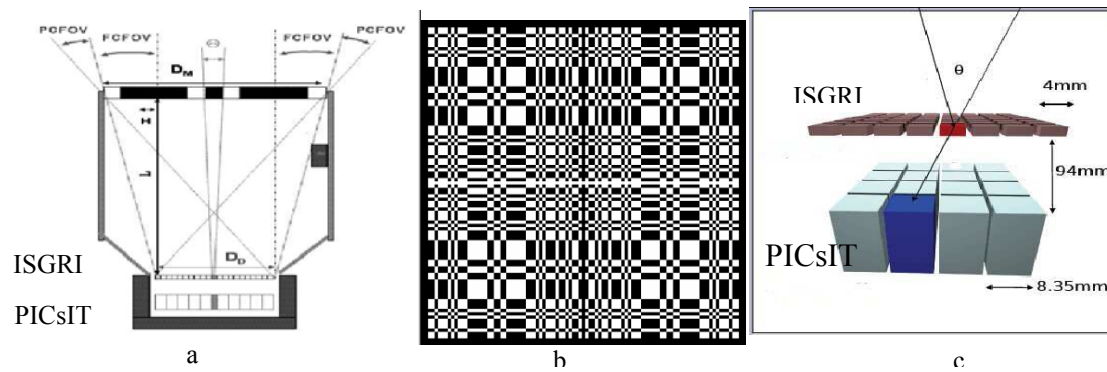


Figure 1-1. Structure of IBIS is shown in (a) that combine coded mask on the top shown in (b) and a Compton imager composed of ISGRI and PICsIT on the bottom shown in (c).

Without mechanic collimation, the Compton camera offers a wide field of view and high efficiency in the collection of photons with the capability of resolving directions of incident photons. Compton cameras have potential uses in nuclear medicine applications, such as SPCT and PET. In order to take advantage of high efficiency, high resolution, and high energy coverage in Compton cameras, Todd and Nightingale in 1974 proposed the first Compton imaging system for the possible applications in nuclear medicine [7]. Since 1974, the developments in position sensing techniques have provided opportunities for inventive designs such as that in Singh's group, CIMA Collaboration, and others. Singh's group evaluated and designed a Compton camera with pixelated germanium as the scattering detector and a conventional Anger camera as the absorbing detector [8]. The scattering detector was built by Pehl's group [9]. CIMA Collaboration designed and constructed C-SPRINT Compton Camera by using a silicon pad as a scattering detector and NaI as an absorbing detector [8]. Furthermore, a benchtop module for very high resolution small animal Compton-PET was constructed with silicon pads and BGO, by CIMA Collaboration [8]. Another novel design of high resolution Compton enhanced PET was proposed by Zaidi and his colleagues [10]. Two key components in

Zaidi's design are a matrix of long scintillation crystals and an array of hybrid of photon detectors which enhances the efficiency by reconstructing a significant fraction of Compton events within the crystals. However, it is still necessary to optimize Compton imaging systems to the level of performance suitable for clinic applications due to limited efficiency in observing single Compton events and uncertainty in the determination of scattering angle. In order to increase the efficiency in observing single Compton events, the approach of stacked multiple layers has been investigated and applied [11]. Tracking recoiled electrons in Compton scattering has also been explored as a method to reduce the uncertainty in the determination of the scattering angle [12].

For applications in industry, environment, and homeland security, imaging of gamma-rays with moderate angular resolution, about 0.3 radians, and high sensitivity is desired for the energy range of several hundred keV to a few MeV. The Compton camera is a possible approach due to its high efficiency and wide field of view. For example, the Raging Compton Camera (RCC) was proposed and investigated by Martin and his colleagues [13]. In RCC, a segmented HPGe with 4x4 planar array detectors was used as the scattering detector while an array of NaI scintillation detectors served as the absorbing detectors. However, the efficiency of this design is low and its size is too large.

The progress in the techniques for locating interactions in 3-D has brought new opportunities to improve the performance of Compton imaging systems. Resolved interaction locations and energy deposition at each interaction location allows observation of the Compton events (including recoil electrons and scattered photons in Compton scattering) within one detector which significantly increases the relative efficiency. For example, the Compton camera has been designed with the room temperature semiconductor CdZnTe with 3-D position sensing

[14]. High energy resolution of 1-2% was achieved with single and double hit events. The angular resolution of this system was about 12° after the image was reconstructed with Maximum Likelihood Expectation Maximization (MLEM) [15]. In order to increase the efficiency, a system with a 3-D array of CdZnTe detectors has been investigated [16]. Currently, the cost of this system is too high for wide spread application in industry, environment, and homeland security. However, a high efficiency and affordable system of gamma imaging is still in high demand.

With newly developed large scintillation crystals of high atomic number, such as LaBr₃, and optimized designs, an affordable system with high efficiency and moderate angular resolution is possible over a broad range of energies. This dissertation provides a design for a hybrid gamma-ray imaging system that integrates Compton imaging and coded aperture imaging approaches to achieve high efficiency and moderate angular resolution in a broad energy range from several hundred keV to a few MeV by using LaBr₃ detectors. Without using expensive and complicated position sensing techniques, LaBr₃ scintillation detectors were selected as both scattering and absorbing detectors. LaBr₃ scintillation detectors have been recently developed with better energy resolution and higher efficiency than NaI detectors with the same geometry. The fast decay of scintillation in LaBr₃ crystals reduces dead time and random coincident events in Compton camera applications.

The good energy resolution of the detectors is appreciated not only for the identification of isotopes, but also for improving the angular resolution of the system. The angular uncertainty in a Compton camera depends on the precision of the determination of the interaction position and the energy deposition. LaBr₃ (Ce) scintillation detectors have been fine-tuned to achieve energy resolution of less than 3% at 662 keV [17] and fast decay (16 ns) [18]. These attributes have

made it a good candidate for both the scattering and absorbing detectors in Compton imaging systems [19].

In the designed hybrid gamma camera presented in this work, events with two coincident hits are used for Compton imaging while single hit events are utilized for coded aperture imaging. A two hit event is defined as any two of the LaBr_3 detectors being triggered coincidentally within the time resolution. The camera has a two-plane configuration and by changing the sizes of the LaBr_3 detectors and the distance between the detectors, the camera can achieve the highest efficiency for a given angular uncertainty or the smallest angular uncertainty for a given efficiency. The probability of a single Compton scattering, and angular uncertainty, are functions of the thickness of the LaBr_3 crystals, the distance between the scattering and absorption planes, and the spacing between the detectors, which are calculated numerically.

In this dissertation, the principles of the Compton imaging system are reviewed in Chapter 2. Optimization method for the Compton cameras is also presented also in Chapter 2. Coded aperture imaging theory is reviewed Chapter 3. The energy resolution and timing properties of LaBr_3 detectors are reviewed in Chapter 4, where the results of spectroscopy of several isotopes are also presented. The image reconstruction algorithms are reviewed in Chapter 5. The experimental setup and hardware used are summarized in Chapter 6. A prototype and simple simulation of the hybrid Compton and coded aperture imaging system is presented in Chapter 7 where the performance of the designed camera was evaluated based on Monte Carlo simulations in Geant4. In Chapter 8 a novel design of Compton cameras is presented which achieved a high spatial resolution suitable for medical applications, such as imaging gamma emission during photon therapy treatment. The lessons learned and the evaluations of this hybrid imaging system

are summarized in Chapter 8. In Chapter 9 the future work and major challenges are briefly discussed.

CHAPTER 2 COMPTON CAMERA

Detection of gamma-rays is an important tool in identifying their emitters because they carry the finger prints from nuclei, characteristic energy lines given off in nuclear decay or photo-nuclear reactions. Also, gamma-rays generally have higher energies than characteristic x-rays, and thus are more observable through shielding barriers. Emission imaging systems utilizing gamma-ray imaging have both high angular resolution and high efficiency, and are in great demand for medical, environmental, and homeland security applications to locate and identify radiation sources.

Imaging systems with mechanical collimators, such as pinholes in small animal SPECT, parallel holes in SPECT, and coded apertures in telescopes, have been well developed for imaging X/ γ -ray emissions. However, it is difficult to infer the directions of incident gamma-rays as compared to x-rays with these systems, due to the higher energy and lower modulation levels of gamma-rays as compared to lower energy X-rays in these systems.. For these mechanical collimation systems, the image quality and efficiency decrease with increasing gamma ray energy. In order to image high energy gamma rays with high efficiency and angular resolution, electronic collimation methods have been developed, such as timing coincidence techniques used in pair emission tomography (PET) systems and Compton camera systems.

In Compton cameras, the measurement of the position and deposited energy of two or more coincident interactions constrain the source onto a conic surface [20]. Since there is no attenuation material between source and detectors, electronic collimation systems have been expected to achieve a higher efficiency and superior angular resolution compared to conventional gamma cameras with mechanical collimators in the energy range of a few hundred keV to a few MeV. The Compton imaging approach has been used extensively for applications of astrophysics

[21] and nuclear medicine [22, 23, and 24]. In these the application, the detector system geometries are optimized to address the issues of limited efficiency in observing single Compton events and uncertainty in determination of the scattering angle, e.g. [25].

This angular uncertainty depends on the precision of the interaction locations and the deposited energy measurements. Therefore, detectors with high resolution in energy and space are needed to build Compton imaging systems with high angular resolution. $\text{LaBr}_3(\text{Ce})$ scintillator crystals provide a good energy resolution of less than 3% at 662 keV [26]. Additionally, with its higher atomic number and density as compared to Si, LaBr_3 may allow us to build higher efficiency Compton cameras. A narrow coincident time-window is also achievable because of its short decay time (16 ns) [27]. Above all, $\text{LaBr}_3(\text{Ce})$ is a good candidate for both the scattering and absorbing detectors for Compton cameras.

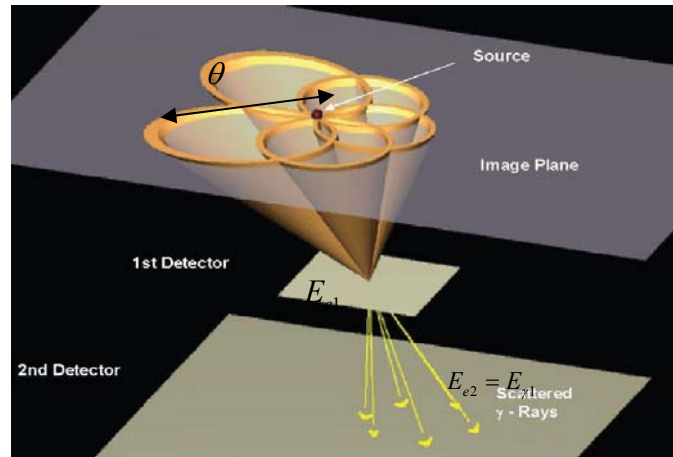


Figure 2-1. Illustration of the principle of a Compton Camera

In this dissertation, we investigate the geometries of a Compton imaging system with a two-plane configuration; parameters include the sizes of detector, the distance between scattering and absorbing planes, and the spacing between detectors in the same plane. We generated a database of LaBr_3 detector configurations to optimize the efficiency and angular uncertainty for Homeland Security and medical physics applications, based on the numerical calculations of the

probabilities of single Compton scattering and the angular uncertainty induced from uncertainties in interaction location, energy measurement, and Doppler broadening.

In this Chapter, we investigate the impact of the geometry, configuration, and detection material on the efficiency and angular uncertainty of Compton camera, based on the principles of a Compton camera, as illustrated in Figure 2-1 and stated in equations 2.1 and 2.2. The principle of Compton imaging is based on the Compton relationship

$$E_{\gamma_1} = \frac{E_{\gamma_0}}{1 - \frac{E_{\gamma_0}}{m_0 c^2} (1 - \cos(\theta))} \quad (2.1)$$

$$\cos(\theta) = 1 - m_0 c^2 \left[\frac{1}{E_{\gamma_1}} - \frac{1}{E_{\gamma_0}} \right] \quad (2.2),$$

$$E_{\gamma_0} = E_{\gamma_1} + E_{e_1}$$

where E_{γ_0} is the energy of the incident photon; E_{γ_1} is the energy of the scattered photon; E_{e_1} is the energy of the recoil electron; θ is the scattering angle with respect to the direction of the incident photon, m_0 is the rest mass of the electron; c is the speed of light. Based on eq. (2.2) the direction of an incident photon can be constrained on the surface of a cone if E_{γ_1} and E_{e_1} are measured. The axis of the cone is indicated by a line extended from the location of Compton scattering to the position of the first interaction of the scattered photon. The half angle of the cone is the scattering angle θ .

The efficiency of the Compton camera is determined by the efficiency of observing single Compton events; this is the probability of a Compton scattering event and the chance of resolving this event. The probability of the Compton scattering event depends upon the cross section of Compton scattering in materials and is a function of the energies of incident and scattered photons and the scattering angle. In general, Compton imaging is an efficient approach

for imaging photons above a few hundred keV to a few MeV, the energy region where Compton scattering is dominant for LaBr₃, as shown in Figure 2-2.

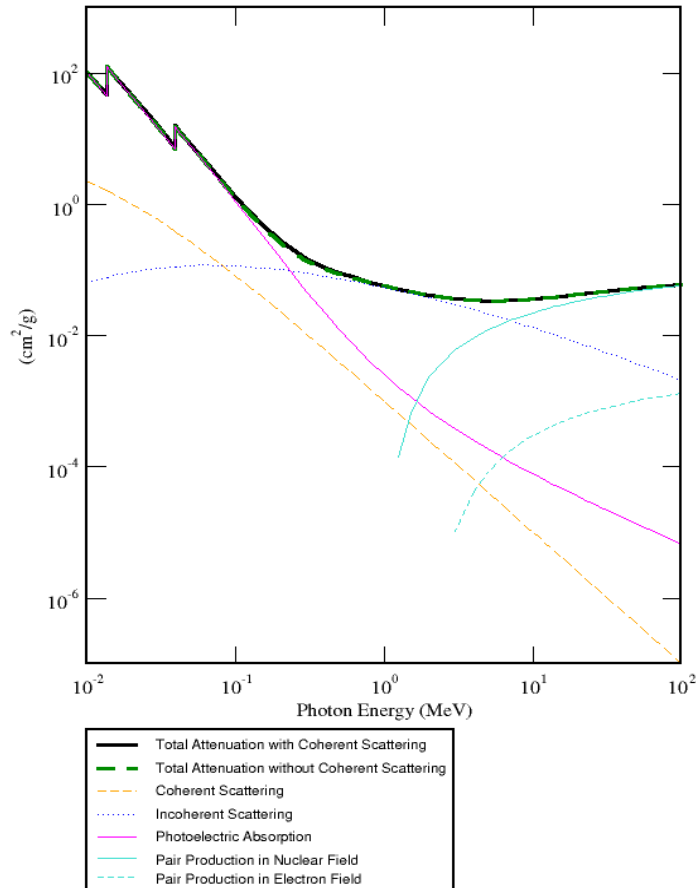


Figure 2-2. The cross sections of photon interaction with LaBr₃ as function of the energy of incident photon. (This plot adapted from <http://physics.nist.gov/PhysRefData/Xcom/Text/XCOM.html>)

Compton Scattering

An illustration of the interaction probabilities in units of mass attenuation of primary photons interactions in LaBr₃ are shown in Figure 2-2. The figure, from the NIST XCOM website[106], shows that the primary photon interactions, i.e. photoelectric absorption, incoherent scattering, and pair production, are dominant in the energy ranges $E < 200$ keV, 300

keV $< E < 7$ MeV, and $E > 8$ MeV, respectively. The Compton scattering cross section and attenuation coefficients shown here are derived from the Klein-Nishina Equation [28]:

$$\frac{d\sigma}{d\Omega} = \frac{r_0^2}{2} \left(\frac{E_{\gamma_1}}{E_{\gamma_0}} \right)^2 \left(\frac{E_{\gamma_0}}{E_{\gamma_1}} + \frac{E_{\gamma_1}}{E_{\gamma_0}} - \sin^2(\theta) \right) \quad (2.3)$$

$$r_0 = \frac{e^2}{m_0 c^2}$$

where e is the charge of an electron and m_0 is the rest mass of the electron, θ is the photon scattering angle, and E_{γ_0} , E_{γ_1} are energies of the incident and scattered photons as stated above. This formula and the Compton relationship in eq. (2.1) use the free electron approximation (the photon scatters from a free electron) where the scattering angle and photon energy uniquely determine the energy of the scattered photon and recoil electron. However, the effects of atomic structure are needed for low photon energies and large scattering angles, conditions where the electron binding energy is comparable to the kinetic energy imparted to it by the photon.

For scattering with an atomic electron, the cross section is a function of the initial momentum of the electron and momentum exchanged through binding effects, as seen in the Feynman diagram for the Compton scattering process in Figure 2-3.

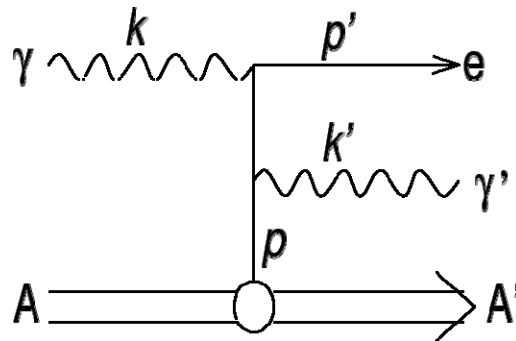


Figure 2-3. The Feynman diagram for the Compton scattering process.

The circle in the line of the incoming atom A indicates that the electron is initially bound to the atom and represents the probability that the electron with a four-momentum $p = (E_e, \vec{p}_e)$

interacts with the incoming photon with a four-momentum $K = (E_{\gamma_0}, \vec{p}_{\gamma_0})$ into a final state $e^- \gamma'$ given by $p' = (E'_e, \vec{p}'_e)$ and $K' = (E_{\gamma_1}, \vec{p}_{\gamma_1})$. If the binding energy is neglected and the electron is considered to be initially at rest, the cross section for the process is given by the Klein-Nishina formula. However, the more accurate expression for Compton scattering from a bound atomic electron, represented with the double differential cross section, is [29]:

$$\frac{\partial^2 \sigma}{\partial E_{\gamma_1} \partial \Omega} = \frac{r_0^2}{2} \frac{E_{\gamma_1}}{E_{\gamma_0} q} (1 + p_z^2)^{1/2} \left[\frac{R}{R'} + \frac{R'}{R} + 2 \left(\frac{1}{R} - \frac{1}{R'} \right) + \left(\frac{1}{R} - \frac{1}{R'} \right)^2 \right] J(p_z) \quad (2.4)$$

In what follows we use natural units, i.e., $c=1$ and $\hbar=1$. Where Ω is the solid angle (θ, φ) ;

$J(p_z) = \iint dp_x dp_y |\Psi(\vec{p})|$ is the Compton profile; $\Psi(\vec{p})$ is the wave function of bound electron;

$q = \sqrt{E_{\gamma_0}^2 + E_{\gamma_1}^2 - 2E_{\gamma_0}E_{\gamma_1} \cos(\theta)}$ is the modulus of momentum transfer vector $\vec{q} = \vec{p}_{\gamma_1} - \vec{p}_{\gamma_0}$;

$p_z = \frac{\vec{p}_{\gamma_1} \cdot \vec{q}}{q} = \frac{E_{\gamma_1}E_{\gamma_0}(1 - \cos(\theta)) - E_{\gamma_0} + E_{\gamma_1}}{q}$ is the projection of the initial momentum of the electron on the

direction momentum transfer \vec{q} ; and $R = E_{\gamma_0} \left(\sqrt{1 + q_z^2} + \frac{E_{\gamma_0} - E_{\gamma_1} \cos(\theta)}{q} \right)$, $R' = R - E_{\gamma_0}E_{\gamma_1}(1 - \cos(\theta))$.

Extensive tables of atomic and shell-wise Compton profiles for all elements have been calculated with the Hartree-Fock approximation by Biggs *et al* [30]. In Compton scattering with a bound electron, the energy of scattered photon and electron are no longer uniquely determined by the energy of initial photon and the scattering angle. The energy of scattering photons is a distribution around the energy given by Compton relationship in eq. (2.1).

Efficiency

The efficiency of a Compton camera is determined by the probability of observing single Compton scattering. For this work, this probability was calculated based on simple slab geometry of a pencil beam irradiating the center of the scattering slab, as shown in Figure 2-4.

This simplified case was used to illustrate the effect of detector thickness and distance between scattering and absorbing planes on the efficiency of observing single Compton scattering events.

For a given geometry, the efficiency of the Compton imaging system depends on the properties of the detector material used for the scatterer and absorber. With a low atomic number, silicon is a desirable material for the scattering layer in a Compton imaging system with double sided strip detectors, due to its good energy resolution, small Doppler broadening effect, and capability for position sensing [23, 31]. It is true that the photoelectric process is dominant over a broader energy-range for higher Z materials, such as LaBr_3 , compared with lower Z materials, such as Si. However, in the energy range above a few hundred keV, LaBr_3 detectors may have a higher probability for observing single Compton scattering events than Si detectors with the same thickness, due to the higher Z and higher density of LaBr_3 compared with that of Si [24]. Furthermore, at high energies, the angular uncertainty induced from Doppler broadening effects is less significant compared with those induced from the uncertainties in position and energy. Therefore, the high Z $\text{LaBr}_3:\text{Ce}$ crystal is still a good candidate for the scattering detector.

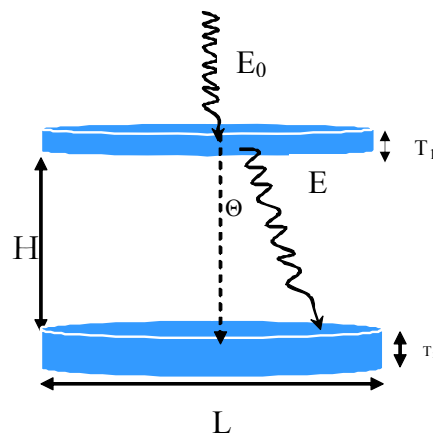


Figure 2-4. Slab geometry used for numerical calculation.

The formulas used to calculate the probabilities for observing a single Compton scattering event in a scatter (eq.1) and absorption of a scattered photon in the absorber (eq.2) are below.

$$P_{SC}(T_i, x, \Omega, E) = e^{-\mu(E)x} \frac{d\sigma_{incoh}}{d\Omega dE} N_a P_{escape} \quad (1)$$

$$P_{escape} = \begin{cases} e^{-\frac{\mu(E)(T_i-x)}{|\cos(\theta)|}} & \theta \leq \theta_1 \text{ or } \pi - \theta \leq \theta_2 \\ e^{-\mu(E)D_w} & \text{others} \end{cases}$$

$$P_{Abs}(\theta, E, T_j) \cong (1 - e^{-\frac{\mu(E)T_j}{|\cos(\theta)|}}) \sin(\theta) \quad (2)$$

$$Eff(T_i, T_j) \cong \int_0^\infty dE \int_0^{T_i} dx \int_0^{\Omega_D} d\Omega P_{SC}(T_i, x, \Omega, E) \times P_{Abs}(\theta, E, T_j) \quad (3)$$

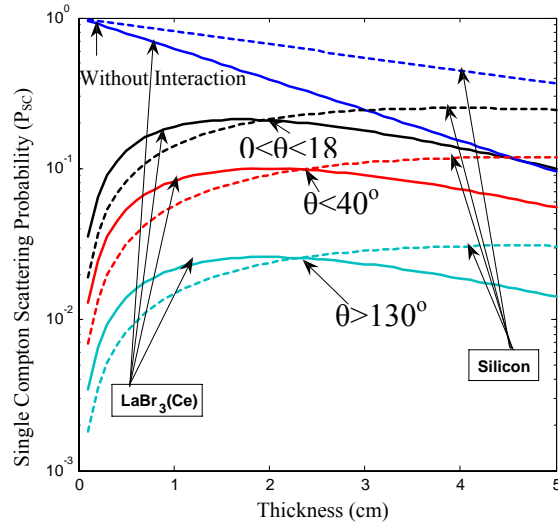
where E_0 is the energy of incident photon; $\frac{d\sigma_{incoh}}{d\Omega dE}$ is the double differential cross section for

incoherent scattering; $\theta_1 = \arctan\left(\frac{R}{T_i-x}\right)$; $\theta_2 = \arctan\left(\frac{R}{x}\right)$; μ is the attenuation coefficient;

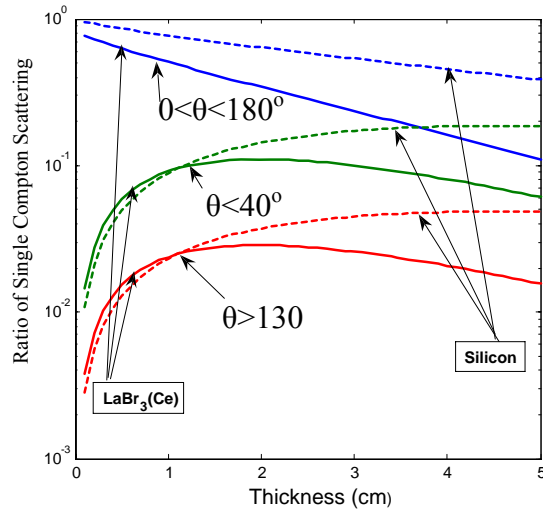
P_{SC} is the probability of single Compton scattering in the scattering plane; P_{escape} is the probability of escape from the scattering detector after a single Compton scattering event, and P_{Abs} is the probability of absorption in the absorbing plane. $Eff(T_i, T_j)$ is the efficiency of the detector system for a single Compton event that scattered on detector i and absorbed in detector j; T_i and T_j are the thickness of scattering i and absorbing detectors j, respectively; R is the radius of the detector; Ω_D is solid angle of the absorbing detector subtended by the scattering detector; D_w is the distance between the scattering location to a point on the wall of a scattering detector where the scattered photon escaped; E is the energy of the scattered photon; and x is the depth where scattering occurred.

As a result of the competition between probabilities of Compton scattering and attenuation, a maximum probability of single Compton scattering occurred at a smaller thickness in LaBr_3 than in Si, as seen in Figure 2-5a and 2-5b. Figure 2-5a shows that for a photon with energy of

662 keV the probability of single Compton scattering is higher for LaBr₃ than for Si detectors with the same thickness, below a turning point of approximately 2 cm. For the ratio of the probability



(a)



(b)

Figure 2-5. For a photon at 662 keV, the probability of observing a single Compton scatter event as a function of the thickness of scattering detectors (a); ratio of single Compton scattering probability to total interaction probability as function of the thickness (b). The range of scattering angle $0 < \theta < 180^\circ$ corresponds to all possible directions; $\theta < 40^\circ$ and $\theta > 130^\circ$ are forward and backward directions, respectively.

or single Compton scattering and the total interaction probability, the turning point is around 1.25 cm, as seen in Figure 2-5b. The figures also show that the forward single Compton scattering is dominant in a simple slab geometry case. Also, the figures show that the turning point of detector thickness increases with the energy of the incident photon. Since the energy range of interest for Homeland Security and medical imaging applications extends from a few hundred keV to a few MeV, we evaluated our design at the Cs-137 source energy of 662 keV as this corresponded to approximately the middle of the energy range.

In order to illustrate the dependence of efficiency on the scattering angle, the efficiency for forward scattering within 40° and backward scattering greater than 130° were calculated and plotted in Figure 2 as well. This shows that the efficiency is about one order of magnitude higher for forward scattering than for backward.

Angular Uncertainty

In addition to the efficiency, the angular resolution is another important parameter in evaluating the performance of Compton cameras and is closely related to the uncertainty in the determination of the scattering angle. The angular uncertainty of a Compton imaging system has three primary components.

Geometrical Uncertainty

One is the uncertainty in the locations of the initial Compton scattering event in the scatter detector, and the subsequent scatter in the absorber detector [32], as seen in Figure 2-7.

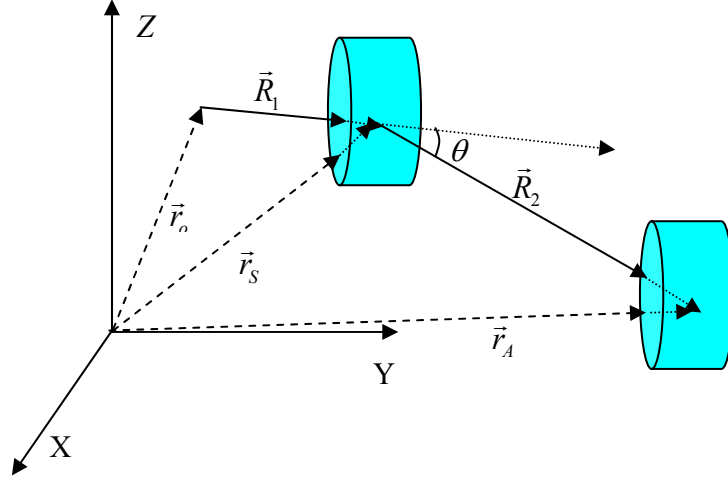


Figure 2-6. The configuration of one scattering detector and one absorbing detector.

$$\Delta\theta^2 = \Delta\theta_S^2 + \Delta\theta_A^2 \quad (2.9)$$

$$\Delta\theta_S^2 = \frac{1}{(R_1 \sin(\theta))^2} \left[\Delta\vec{r}_S \cdot (\vec{B}_1 - \alpha\vec{B}_2) \right]^2 \quad (2.10)$$

$$\Delta\theta_A^2 = \frac{1}{(R_2 \sin(\theta))^2} \left[\Delta\vec{r}_A \cdot \vec{B}_2 \right]^2 \quad (2.11)$$

$$\vec{R}_1 = \vec{r}_S - \vec{r}_o; \quad R_1 = |\vec{r}_S - \vec{r}_o|$$

$$\vec{R}_2 = \vec{r}_A - \vec{r}_S; \quad R_2 = |\vec{r}_A - \vec{r}_S|$$

$$\alpha = \frac{R_1}{R_2}$$

$$\vec{B}_1 = \vec{n}_2 - \vec{n}_1 \cos(\theta),$$

$$\vec{B}_2 = \vec{n}_1 - \vec{n}_2 \cos(\theta),$$

$$\left[\vec{P} \cdot \vec{Q} \right] \equiv (P_x Q_x)^2 + (P_y Q_y)^2 + (P_z Q_z)^2,$$

where $\Delta\theta$ is the uncertainty of the scattering angle determined by the simple back projection ;

$\Delta\vec{r}_S$ and \vec{r}_A are the uncertainty vectors in scattering and absorbing detectors, respectively; and

$\Delta\theta_S$ and $\Delta\theta_A$ are the angular uncertainties contributed from scattering and absorbing detectors.

In our calculations, we assumed that the source is infinitely far and that the position of each interaction is the center of a detector, which introduced a dependence of the angular uncertainty on the detector geometry, as shown below:

$$\Delta\theta(\theta) \approx \frac{1}{H} \sqrt{2\Delta r^2 \cos(\theta)^2 + \Delta z^2 \sin(\theta)^2 + 2\Delta r^2} \quad (2.12)$$

where H and L are the vertical and lateral distances between a scatterer and an absorber respectively; Δr and Δz are the radius and thickness of each crystal in a detector respectively; and θ is the scattering angle. For given geometries of $\Delta r = 2.5$ cm and $\Delta z = 1.5$ cm, the angular uncertainty as function of H is shown in Figure 2-7.

According to Figure 2-7, a design with a 20 cm separation between scattering and absorbing detectors can achieve 0.3 radians angular uncertainty, for the given detector dimensions stated below.

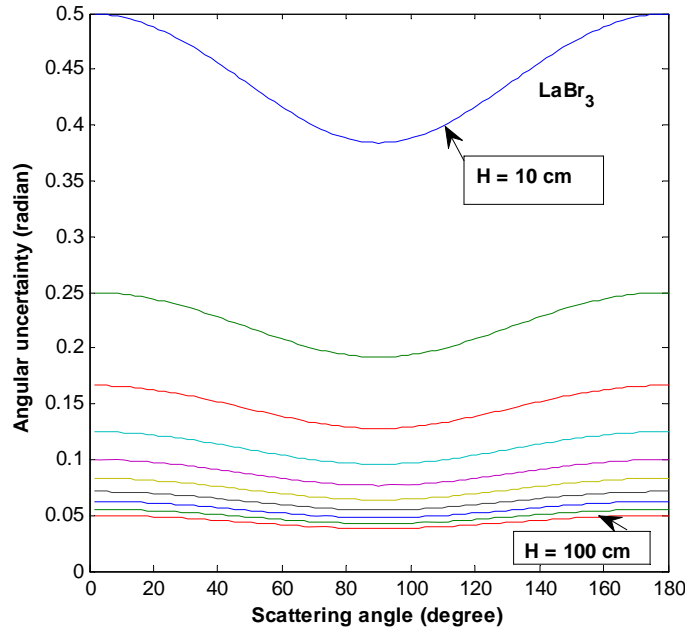


Figure 2-7. Angular uncertainties as function of distance between the scattering and absorbing detectors.

Energy Resolution

The second contribution to the angular resolution is the uncertainty in measuring the deposited energy in each detector. If the uncertainties in the measured energy deposition were ΔE_{e1} and ΔE_{e2} in the scattering and absorbing detectors respectively, the induced uncertainty in determination of the scattering angle is described below:

$$\Delta\theta = \frac{m_0 c^2}{E_{\gamma 0}^2 \sin\theta} \left\{ \Delta E_{e1}^2 + \left[\frac{E_{\gamma 0}^2}{E_{\gamma 1}^2} - 1 \right]^2 \Delta E_{e2}^2 \right\}^{1/2} \quad (5)$$

where $E_{\gamma 0}$ and $E_{\gamma 1}$ are the energies of incident and scattered photons respectively, and m_0 is the rest mass of an electron. In our investigation we used the energy resolution as the function of energy that was obtained from calibration of a BrillanCe 380 LaBr₃(Ce) detector produced by SAINT-GOBAIN company. The angular uncertainty induced is shown in Figure 2-8. It shows that angular uncertainty due to energy measurement decreases with increasing photon energy. However, it should be noted that eq. (5) is valid only for the case where the scattered photon is absorbed in the second detector. For an incident photon with unknown energy, the escape of the scattered photon from the second detector results in artifacts in the back projection image, but these could potentially be eliminated if the system response was correctly modeled using the iterative image reconstruction approach as shown in following Chapters where the iterative approach was applied. The absorbing efficiency of the scattered photon was evaluated based on the photon peak efficiency of the two-hit events in the section above.

In our investigation we derived out an empirical formula to represent the energy resolution as a function of energy based on the spectroscopy of calibrated sources, as shown below:

$$\Delta E = 8.8283 - 0.1327\sqrt{E} + 0.0195E \text{ (keV)} \quad (2.14)$$

Where, E is the energy of an incident photon. An example of the observed energy spectrum of Cs-137 is shown in Figure 2-8, the fitting of this formula with the measurement is shown in

Figure 2-9. Combining eq.(2.13) with eq.(2.14), we calculated the contribution of the energy uncertainty to the angular uncertainty, which is shown in Figure 2-10. According to this figure, the angular uncertainty of 0.3 is achievable with our current energy resolution, for photons with energies above 500 keV and at scattering angles above $\sim 10^\circ$ and below 150°

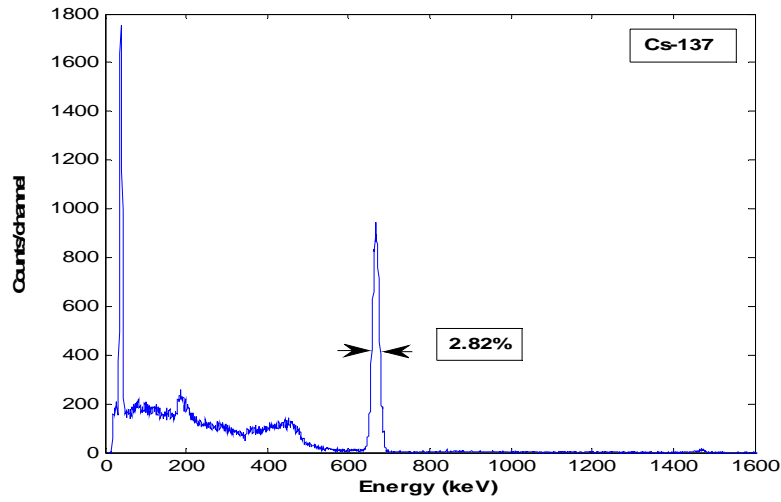


Figure 2-8. The energy spectrum of Cs-137 observed with LaBr₃.

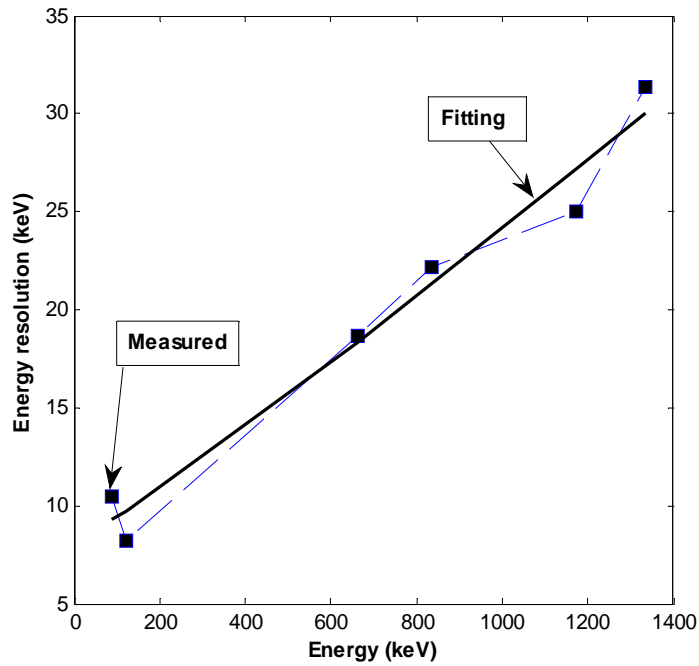


Figure 2-9. The fitting of energy resolution as a function of energy.

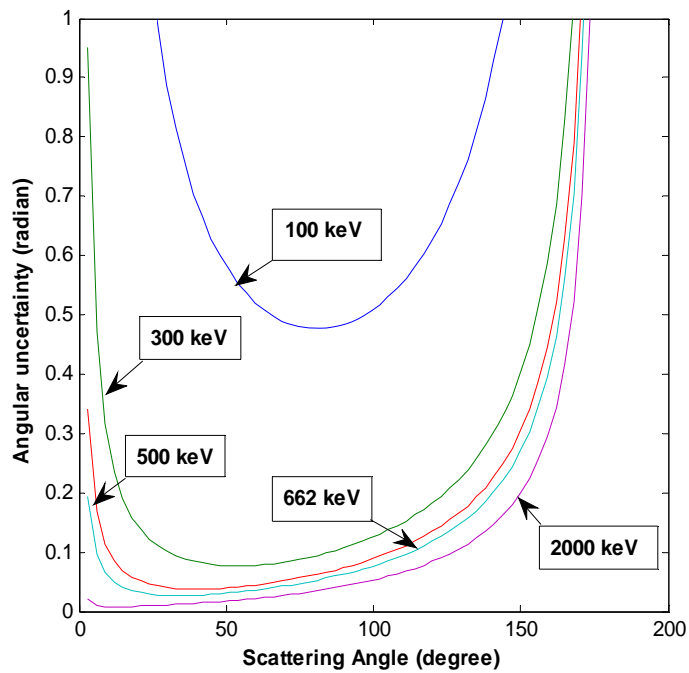


Figure 2-10. Angular uncertainty included from the uncertainty of energy measurement.

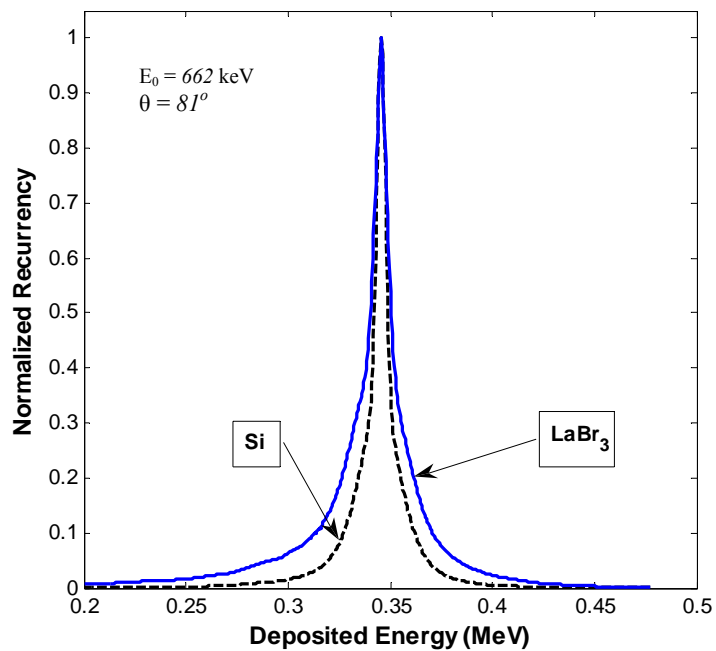


Figure 2-11. Comparison between Doppler broadening of Si and $LaBr_3$.

Doppler Broadening

The third contribution to the angular uncertainty is the Doppler broadening caused by the uncertainty in the energies and momentums of the bound electrons in atoms. As previously mentioned, due to these uncertainties, there is no longer a one-to-one relationship between the kinetic energy of the recoil electron and the scattering angle, for the scattered photon of a given energy, but rather a broadening around the energy, as seen in Figure 2-11.

Doppler broadening effects in Compton scattering therefore lead to uncertainty in the scattering angle. Based on the Compton profile calculated with the Hartree-Fock method [30], the angular uncertainty attributed to Doppler broadening was obtained based on FWHM calculations of Doppler profiles of LaBr_3 , NaI, and Si. This introduced an intrinsic limitation on the angular uncertainty of a Compton image system, as illustrated in Figure 2-12, which also shows that the angular uncertainty of Doppler broadening is less significant for *Si* than for *LaBr₃* and NaI.

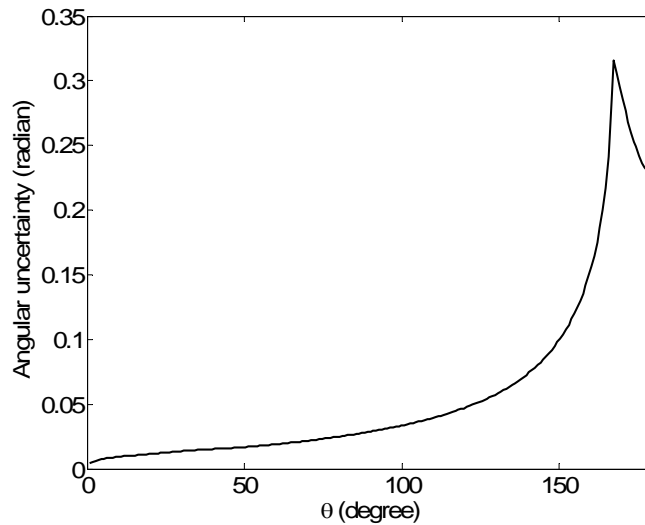


Figure 2-12. Doppler broadening effects in angular uncertainty as function of scattering angle.

The results show that an angular resolution of ~ 0.3 radians is achievable for scattering angles above 30° and below 160° s. For applications requiring high angular resolution, it is important to keep in mind that there is an angular uncertainty over the limit of ~ 0.05 radians due to the Doppler broadening effect. Scattering angles between 40° and 140° are a desired angular range for detection the scattered photons in Compton cameras for high angular resolution applications. According to Figure 2-6, Compton scattering efficiency is highest for scattering angles of 0° to 90° .

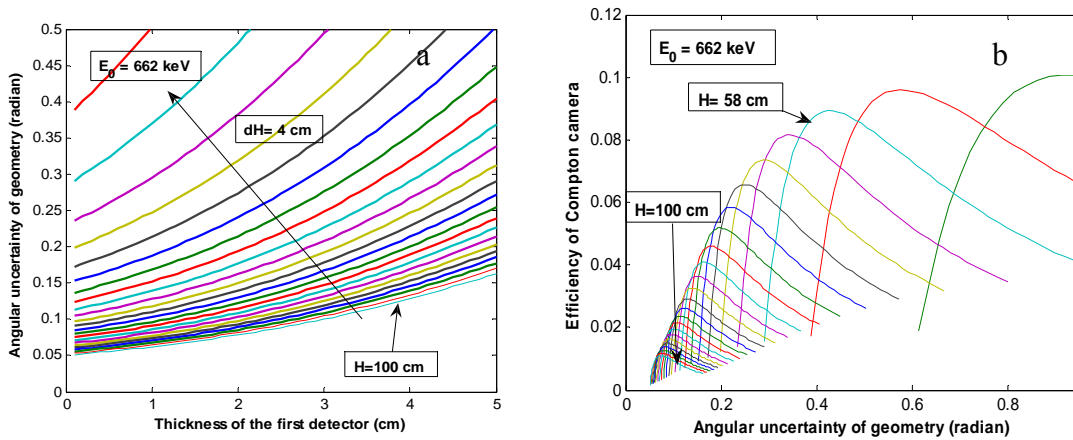


Figure 2-13. (a) The efficiency as a function of angular uncertainty, (b) angular uncertainty as a function of thickness.

Optimization of Geometries

To optimize the efficiency of a Compton imaging system for a given angular resolution, we studied the relationships between the angular uncertainty, efficiency, thickness of the crystal, and the distance separating the scattering and absorbing detectors, using numerical calculations, as shown in Figure 2-13 (a), and (b) that were obtained by averaging the scattering angles over 0° to 90° with the weighting of efficiency. The uncertainty of position in our method as described depends on the geometry of the crystal in each detector and distances between the detectors in the array, which also leads to uncertainty in the derived scattering angle. As the crystal

dimensions also affect the efficiency of the camera, a geometrical optimization balancing the two effects was needed.

In general, a larger distance between the scattering and absorbing detectors reduces the angular uncertainty. However, increasing the distances between detectors also decreases the solid angle of the absorber subtended by the scatterer, and decreases Compton efficiency. These effects must be balanced in optimization of a design.

In my dissertation, I will present the detailed design of a Compton camera and further investigate the optimization of the angular uncertainty and efficiency under the constraints of coded aperture imaging implementation.

CHAPTER 3 CODED APERTURES

A coded aperture imaging camera is composed of a coded aperture and a position-sensitive detector. The coded aperture encodes the directions of incident photons. The image of incident photons is reconstructed via a decoding process. The coded aperture is composed of 'mask elements' that usually have an equal size and are distributed in a pre-determined pattern, which is placed on a regular grid. The position-sensitive detector has a spatial resolution that is sufficient to resolve the mask-pattern grid.

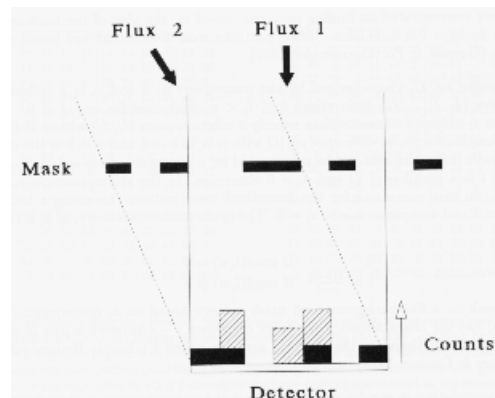


Figure 3-1. The illustration of coded aperture cameras.

In the coded aperture camera, photons from a particular direction project the mask on the detector; this projection has the same coding as the mask pattern, but is shifted relative to the central position over a distance uniquely corresponding to this direction of the photons, as seen in Figure 3-1. The detector accumulates the sum of a number of shifted mask patterns. Each shift of the mask patterns encodes the position and its strength of the pattern represents the source intensity at that specific position. The detector may detect photons incident from any position within the field of view. The accumulated distribution of hits may be decoded to an image by determining the shift and the strength of every possible mask pattern. Proper performance of a coded aperture camera requires that every viewed position is encoded uniquely on the detector

(that is, each source position creates a unique shadow pattern on the detectors). An important difference to direct-imaging systems is the fact that Poisson noise from any source in the field of view is, in principle, induced at any other position in the reconstructed image. The imaging quality of the camera is closely related to the type of mask pattern, the optical design of the camera, the spatial resolution of the detector and the decoding (reconstruction) algorithms.

Aperture Patterns

In order to achieve a desired imaging performance, the mask pattern usually satisfies two conditions. First, the autocorrelation function (ACF) of the mask pattern should be a delta function. Second, the signal-to-noise ratio of a coded source in field of view should be as high as possible. Historically, two types of mask patterns were proposed: a pattern of Fresnel zones [33] and the random pinhole pattern [34, 35], as seen in Figure 3-2. The random pinhole pattern was proposed as an extension of a pinhole camera. The pinhole camera has ideal imaging properties

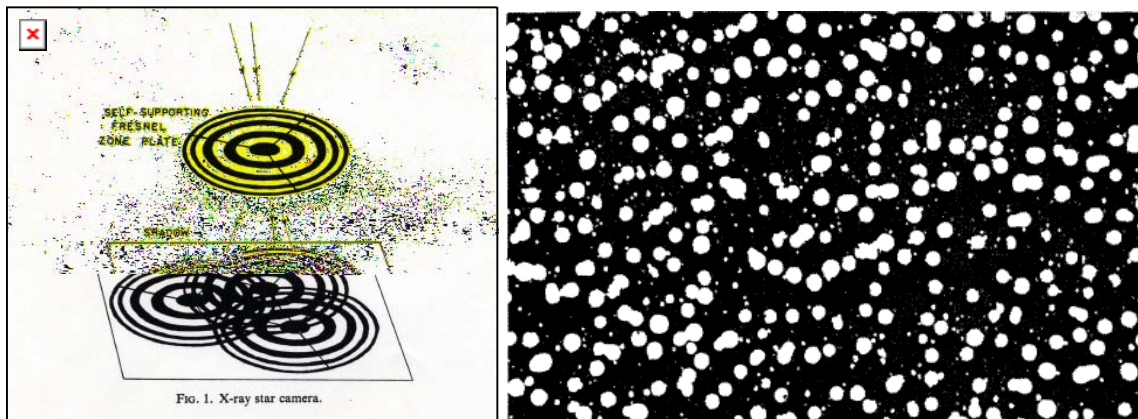


FIG. 1. X-ray star camera.

Figure 3-2. Fresnel zones coded aperture on the left and random pinhole on the right.

with respect to its ACF, but delivers a poor signal-to-noise ratio because of the small diameter of the pinhole necessary to achieve a good angular resolution. In the random pinhole camera, the open area of the plate is increased by randomly placing many duplicate pinholes in the plate. By

keeping the diameter of holes small, the angular resolution is preserved. The random character is necessary to achieve a δ -like ACF.

However, both Fresnel zone and random pinhole mask patterns are not ideal and their ACFs do not have perfectly flat sidelobes that may introduce artifact structure in decoded images. Later, ideal families of patterns were found that are based on cyclic difference sets [36, 37]. A cyclic difference set D , defined by the parameters n , k and z , is a collection of k integer numbers $\{I_1, I_2, \dots, I_k\}$ with values of $0 \leq I_i < n$, such that for any $J \neq 0 \pmod{n}$ the congruence $I_i - I_j = J \pmod{n}$ has exactly z solution pairs (I_i, I_j) within D [38]. An example of a cyclic difference set D with $n=7$, $k=4$ and $z=2$ is the collection $\{0, 1, 2, 4\}$. Cyclic difference sets can be represented by a binary sequence a_i ($i=0, \dots, n-1$) with $a_i=1$ if i is a member of D and $a_i=0$ otherwise. In this example, a_i is given by 1110100. a_i in turn can stand for the discredited mask pattern, assigning a transparent element to $a_i=1$ and an opaque one to $a_i=0$. The cyclic autocorrelation c_l of a_i is:

$$c_l = \sum_{i=0}^{n-1} a_i a_{\text{mod}(i+l, n)} = \begin{cases} k & \text{if } \text{mod}(l, n) = 0 \\ z = \frac{k(k-1)}{n-1} & \text{if } \text{mod}(l, n) \neq 0 \end{cases} \quad (3.1)$$

I_i between 0 and n such that for any $J \neq 0 \pmod{n}$ the congruence $I_i - I_j = J \pmod{n}$ has exactly z solution pairs (I_i, I_j) within D . A mask pattern based on a_i consequently satisfies condition 1. a_i has the characteristic that every difference $i - j$ between a pair of $a_i, a_j = 1$ is equally sampled and therefore these arrays are also called Uniformly Redundant Arrays (URA) [36].

From the ACF, it can be anticipated that it is advantageous with respect to condition 2 to have a difference between k and z that is as large as possible, for k determines the signal and z the background level (and its noise). Additionally, the optimum open fraction of the mask pattern

is also dependent on specific conditions concerning the field of view. The maximum difference is reached if $n = 4t-1$, $k = 2t-1$ and $z = t-1$ if t is integer. These cyclic difference sets are called Hadamard difference sets [38,39] and can be classified into at least three types, according to the value of n : 1) Quadratic residue sets: n is prime (the members of this set are given by the squares, modulo n , of the first $(n+1)/2$ integers); 2) Twin prime sets: $n = p(p+2)$ for integer p , p and $p+2$ being prime; 3) Pseudo-noise sets: $n = 2^m - 1$ ($m > 1$ is integer).

Some Hadamard difference sets may belong to more than one class, the existence of a set with a value for n given by a class is guaranteed. The above example is a quadratic residue set as well as a pseudo-noise set. A characteristic for Hadamard sets is that $k = (n-1)/2$, i.e. for large n the mask pattern is about half open. The cyclic autocorrelation then is:

$$c_l = \sum_{i=0}^{n-1} a_i a_{\text{mod}(i+l,n)} = \begin{cases} \frac{n-1}{2} & \text{if } \text{mod}(l,n) = 0 \\ \frac{n-3}{4} & \text{if } \text{mod}(l,n) \neq 0 \end{cases} \quad (3.2)$$

Another collection of cyclic difference sets are the Singer sets, and are characterized by $n = (t^{m+1}-1)/(t-1)$, $k = (t^m-1)/(t-1)$ and $z = (t^{m-1}-1)/(t-1)$, where t is a prime power. The equivalent mask pattern will have smaller open fractions than those based on Hadamard sets; for $t \gg 1$ the open fraction approximates $1/t$.

One way to construct a pseudo-noise Hadamard set is the following [40]: if $p(0), \dots, p(m-1)$ are the factors of an irreducible polynomial of order m ($p(i)$ is 0 or 1) then a_i is defined by a shift register algorithm:

$$a_{i+m} = \sum_{j=0}^{m-1} p(j) a_{i+j} \quad (i = 0, \dots, 2^m - 2) \text{ mod}(2) \quad (3.3)$$

The first m values of this recursive relation, a_0, \dots, a_{m-1} , can be chosen arbitrarily; a different choice merely results in a cyclic shift of a_i .

If n can be factorized in a product of two integers ($n = p \times q$), it is possible to construct a two-dimensional array a_{ij} ($i=0, \dots, p-1; j=0, \dots, q-1$) from the URA a_i ($i=0, \dots, n-1$). The arranged mask pattern is thus called the 'basic pattern'. The ordering of a_i in two dimensions should be such that the autocorrelation characteristic is preserved. This means that in a suitable extension of the basic $p \times q$ pattern, any $p \times q$ section should be orthogonal to any other $p \times q$ section. A characteristic of a URA a_i is that any array a_i^s , formed from a_i by applying a cyclic shift to its elements ($a_i^s = a_{\text{mod}(i+s, n)}$) is again a URA which is orthogonal to a_i . Therefore, the autocorrelation characteristic of the expanded a_{ij} is fulfilled if every $p \times q$ section is a cyclic shift of the basic pattern.

The pseudo-noise arrays have the convenient property that they can easily be wrapped in almost a square of $n \gg 1$: if m is even, n can be written as $n = 2^m - 1 = (2^{\frac{m}{2}} - 1)(2^{\frac{m}{2}} + 1)$, such that p and q only differ by 2.

There are several practical problems in the manufacturing of two-dimensional mask plates. In the traditional x-ray range (up to 120 keV), an opaque mask element may be completely surrounded by transparent elements. For photon energies above 100 keV, this issue of mechanical support is less constraining because transparent materials can easily be found at these energies. A practical problem of masks occurs in applications beyond a few hundred keV: the opaque elements generally need to be very thick. Mask element sizes cannot be small because the mask itself would act as a narrow-field collimator. This is not a serious problem in our design

because thinner opaque may be used and partially opaque events can be eliminated based on the records of hits on the front aperture (acting as an active mask) or scatterer.

The autocorrelation characteristic remains valid only if the coding is performed by the use of a complete cycle of a basic pattern. As soon as the coding is partial, systematic noise will emerge in the side-lobes of the autocorrelation function. In order to be able to record a full basic pattern for every position in the observed field of view, we need to design an optical configuration of mask and detector. The optical design of a coded mask camera involves the sizes of the mask, the mask elements, and the detector, as well as the number of basic patterns used in the mask, the distance between mask and detector and the size and placement of an optional collimator. The design should also provide optimal angular resolution and a wide field of view.

Optimum and Simple Configurations

From the previous section, for ideal imaging properties, it is necessary to record a complete cycle of the basic pattern for every position in the observed field-of-view (FOV). This can be accomplished by configuring the mask and detector in one of the following two ways, as illustrated in Figure 3-3 [41]. In one configuration, the mask consists of one $p \times q$ basic pattern, while the detector has a size of $2p-1 \times 2q-1$ mask elements. By the implementation of a collimator in front of the detector, the observed FOV is restricted to those positions in the FOV from where the mask is completely projected on the detector, as seen in the right of Figure 3-3. In the second configuration, the mask consists of a mosaic of almost 2×2 cycles of the basic pattern $2p-1 \times 2q-1$ mask elements, while the detector is as large as one basic pattern, as seen in the left of Figure 3-3. A collimator is applied to restrict the FOV of any position on the

detector to the region from which one complete cycle of the basic pattern is projected on the detector. This type of configuration often is called 'cyclic' because of the nature of the mask.

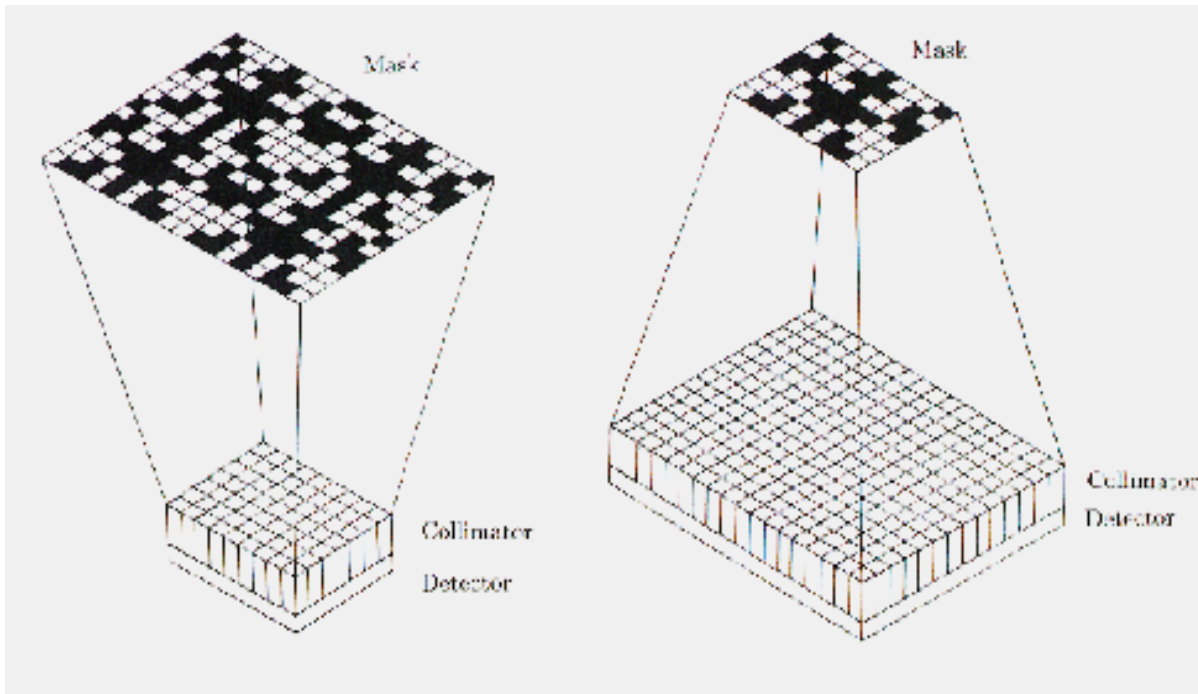


Figure 3-3. Schematic drawings of the two types of 'optimum' configurations discussed. The left configuration is called 'cyclic.'

Both types of collimators deliver a pyramidal-to-zero response function to the collecting detector area over the observed FOV. In practice, for high sensitivity applications, the cyclic type is usually the choice based on the argument of preservation/maximization of the collecting area.

There is also an alternative configuration that is the so called 'simple' or 'box-type' system in which full coding is relaxed, as seen in Figure 3-4 [42]. The detector has the same size as the mask, which consists of one basic pattern. No collimator is then needed on the detector. To prevent photons that do not pass the mask from entering the detector, shielding is used. In this simple system only the on-axis position is coded with the full basic pattern (the fully-coded field of view (FCFV)), the remainder of the FOV is partially coded (partially-coded field of view PCFV). The off-axis sources will introduce false peaks.

Geometries Design

The mask of this design follows the configuration of the cyclic type in which the mask has a larger size than that of detector. In order to increase the FCFV three duplicated patterns are arranged as seen an example in Figure 3-5.

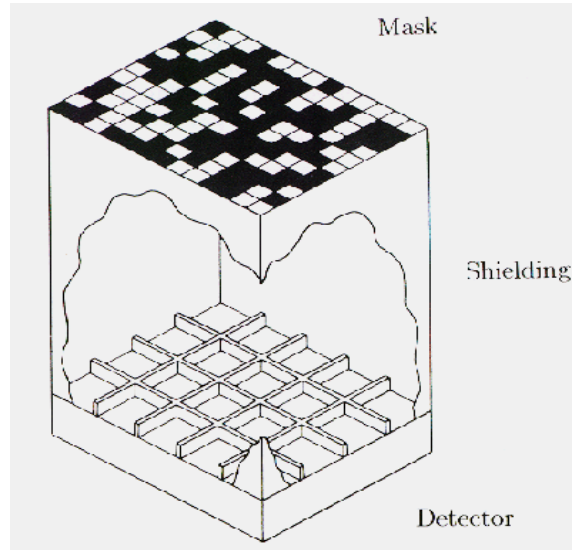


Figure 3-4. Schematic drawing of the 'simple' configuration. The sizes of the mask and detector are equal.

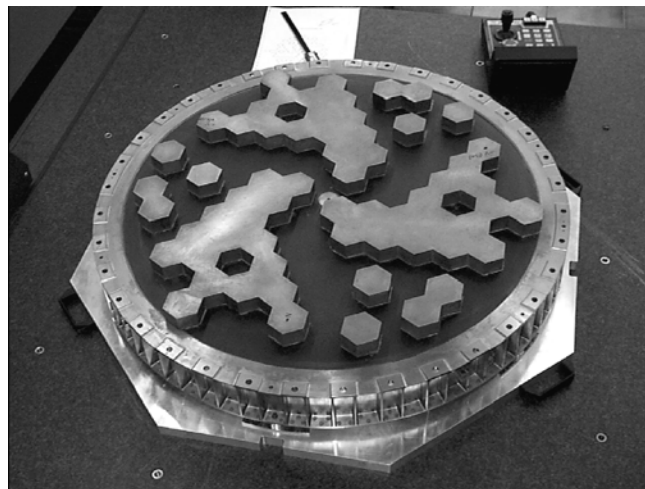


Figure 3-5. SPI Mask is the tungsten alloy elements on top of the support structure [41].

The field of view and geometric resolution are related to the mask and detector parameters.

The field of view is function of the size of detector (d_d) and distances of source to the aperture

(a) and the aperture to the detector (b), as seen below

$$FOV = \frac{d_d}{m-1} \quad (3.4)$$

$$m = 1 + \frac{b}{a}$$

The angular field of view is defined as $\pm\Delta\mathcal{G}$ from its axis and:

$$\Delta\mathcal{G} = \arctan\left(\frac{FOV}{2a}\right) \quad (3.5)$$

In case of a cyclic system, this becomes:

$$\Delta\mathcal{G} = \arctan\left(\frac{d_d}{2b}\right) \quad (3.6)$$

The angular resolution is most commonly defined as the distance that must separate two sources in the object plane so that their images are still perceived as two separate points. Usually the two sources are resolvable if they are separated by at least one full width at half maximum of the point spread function (PSF). In the case of no modulation of the aperture transparency, either complete transparency or opacity, the FWHM on the detector plane is the same as the size of magnified hole by the factor m . Therefore the FWHM on the object plane is:

$$\lambda_g = \frac{mp_m}{b} a = \frac{m}{m-1} p_m = \frac{a+b}{b} p_m, \quad (3.7)$$

where p_m is the size of an aperture hole. That indicates that the best resolution of a coded aperture is the size of an aperture. The angular resolution can be defined as

$$\delta\theta = \arctan\left(\frac{\lambda_g}{a}\right) = \arctan\left(m \frac{p_m}{b}\right) \quad (3.8)$$

Active Coded Aperture Cameras

Based on the knowledge reviewed above, we propose a simple coded aperture camera that utilizes active scattering detectors in the front layer as the coded aperture and the absorbing detectors in the rear layer as the position sensitive detector. An example of the mask design can be adapted from the design of coded aperture used in SPI coded aperture mask on board INTEGRAL[41], as seen in Figure 3-6.

In comparison with conventional coded aperture designs, our design uses an active coded aperture that has an advantage in utilizing the recorded photon interactions in the aperture to improve its opaqueness by eliminating the events with double hits; one in the coded aperture (scattering detectors) and the other in the absorbing detector. Multiple hit events can be utilized in the Compton Camera method for our detector system design. The other advantage is that the efficiency of this design is not reduced by an additional coded aperture in front of the scattering detectors that is used in the conventional hybrid design of imaging system of coded aperture and Compton cameras [43, 44].

For $a \rightarrow \infty; m = 1$, $\delta\theta = \arctan\left(\frac{p_m}{b}\right)$. In order to achieve resolution of 0.3 radians, the ratio of $\frac{p_m}{b} = 0.309$ is required. According to the design of the Compton camera [10], the distance between the coded aperture and the detector is about 30 cm. The size of hole on the coded aperture is about 9cm. If the distance between the sources and coded aperture is very large, the angular field of view is $\Delta\theta = \arctan\left(\frac{d_d}{2b}\right)$. If the size of detector $d_d=100\text{cm}$ we found $\Delta\theta = 1.1903 \text{ radian} \approx 68.2^\circ$. The opening angle of the field of view for our system is about 140° , which is wide enough for most homeland security applications.

In this dissertation, the coded aperture pattern was generated under constraints on the number of detectors, the size of the system and other requirements as discussed in later Chapters. One of the important items addressed is the limited spatial resolution of absorber detectors because the finite size of the crystals and that ordinary photomultiplier tubes (not position sensitive) were used in the initial system design. This will degrade the angular resolution of the coded aperture camera.

CHAPTER 4 IMAGE RECONSTRUCTION ALGORITHMS

Compton cameras do not directly deliver images of incoming photons, but rather utilize coincident hits among detectors to encode the directions of the incoming photons. It is thus necessary to apply image reconstruction algorithms to decode the observation afterwards, which is similar to spatial multiplexing techniques [3]. In general, three kinds of image reconstruction algorithms have been developed: simple back-projection, filtered back-projection, and iterative algorithms. The simple back-projection algorithm and the filtered back-projection algorithm are used to deliver real-time images because they implement individual events, whereas iterative algorithms generally require multiple events in order to reconstruct an image.

The Simple Back-Projection Algorithm

For each two-hit event, the incident gamma-ray direction can be constrained on the surface of a cone with the axis defined by a line that connects the position of Compton scattering and the position of the first interaction of the scattered photon. The half-angle of the cone is derived from the deposited energies based on the Compton relationship. In the simple back-projection algorithm, these cones are projected onto the imaging space, which is the hemisphere around the detector, as seen in Figure 4-1.

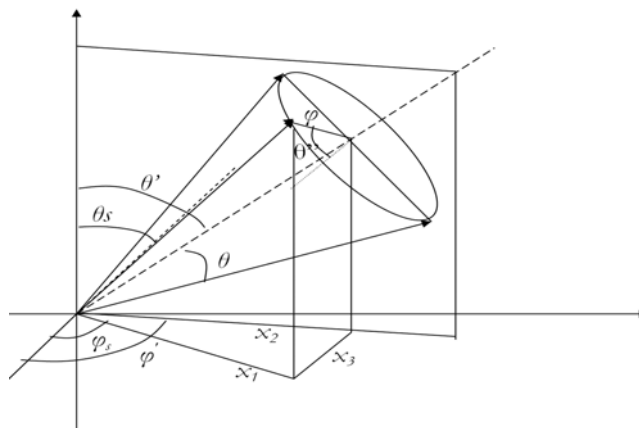


Figure 4-1. The geometry of a Compton scattering event.

The geometry of a scattering event is at the direction of (θ', φ') with scattering angle of θ and azimuthal angle of φ , where (θ_s, φ_s) is the possible direction of the incident photon. The formula used for back projection is given below in Eq. 4.1, which converts all possible directions of the incident photon to a unique coordinate.

$$\cos(\theta_s) = [\sin(\theta') \cos(\varphi) + \cos(\theta') / \tan(\theta)] \sin(\theta) \quad (4.1)$$

$$\cos(\varphi' - \varphi_s) = -\frac{(x_1^2 + x_2^2 - x_3^2)}{2x_1x_2} \quad (4.2)$$

where

$$x_1 = \sin(\theta_s) / \sin(\theta);$$

$$x_2 = \sin(\theta') / \tan(\theta);$$

$$x_3 = \sqrt{1 - \sin^2(\theta'')};$$

$$\sin(\theta'') = \cos(\varphi) \sin(\theta).$$

Examples of two-hit events induced by 662 keV photons incident at $(\theta_s = 0, \varphi_s = 0)$ mapped on the hemisphere are presented in Figure 4-2. Each of the rings on the hemisphere corresponds to all possible directions where a photon might be incident upon the camera.

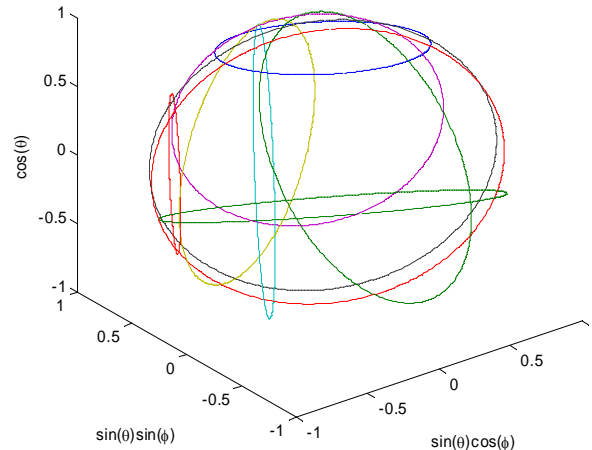


Figure 4-2 Examples of two-hit event mapped onto hemisphere.

The width of the back-projection cone is determined by the angular uncertainty as discussed in Chapter 2. Although the gamma rays from the same direction may pass different cones, the overlaps of these cones along this direction can be distinguished from the background as seen in Figure 4-3, providing locations of high intensity that represent source locations. The figure shows the simple back-projected image of a point source at 662 keV.

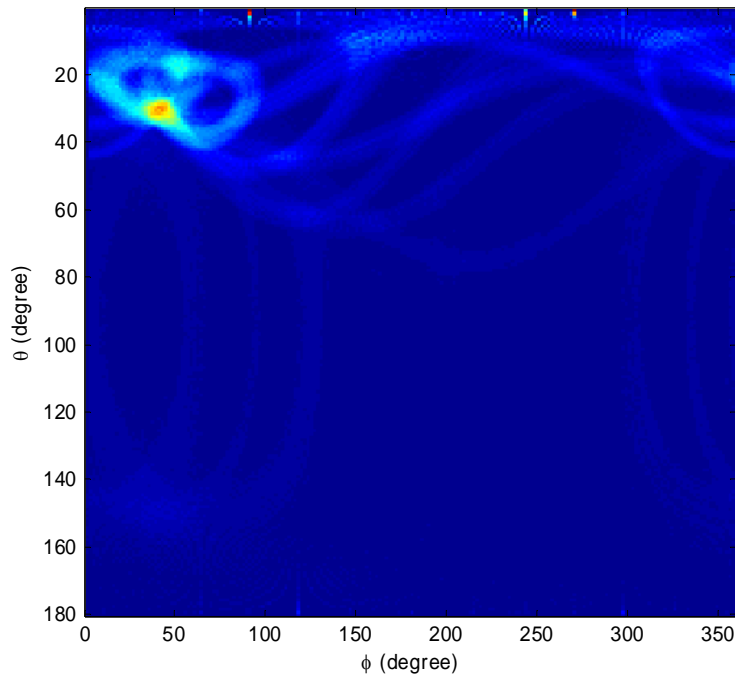


Figure 4-3. The image of a beam of photons one with energy of 662 keV at a polar angle of 30° and an azimuthal angle of $\varphi = 40^\circ$.

Only two-hit events are used in the simple back-projection operation. The angular resolution is about 20° . The sonogram-like features are attributed to the finite number of absorbing detectors which cover a few regions of scattering angles because each observed scattering angle introduces a sonogram-like curve.

Filtered Back-Projection Algorithm

The simple back-projection algorithm is fast and easy to implement, but its angular resolution is limited by the angular uncertainty. Algorithms of the filtered back-projection algorithm have been widely used in computer tomography (CT) image reconstruction [107] to remove blurring features in a point spread function (PSF) and improve spatial and contrast resolution. However, the filtered back-projection algorithm using linear ramp filter in CT systems do not provide good results in Compton cameras because the profiles of the blurred PSF in Compton cameras is different from that in CT systems. In Compton imaging systems, the image plane is expanded by the spherical harmonics rather than the Fourier space, as in CT.

In order to take the advantage of the reconstruction speed of back-projection algorithms and compensate for poor angular resolution, filtered back-projection image reconstruction algorithms have been developed. A direct reconstruction algorithm applied to severely limit scattering directions to only those that are perpendicular to the detector array was developed by Cree and Bones [45]. Analytical inversion methods were also studied on conic surface projections using the spherical harmonics without considering the distribution of possible scattering [46]. An analytical inversion algorithm for the complete data set of all possible scattering angles based on the Klein-Nishina formula was also developed [47]. Since in the Compton imaging system, the image plane is expanded by the spherical harmonics, the filtered back-projection algorithm is implemented based on the expansion of spherical harmonics series rather than Fourier series for CT.

Any function $f(\vec{\Omega})$ on the hemisphere can be transformed into series of spherical harmonics as:

$$f(\vec{\Omega}) = \sum_{l=0}^{+\infty} \sum_{m=-l}^l F_l^m Y_l^m(\vec{\Omega}) \quad (4.3)$$

where

$$Y_l^m(\vec{\Omega}) = \sqrt{\frac{(2l+1)(l-m)!}{4\pi(l+m)!}} P_l^m(\cos\theta) e^{im\phi}$$

$$F_l^m = \int_{s^2} d\vec{\Omega} f(\vec{\Omega}) Y_l^{m*}(\vec{\Omega})$$

In which $P_l^m(\cos\theta)$ is the associated Legendre polynomial.

Ideally, if the Compton relationship for scattering off free electrons is valid and the energy response is the same for different energies, then the mathematic model of Compton camera is:

$$g'(\vec{\Omega}') = \int_{s^2} d\vec{\Omega} g(\vec{\Omega}) h(\cos\omega) \quad (4.4)$$

where $g'(\vec{\Omega}')$ is the image of a given source $g(\vec{\Omega})$; $h(\cos\omega)$ is the point spread function with azimuthal symmetry, and ω is the angle between $\vec{\Omega}$ and $\vec{\Omega}'$. According to the spherical convolution theorem [56], in the spherical harmonics form, this convolution is:

$$G_l'^m = \sqrt{\frac{4\pi}{2l+1}} G_l^m H_l^0 \quad (4.5)$$

where $G_l'^m$, G_l^m , H_l^0 are the transformations of $g'(\vec{\Omega}')$, $g(\vec{\Omega})$, and $h(\cos\omega)$ in the spherical harmonics domain, respectively. The spherical harmonics coefficients of $h(\cos\omega)$ are:

$$H_l^m = \int_{s^2} d\vec{\Omega} h(\cos\omega) Y_l^{m*}(\vec{\Omega}) \quad (4.6).$$

For the azimuthal symmetric $h(\cos\omega)$, its spherical harmonics coefficients are zero for all $m \neq 0$.

For $m=0$, we have:

$$\begin{aligned}
H_l^0 &= \int_{s^2} d\vec{\Omega} h(\cos \omega) Y_l^{0*}(\vec{\Omega}) \\
&= \sqrt{\pi(2l+1)} \int_{\pi} d(\cos \omega) h(\cos \omega) P_l^0(\cos \omega) \\
&= \sqrt{\frac{4\pi}{2l+1}} \left(\frac{2l+1}{2} \right) \int_{\pi} d(\cos \omega) h(\cos \omega) P_l(\cos \omega) \\
&= \sqrt{\frac{4\pi}{2l+1}} H_l
\end{aligned} \tag{4.7}$$

where $H_l = \left(\frac{2l+1}{2} \right) \int_{\pi} d(\cos \omega) h(\cos \omega) P_l(\cos \omega)$. Thus, the spherical harmonics coefficients of source are derived as:

$$G_l^m = \frac{2l+1}{4\pi H_l} G_l'^m \tag{4.8}$$

In an ideal case where response does not depend on the incident angle, $h(\cos \omega)$ can be obtained as:

$$h(\cos \omega) = \frac{1}{2 \sin \frac{\omega}{2}} \int_{\frac{\omega}{2}}^{\pi - \frac{\omega}{2}} \frac{d\theta K(\theta)}{\sqrt{\cos^2 \frac{\omega}{2} - \cos^2 \theta}} \tag{4.9}$$

where $K(\theta)$ is the Klein-Nishina cross section formula:

$$K(\theta) = \frac{1}{\sin \theta} \frac{d\sigma}{d\theta} = Zr_0^2 \pi \left(\frac{E_{\gamma_1}}{E_{\gamma_0}} \right)^2 \left(\frac{E_{\gamma_0}}{E_{\gamma_1}} + \frac{E_{\gamma_1}}{E_{\gamma_0}} - \sin^2(\theta) \right) \tag{4.10}$$

However, due to the limitation in the detector system configuration and the difficulty in detecting small-angle scattering events in practice, an algorithm applied to the limited angle Compton camera data set was developed [48]. This is especially important for application of Compton cameras with limited coverage of scattering angle, such as that in the design presented here. The design presented in this dissertation can only detect the Compton scattering events of certain scattering angles. This is due to the limited number of absorbing detectors and the

variation in the attenuation of the detection material at different scattering directions. The scattered photon energy changes at different scattering angles. Therefore, the measured scattering angle distribution will be different from the prediction based on the Klein-Nishina formula.

In this dissertation, a deconvolution algorithm using the spherical harmonics will be further investigated. The point spread function will be numerically calculated based on the Klein-Nishina formula which takes into account the incomplete coverage of absorbing detector over the scattering angle.

Iterative Approach

Iterative algorithms are general methods to reconstruct images for Compton cameras [49, 50]. Iterative algorithms allow detailed physical-modeling and noise modeling to be used in image reconstruction and deliver better angular resolution than that of back-projection algorithms. In general, a Compton camera system consists of two detectors, scatterer and absorber, which are parallel to each other, as shown in Figure 5-4. A true coincident two-hit event (also referred to as a valid event) is recorded when a photon is scattered in the first detector and then absorbed in the second detector. In each valid event we record: (1) scattering position, (2) interaction position of the scattered photon, and (3) E_1 and E_2 , the energy transferred to the scatterer and absorber, respectively.

For each combination of interaction positions in the two detectors: a scattering angle, the axis $\overline{P_1P_2}$, an apex P_1 and E_1 and E_2 are determined. A mathematical expression for the Compton projection data (ignoring random coincidences) can be given as

$$g_{P_1P_2E_1E_2} = \sum_{ijkE_0} f_{ijkE_0} H_{ijkE_0}^{P_1P_2E_1E_2} \quad (4.11),$$

where the Compton projection data and source distribution are represented by $g_{P_1P_2E_1E_2}$ and f_{ijkE_0} , respectively. The response matrix $H_{ijkE_0}^{P_1P_2E_1E_2}$ represents the probability that a photon emitted from a voxel (i, j, k, E_0) is scattered at position P_1 in the scatterer which deposits energy E_1 and detected at position P_2 of the absorber and deposits energy E_2 .

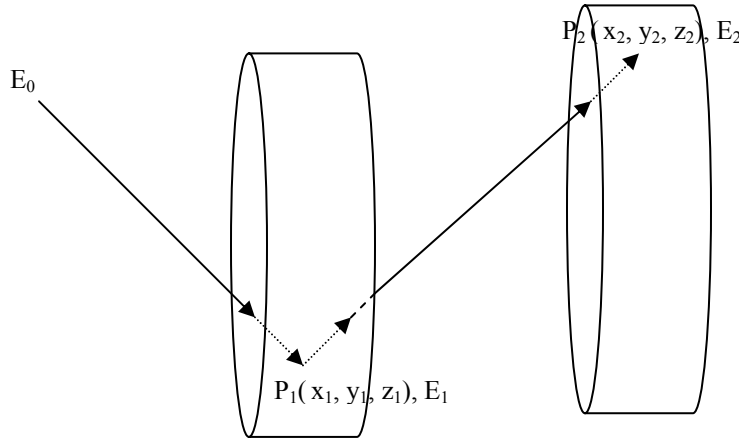


Figure 4-4. The two coincident hits in Compton camera.

The Expectation-maximization algorithm (EM algorithm), which is the same for all emission imaging systems, is given by [50, 51]

$$\hat{f}_{ijkE_0}^{n+1} = \frac{\hat{f}_{ijkE_0}^n}{\sum_{P_1P_2E_1E_2} H_{ijkE_0}^{P_1P_2E_1E_2}} \sum_{P_1P_2E_1E_2} H_{ijkE_0}^{P_1P_2E_1E_2} \frac{g_{P_1P_2E_1E_2}}{\sum_{klmE} \hat{f}_{klmE}^n H_{klmE_0}^{P_1P_2E_1E_2}} \quad (4.12)$$

The above EM algorithm is implemented by iterations requiring projection of the estimated source distribution and back-projection of the ratio between the measured and estimated projection data. However, this method is impossible to implement unless there is a method to calculate $H_{ijkE_0}^{P_1P_2E_1E_2}$, because the stored response matrices are unreasonable due to their large sizes.

In order to reduce the computer time Barrett and his colleagues applied Maximum-likelihood image reconstruction to list-mode data [108, 109] that was so called MLEM. However, the MLEM algorithm is usually slow in converge. This is especially true for the cases involving response matrixes with large size. The ordered subset expectation maximization (OSEM) algorithm [52] is a possible approach to accelerate the reconstruction speed. The OSEM algorithm divides the measured data set into several subsets, and uses the reconstructed image of the previous subset as the initial image of the next subset. The algorithm can provide order-of-magnitude acceleration over conventional MLEM algorithms and is relatively easy to implement [52]. Recently, the application of OSEM in Compton cameras has been probed under certain approximations by Kim et al. [53]. The promising results will lead to more studies devoted to this new approach for Compton cameras.

In this dissertation, the symmetric approximation and factorization approach is utilized to calculate the $H_{ijkE_0}^{P_1P_2E_1E_2}$ based on much smaller prior stored data sets. The OSEM approach will also be investigated.

Decoding Coded Aperture Images

In coded aperture imaging systems, the encoding process can be converted into the convolution [54, 55]:

$$\begin{aligned}
 R(\vec{r}) &\propto O' * A' \\
 O'(\vec{r}) &\equiv O\left(-\frac{a}{b}\vec{r}\right) \text{ and } A' \equiv A\left(\frac{a}{a+b}\vec{r}\right)
 \end{aligned} \tag{4.12}$$

where $R(\vec{r})$ is the image observed on the detector plane, and O and A are the source distribution and coded aperture pattern, respectively. Instead of back-projection methods to reconstruct the source distribution, there is a correlation method of decoding that is a way of locating the mask pattern in the projection. The implementation of correlation reconstruction is:

$$\hat{O} = R \times G \quad (4.13)$$

Therefore,

$$\hat{O} = O' * (A' \times G) + N \times G, \quad (4.14)$$

If,

$$A' \times G = \delta \quad (4.15)$$

then,

$$\hat{O} = \hat{O}' + N \times G$$

where N represents the noise. In the reconstructed image, the noise is still present, but it is not ill-behaved as that in the back-projection approaches, based on Fourier transforms.

In this work, a proposed design of a coded aperture A for a given number of scattering detectors is presented and analyzed. The performance of the correlation reconstruction approach with Monte-Carlo simulation is investigated. In order to combine image reconstruction of multi-coincident events, iterative image reconstruction algorithms for the coded aperture approach are also investigated.

CHAPTER 5
LaBr₃:Ce SCINTILLATION DETECTOR

Scintillation crystals have been widely used in imaging and spectroscopy of energetic photons (γ -rays) at room temperature. The desired properties of scintillation crystals for many spectroscopy applications include high light output, high Z, fast response, low cost, good linearity, and minimal afterglow. Recently, a new cerium doped halide scintillator, LaBr₃, has been discovered which has attractive scintillation properties such as very high light output (~60,000 photons/MeV), and fast principle decay constant (30 ns) [57, 58], as seen in Table 5-1. Based on these properties, LaBr₃:Ce is a promising scintillator for γ -ray imaging and spectroscopy, because the high light yield allows reduced statistic fluctuation in energy determination and allow application of position sensing in the detector. The fast decay was desired for precision coincident timing used in Compton cameras.

Table 5-1 Comparison of scintillation crystals.

	Light Yield Photons/keV	Decay Time τ (ns)	τ /Light Yied
BaF2	1.8	0.8	0.44
BrilLanCe*380	63	16	0.25
BrilLanCe*350	49	28	0.57
LSO	27	40	1.48
NaI(Tl)	38	250	6.58
GSO	8	60	7.50
BGO	9	300	33.3

LaBr₃ has a hexagonal (UCl₃ type) structure with P63/m space group [58, 59, 60], as seen in Figure 5-1, and has a density is 5.3 g/cm³. LaBr₃ compound melts at 783 °C congruently. Therefore LaBr₃ crystals can be grown using melt based methods such as Bridgman and Czochralski which are well suited for growth of large volume crystals [60].

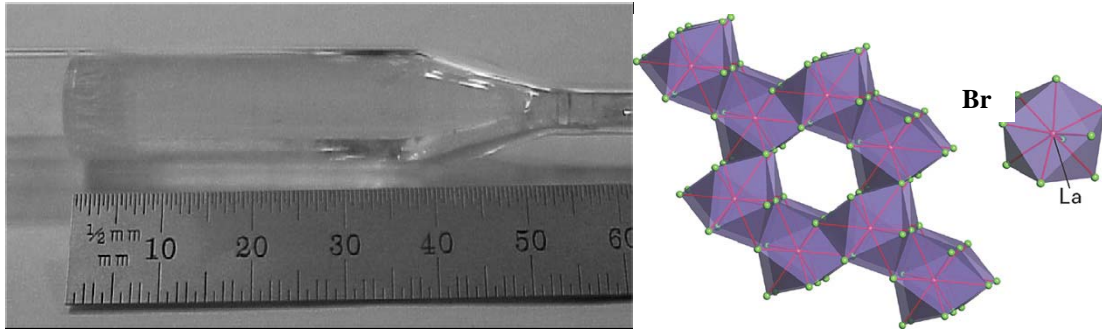


Figure 5-1. LaBr₃ Crystal and its Hexagonal structure of LaBr₃.

Scintillation Mechanisms

The superior properties of LaBr₃:Ce are attributed to Ce³⁺[61]. The desired scintillation mechanism in LaBr₃:Ce is the prompt transfer (faster than 1 ns) of a free electron and free hole from the ionization track to Ce³⁺ leading to 4f–5d excitation and followed by 5d–4f emission with 100% efficiency. However, there are number of processes to transfer electrons to various sites. There are two types mobilization process that are important in the scintillation. First, a hole at the top of the valence band is not stable and will be bound between two anions to form a 2 X-- like molecular complex (X = F, Cl, Br, I, which known as V_k center) accompanied by strong lattice relaxation [62] that may jump from one site to an adjacent site by thermal activation. Second, the V_k center traps an electron from the conduction band because it carries positive charge. In this case, a self-trapped exciton (STE) is created which is a neutral defect and may migrate thermally with a speed faster than that of a V_k center [62].

The role of V_k and STE centers in the scintillation is illustrated in Figure 5-2. Figure 5-2a shows the self-trapping of a hole into a V_k center (indicated by arrow 1). Next the V_k center migrates by a thermally activated hopping migration to

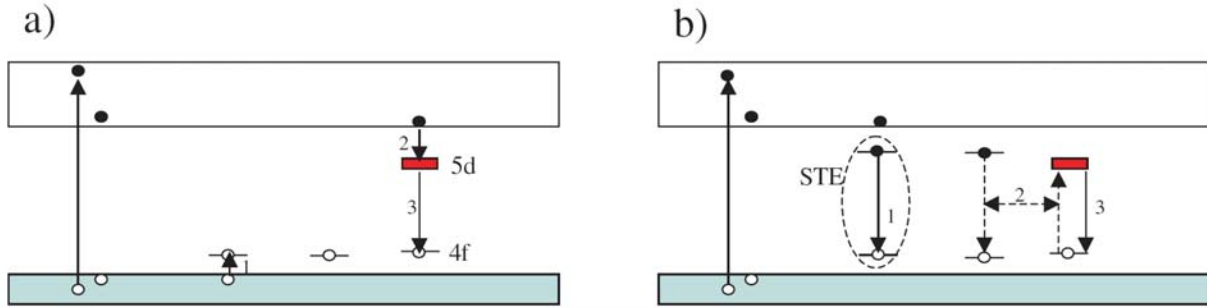


Figure 5-2. a) Binary V_k and electron diffusion, and b) STE migration in the scintillation process.

the Ce^{3+} ion where it is trapped to form Ce^{4+} or a $Ce^{3+} - V_k$ associated complex. Finally the electron is trapped in this center (arrow 2) leading to excitation of Ce^{3+} followed by 5d–4f photon emission (arrow 3). This process is binary V_k and electron diffusion. In this case, the scintillation decay time τ_s is determined not only by the lifetime τ_v of the 5d-state of Ce^{3+} but also by the transfer speed of V_k centers to Ce^{3+} and electrons to Ce^{4+} or $Ce^{3+} - V_k$.

The more complex situation occurs when, before being trapped by Ce, V_k traps an electron to form an STE, as shown in Figure 5-2b. The STE is a luminescent defect by itself with typical decay time of several microseconds (arrow 1). The STE is also a mobile defect that may transfer its energy to Ce^{3+} (arrow 2) leading to delayed Ce^{3+} emission (arrow 3), when in the vicinity of Ce^{3+} . In some compounds, the STE emission is quenched at low temperatures, and when the lifetime of the STE is shorter than the time needed to transfer energy, this can be an important scintillation loss factor. Depending on the spectral overlap between STE emission and Ce^{3+} absorption, radiative transfer is also possible.

Spectroscopy with $LaBr_3:Ce$ Detectors

In our design we selected the BrillanCe 380 ($LaBr_3(Ce)$) detector that was manufactured by Saint-Gobain company. In order to maximize light collection, $LaBr_3:Ce$ crystals are wrapped in

reflective, white Teflon tape on all faces (except the one that coupled to a photomultiplier (PMT)). An optic index matching silicone fluid was also used at the PMT scintillator interface. The energy resolution at 662 keV as function of temperature and BrillanCe 380 detector are shown in Figure 5-2.

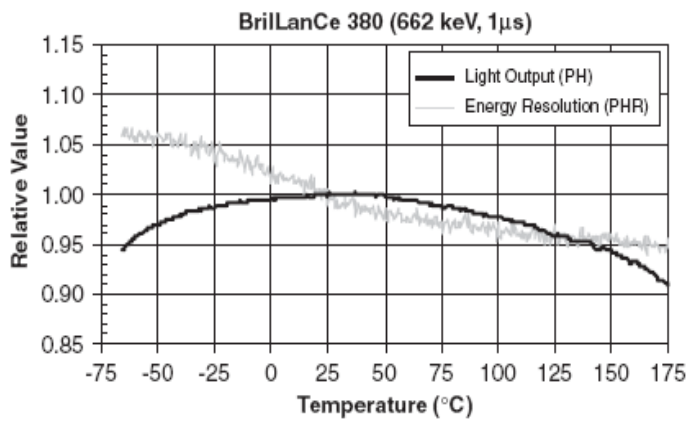


Figure 5-3. The energy resolution at 662 keV as function of temperature on left and BrillanCe 380 detector on right.

The energy spectrum of ^{22}Na source measured with $\text{LaBr}_3:\text{Ce}$ crystals is shown in Figure 5-4 and the energy resolution is function of energy as shown in Figure 5-5.

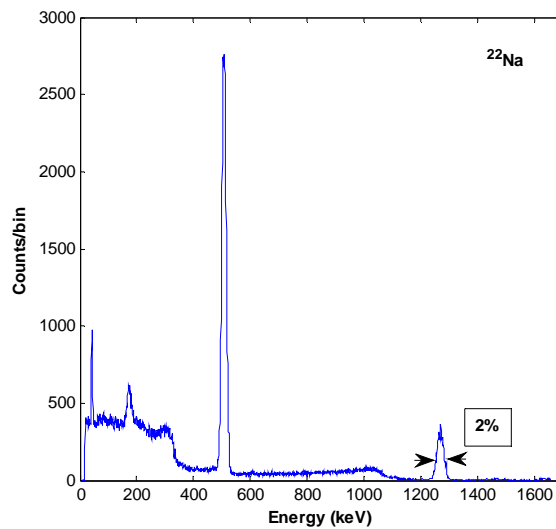


Figure 5-4 The energy spectrum of ^{22}Na .

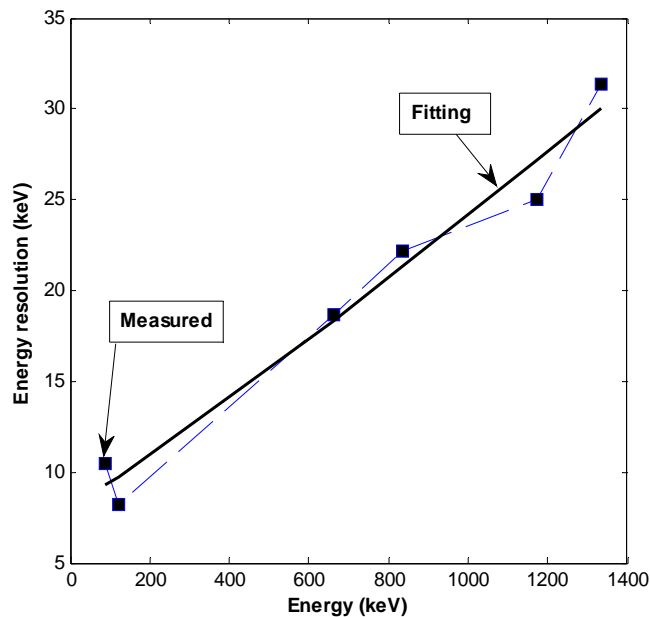


Figure 5-5. The fitting of energy resolution as a function of energy.

However, there are number of internal contaminants, such as ^{227}Ac and ^{238}U decay chain, in LaBr_3 that create features in spectrum, as seen in a 36,000 second unshielded background spectrum taken with the $\text{LaBr}_3:\text{Ce}$ detector (Figure 5-6). The peak at ~ 1460 keV is the 1436 keV gamma ray that has structure related to a coincident x-ray that is absorbed in the detector. The broad feature around 750 to 1000 keV is the 789 keV gamma rays in coincidence with a beta particle. All of these features are attributed to the internal ^{138}La decay.

Above the 1436 keV gamma-plus-x-ray peak in energy there are many peaks (1550–3000 keV) associated with the alpha decays from ^{227}Ac . The gross count rate, in this case is 0.58 counts per second. The small bumps between 250-650 keV are external background gamma rays from the ^{238}U decay chain.

Timing Properties of $\text{LaBr}_3:\text{Ce}$

^{137}Cs gamma-ray excited decay curves of $\text{LaBr}_3:5\% \text{Ce}^{3+}$ recorded at 100, 300 and 600 K are shown in Figure 5-7 [61]. A more complete study can be found in [61]. They exhibit a fast

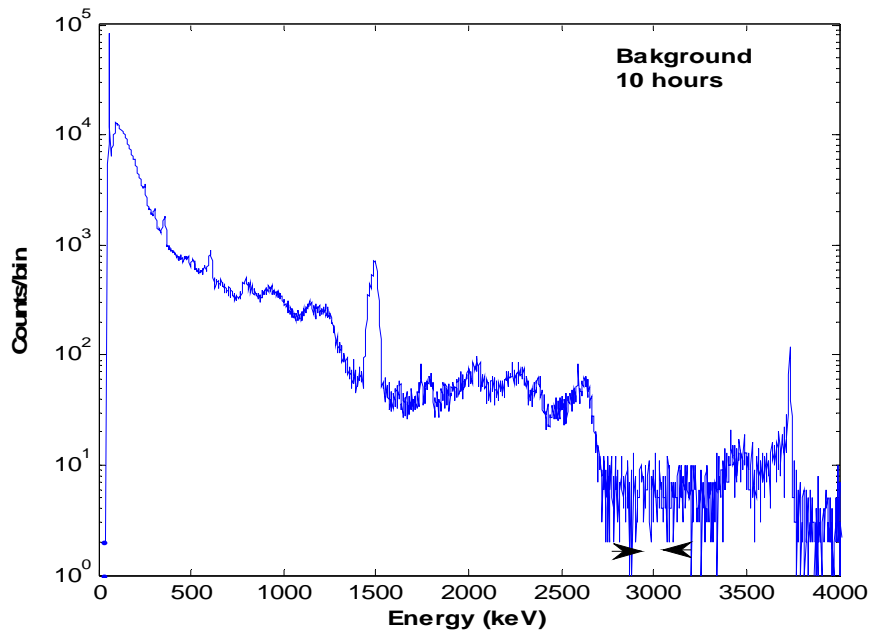


Figure 5-6 Background spectrum measured with BrilanCe 380 LaBr₃ detector in 10 hours.

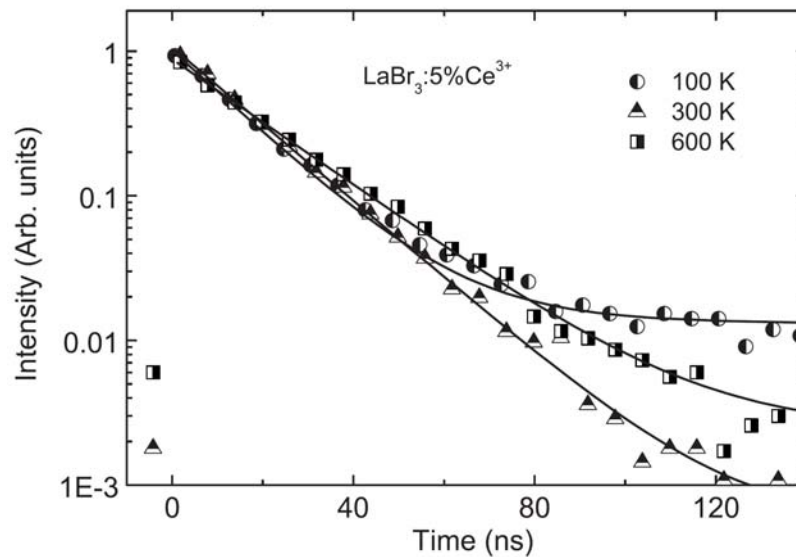


Figure 5-7 Temperature dependence of LaBr₃:5% Ce³⁺ scintillation decay curves. The solid curves are drawn to guide the eye and are not fitted curves.

component of 16 ns at 100 and 300 K and 21 ns at 600 K. At 100 K, a slow component with 0.3 μ s exponential decay constant provides a contribution of 40% to the total light yield. The absence of decay time shortening of the fast component with the increase of temperature

indicates that thermal quenching of 5d to 4f emission does not occur. In general, the fluorescent decay times of $\text{LaBr}_3:\text{Ce}$ samples doped 5% Ce were measured using the delayed coincidence method.

Overall, these measurements indicate that $\text{LaBr}_3:\text{Ce}$ is a promising scintillator. It has high light output, fast response and shows good energy and timing resolution. It is the desired scintillation material to be used in applications of medical imaging, nuclear physics, X-ray diffraction, non destructive evaluation, treaty verification and non-proliferation monitoring, environmental cleaning, and geological exploration.

CHAPTER 6 EXPERIMENT AND HARDWARE

In order to evaluate the feasibility of using $\text{LaBr}_3\text{:Ce}$ detectors in Compton camera designs, a bench top Compton camera was setup and tested. The experimental implementation of the coded aperture camera was difficult. To mimic the coded aperture imaging system without a sufficient number of detectors to create the MURA was challenging and time consuming. However, the test of the coded aperture camera may be achieved by scanning the absorbing plane with a few detectors and comparing the results with the modeling and simulations within this dissertation. For investigating the imaging capabilities of the design of Compton camera, we experimentally implemented the Compton camera design with two LaBr_3 detectors. One of the detectors served as scattering and the other scanned over the scattering angles, as seen in Figure 6-1.

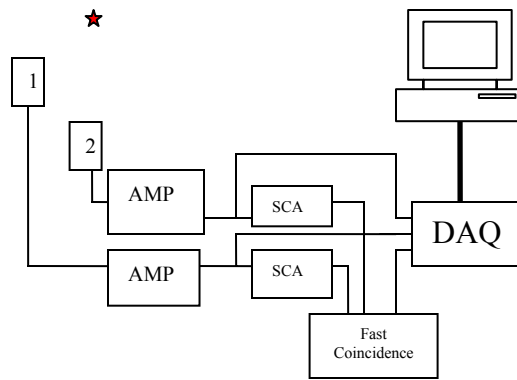


Figure 6-1 The sketch of experimental setup.

LaBr_3 Detector

The two used detectors were Brilliance 380 detectors but have different thicknesses and the same radii of 2.5 cm[63]. The thickness of the absorber was approximately 2.5 cm, while the thickness of the scatterer was about 0.5 cm. The scintillation signal was sensed and amplified by a Photonis XP2060B, 39mm diameter, photomultiplier tube (PMT). The PMTs entrance window

was optically coupled to the scintillator by optical couplant. The XP2060 has a bi-alkali photocathode which ensures a wide wavelength response. The 10 dynode stages were designed to provide significant multiplication while retaining good pulse height resolution and linearity at low biases. Low-voltage (~ 460 V comparing to ~ 1000 V for NaI detector) operation is necessary because of the very high scintillation light output of LaBr_3 (60,000 photons/MeV) coupled with its short duration ($\tau = 15$ ns). LaBr_3 detectors achieved better energy resolution than that of NaI, as seen in Figure 6-2.

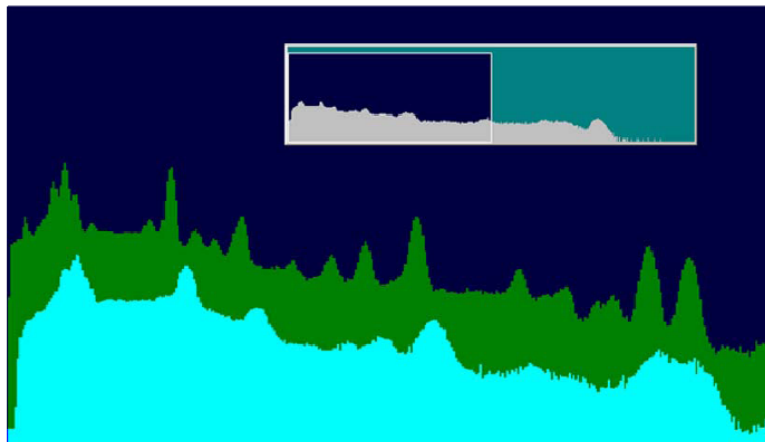


Figure 6-2. ^{232}Th Spectra from $\text{LaBr}_3:\text{Ce}$ (upper) and $\text{NaI}(\text{Tl})$ (lower)

The distance between the scattering plane and absorbing plane in the experimental measurements was about 10~20 cm in order to investigate the relationship between the angular resolution and the distance with a relatively high efficiency.

Data Acquisition Hardware

The electronic readout system was setup with a NI-DAQ 7 PCI card (NI PCI-MIO-16E-1) [64], as seen in Fig. 6.3, and SCB-68-68-Pin shielded connector block [64], as seen in Figure 6-4. Both pieces of equipment are from National Instruments. The DAQ hardware digitizes signals, performs D/A conversions to generate analog output signals, and measures and controls digital

I/O signals. E Series devices use the National Instruments DAQ system timing controller (DAQ-STC) for time-related functions (used in coincidence measurements). The DAQ-STC consists of the following timing groups:

- a) AI—Two 24-bit, two 16-bit counters;
- b) AO—Three 24-bit, one 16-bit counter;
- c) General-purpose counter/timer functions—Two 24-bit counters.

The DAQ-STC can independently configure the groups for timing resolutions of 50 ns or 10 μ s. With the DAQ-STC, a wide variety of internal timing signals to other internal blocks can be interconnected. The interconnection scheme is flexible and completely software-configurable. The DAQ-STC offers PFI lines to import external timing and trigger signals or to export internally generated clocks and triggers. The DAQ-STC also supports buffered operations, such as buffered waveform acquisition, buffered waveform generation, and buffered period measurement. It also supports numerous non-buffered operations, such as single pulse or pulse train generation, digital input, and digital output.

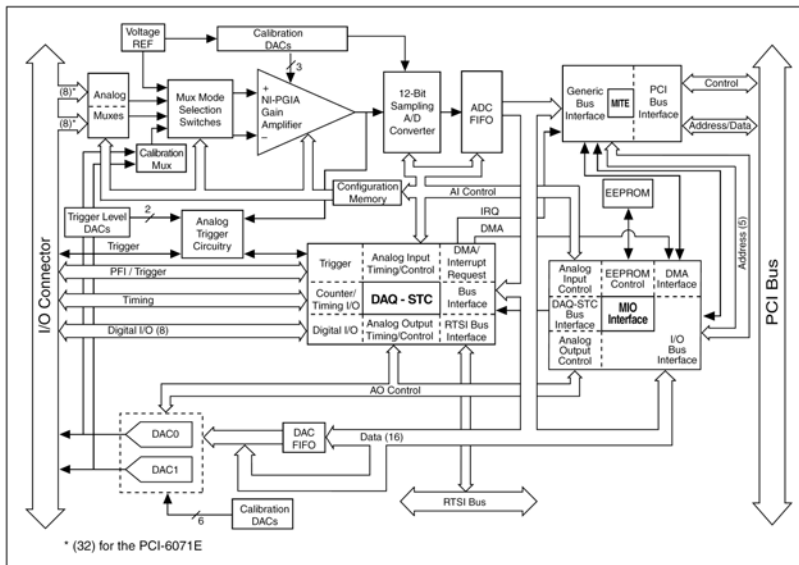


Figure 6-3. The picture of NI PCI-MIO-16E-1 card and block diagram.

National Instruments measurement devices are packaged with NI-DAQ driver software, an extensive library of functions and VIs can be called from application software, such as LabVIEW or LabWindows/CVI, to program all the features of NI measurement devices. Driver software has an application programming interface (API), which is a library of VIs, functions, classes, attributes, and properties for creating applications for a device.

The SCB-68 is a shielded I/O connector block with 68 screw terminals for easy signal connection to a National Instruments 68- or 100-pin DAQ device. The SCB-68 features a general breadboard area for custom circuitry and sockets for interchanging electrical components. These sockets or component pads allow RC filtering, 4 to 20 mA current sensing, open thermocouple detection, and voltage attenuation.

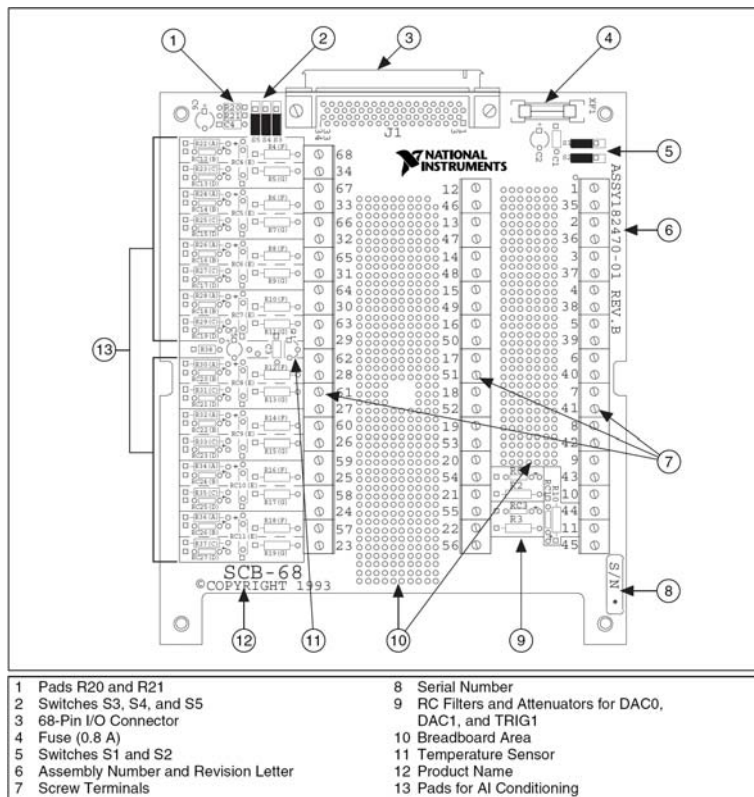


Figure 2-1. SCB-68 Printed Circuit Diagram

Figure 6-4. SCB-68 printed circuit diagram.

In the experiment, three channels were used. Two channels acquire pulse heights and time from the scattering detector and the absorbing detector, respectively. The third channel is the triggering signal from a timing coincident unit.

Experiment

To evaluate the feasibility of using $\text{LaBr}_3(\text{Ce})$ detectors as both scattering and absorbing detectors in Compton cameras, we setup a bench top system with two $\text{LaBr}_3(\text{Ce})$ detectors, as seen in Figure 6-1. This setup mimicked a Compton camera with one scattering detector and 8 absorbing detectors, as seen in Figure 6-5. In order to reduce the experimental time the separation of the two detectors was reduced to ~ 11.6 cm to increase the absolutely efficiency of this bench top.

During the experiment a point source of Cs-137 with activity of ~ 1 μCi was rotated around the center axis at the normal direction of the front detector while the positions of the two detectors were fixed. Detector 2 was shielded from direct measurement of the source by lead sheets to act as the absorbing (backplane) detector. The source was located off-axis a total of 17.8 cm from the center of the scattering detector and was rotated at 45° intervals from 0° to 360° to mimic each of the 8 detectors. At each location, the number of two-hit events collected was greater than 10^3 .

Signals output from the preamplifiers of two detectors were fed to shaping amplifiers. Shaped signals were sent to QAD card and SCAs that provided low level discriminations. The acquisition process was triggered with timing coincidence signal generated with a fast coincident unit from the two SCAs output signals. The DAD was embedded in a computer and controlled with LabVIEW software. In each QAD channel, 40 data points were sampled. The maximum pulse height and base line levels of pre-trigger and post-trigger were measured online and saved

into a file for post processing. The shaping time of the two shaping amplifiers (AMP) were set to 6 μ s to assure that the pulse peaks were well resolved. Each detector was energy calibrated separately using a mix of common radiation sources.

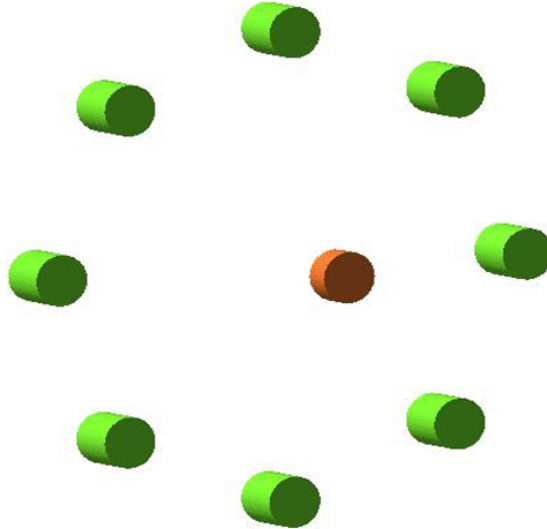


Figure 6-5. The configuration mimicked in the experiment with two detectors. The center detector was the primary scattering detector.

Spectroscopy

The spectra from each detector and the summed spectrum for a ^{137}Cs source are shown in Figure 6-6, in which photon peak and escaped line features appeared at right energy with the similar resolutions of $\text{LaBr}_3(\text{Ce})$ detectors. It demonstrates our pulse height measurements implemented with our LabVIEW codes are correct. The line around 38 keV in the spectrum of detector 2 was due to the escaped K_α photons generated via ionization of K-shell electrons of La in detector 1 and absorbed in the detector 2. The events above 662 keV can be attributed to the high energy background, such as cosmic ray and intrinsic activity in $\text{LaBr}_3(\text{Ce})$ crystals [6]. The energy resolution of the two-hit events was measured as $\sim 3\%$ at 662 keV, which showed that this imaging system was capable of serving as spectrometer.

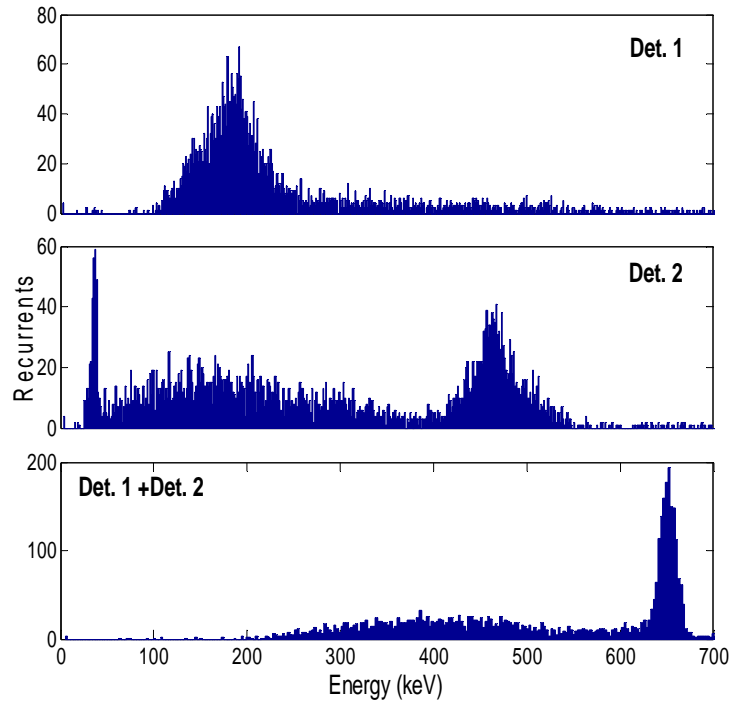


Figure 6-6. The energy spectra of coincident events in the two detectors.

Image

To implement Compton imaging with two-hit coincident events, back-projection and filtered back-projection algorithms were applied. In Compton cameras, the direction of each incident photon can be constrained onto a conic surface determined with a Compton scattering event. The back-projection image reconstruction method is simply a projection of each of the conic surfaces onto (θ, φ) plane, in which the overlapped regions indicate the emission sources [66, 67]. This method has been widely used because of its simplicity and speed, although it did not provide the best quality of image. The formulas we used in the back-projection approach were described in [10].

Images obtained with back-projection were shown in Figure 6-7. In the unfiltered back projection image the point source was evident at (θ, φ) of $(32^\circ, 270^\circ)$, which is near the true source location of $(33^\circ, 270^\circ)$. The ring artifacts can be attributed to the limited coverage of

scattering angles from the eight mimicked detectors, as shown in Figure 6-7. Since there are the artifacts due to limited coverage of scattering angle, the full width at half maximum (FWHM) of the image of the point source varies along different directions of measurement. The FWHM is approximately 30° (0.52 radians) and is consistent with a prediction based on our previous work [10].

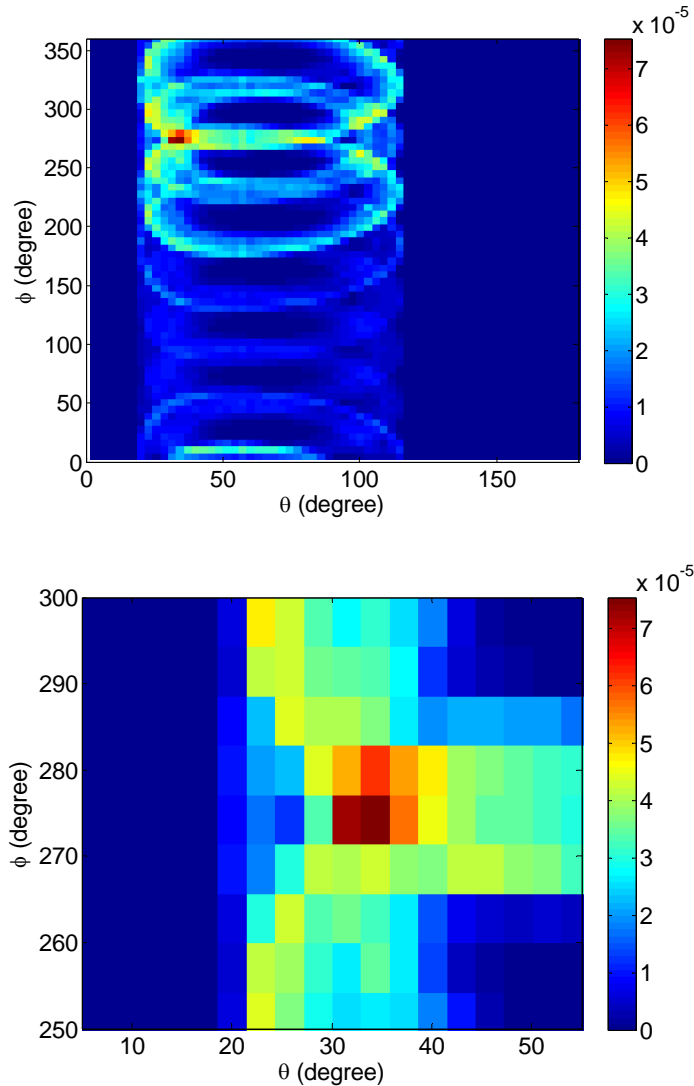


Figure 6-7. The image reconstructed with back-projection method on the top and the zoomed in image on the bottom.

Since the back-projection takes into account the geometric relationship between the incident photons and scattered photons, the reconstructed images do not represent the real source

distributions and introduce artifacts. To improve the image quality, the scattering cross section of Compton and limited coverage of scattering angles by absorbing detectors were need to be considered in image reconstruction that can be partially achieved with filtered back projection algorithms. It has be achieved if the kernel can be represented by a function that is depend on the scattering angle but not the incident directions of photons [68, 69, 70]. In our case the limited coverage of scattering angles leads to a strong dependency between efficiency and incident directions of photons. Therefore, filtered back projection approach did not apply for our bench top experiment.

The iterative methods allows detail modeling of physics of Compton scattering in complex geometries and was used to reconstruct image from the two-hits events recorded in the experiment of the bench top. The response function of the bench top setup to two-hit events was approximated as below.

$$H_{xyzE_0}^{Scat, Abs, E_1, E_2} \propto \int_0^{E_0} \left(\int_0^{E_0-E'} \left(\int_0^{E_0-E'-E''} \frac{d\sigma_{ph}(E_0-E', E'')}{dE''} \Gamma(E_2, E'') \right) \right. \\ \left. + \int_{\Omega_2} \frac{\partial^2 \sigma_{incoh}}{\partial(E_0-E'-E'')\partial\Omega_2} \Gamma(E_2, E'') \Gamma(E_1, E') (1 - P_{int}(Abs_i, E_0-E''-E'', \Omega_2)) d\Omega_2 \right) \\ \left. \Omega_{eff}(x, y, z, E_0, Scat) \times \frac{\partial^2 \sigma_{incoh}}{\partial(E_0-E')\partial\Omega_1} \Gamma(E_1, E') \times (1 - P_{int}(Scat, E_0-E', Abs_i)) \times \Omega_{eff}(Scat, E_0-E', Abs_i) \right) dE' \quad (6.1)$$

where $\Omega_{eff}(x, y, z, E_0, Scat)$ is effective solid angle of the scattering detector to the point of (x, y, z) which takes into account the impact of the geometric shape of the scattering detector and the energy of incident photon on the interaction probability; $\Omega_{eff}(Scat, E_0-E', Abs_i)$ is effective solid angle of the absorbing detector i to the scattering detector which takes into account the impact of the geometric shape of the absorbing detector and the energy of incident photon on the interaction probability; $P_{int}(Scat, E_0-E', Abs_i)$ is the average probability of photon with energy of E_0-E' interacting with the scattering detector; $\Gamma(E, E')$ is the probability of a photon with

energy of E' and is measured as E ; $P_{\text{int}}(\text{Abs}_i, E_0 - E'' - E', \Omega_2)$ is the probability of a photon interacting with the absorbing detector i and escaping at the direction of Ω_2 . In the image reconstruction, the efficiency of the system is needed that can be expressed as:

$$F_{\text{eff}}(x, y, z, E_0) = \sum_{\{\text{Scat}, \text{Abs}_i, E_1, E_2\}} H_{xyzE_0}^{\text{Scat}, \text{Abs}_i, E_1, E_2} \quad (6.2)$$

The calculated efficiency $F_{\text{eff}}(x, y, z, E_0)$ at $z = 15.3 \text{ cm}$ and $E_0 = 662 \text{ keV}$ was shown in Figure 6-8 which showed the symmetric response around the axis of the scattering detector as we expected.

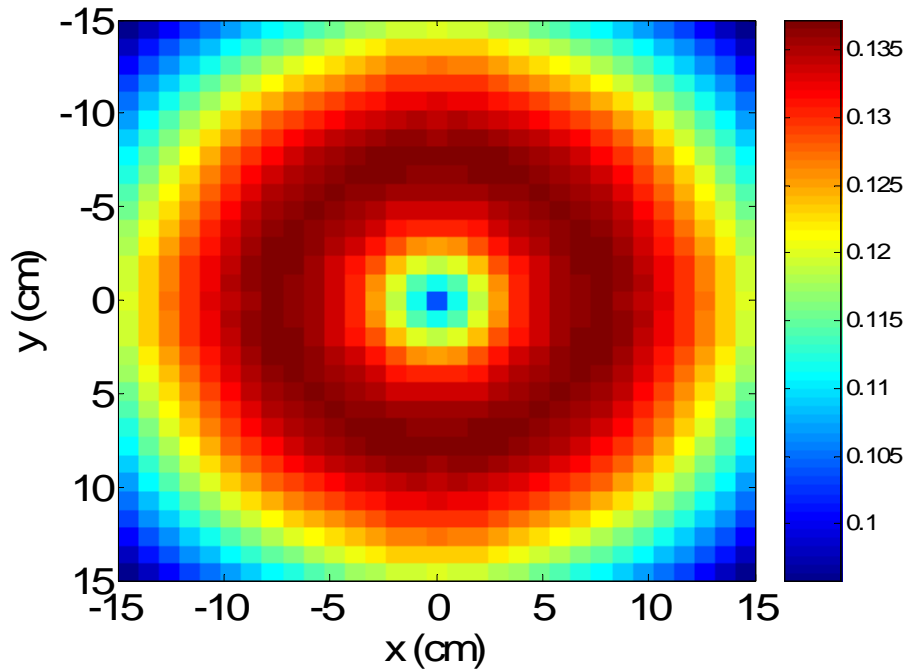


Figure 6-8. The calculated efficiency map of the system as function of the original position of incident photons.

The reconstructed image was shown in Figure 6-9 in which the point source was evident and indicated the angular resolution of the system reduced to about 0.25 radians (FWHM) that was about two times smaller than what we obtained with back-projection method as seen in

Figure 6-7. The improvement of reconstructed image was expected when the imaging system was correctly modeled.

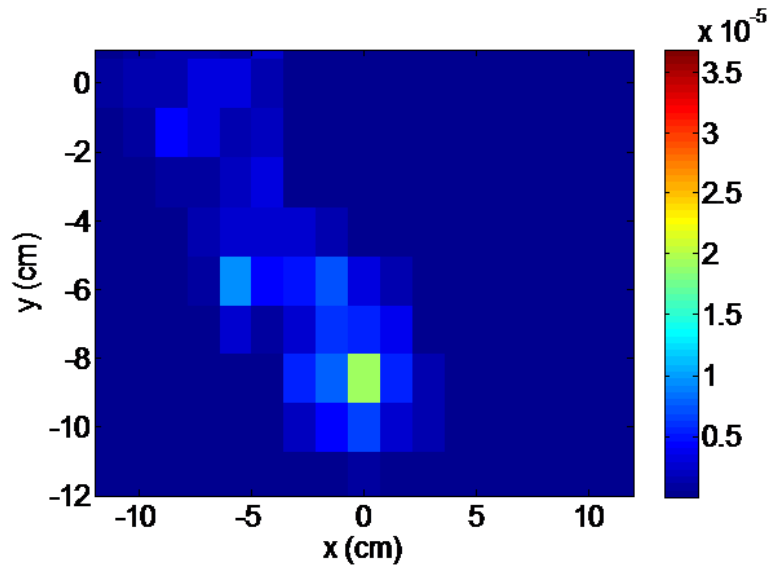


Figure 6-9. The reconstructed image with EML iterative method.

Conclusions

Based on the available hardware in our Lab. as described above we set up a benchtop and successfully acquitted one hit and two-hit data with LabView software. The spectrum of individual detector and coincident spectrum were obtained. The Compton camera approach was successfully implemented on the two-hit data which demonstrated LaBr_3 was able to function in Compton camera and spectroscopy of gamma rays.

CHAPTER 7 DESIGNS AND SIMULATION OF HYBRID CAMERA

Compton camera imaging is a promising approach to achieve higher efficiency and better angular resolution than that of conventional gamma cameras with mechanical collimators for photons with energy above several hundred keV [71, 72, 73], where Compton scattering is the dominant photon interaction. However, for photons with energy near 100 keV, the efficiency of Compton cameras drops significantly because the photoelectric absorption cross section dominates at this energy in most radiation detector materials. Coded aperture imaging is an alternative approach for imaging photons in this energy range and can result in a higher efficiency than that which can be achieved with mechanical collimators [74] and Compton Cameras. In order to image photons across a broader energy range, we designed and investigated a hybrid imaging system that can be implemented as Compton camera and coded aperture camera utilizing an active coded aperture mask that also serves as the Compton scattering layer.

Historically, the hybrid systems with additional coded apertures have been studied for high energy astrophysics [5] and industry applications in e.g. [76, 77]. In those hybrid systems, coded apertures were made from material with high Z and high density to achieve high attenuation. However, at higher energies of photons, the additional coded aperture masks introduced scattering and decrease detection efficiency. In order to overcome these disadvantages in previous designs of hybrid cameras, we presented a relatively unstudied hybrid approach in which the coded aperture is composed of active detection elements, as seen in the discussions of Chapter 3.

To achieve high efficiency and high attenuation, doped $\text{LaBr}_3(\text{Ce})$ with $\sim 5\%$ of Ce is a good candidate for both the scattering and absorbing detectors because of its high atomic number and density. Furthermore, an energy resolution of less than 3% at 662 keV [78] has been

achieved, which is desired for imagers with Compton camera approach and spectrometers. The high light yield and fast decay of light in $\text{LaBr}_3(\text{Ce})$ provided opportunity for applications requiring fast timing and precision position-sensing [78, 79]. In this design, we aimed at about 0.3 radians angular resolution for homeland applications to resolve radiation sources with separation about 10 meters and a few tens meters away. We did not use position sensing techniques in each detector, instead investigating the use an indexed array of detectors and a normal PMT to provide position information. The use of non-position sensitive electronics will also allow the full system to be built at a lower cost than a system that utilizes PSPMTs.

In this Chapter, we describe the method of optimization of the efficiency and angular resolution of this system. The geometric design of the coded aperture with $\text{LaBr}_3(\text{Ce})$ detectors is also described. A prototype design of a hybrid gamma camera is proposed and Monte Carlo simulation of this design is presented. The image reconstruction algorithms investigated are described with detailed modeling of response functions. The lessons we learned from the experimental results and investigation of the prototype are also discussed and summarized.

Optimization of Compton Camera

The optimization of the Compton camera was aimed at two scenarios: highest efficiency for a required angular uncertainty, and the best angular uncertainty for a required efficiency, for particular applications. Unfortunately, these two properties are inversely dependent on one another, thus it is necessary to understand the optimization that must occur with Compton Camera systems. The optimization was based on the calculation of the efficiency of single Compton events in the scatter plane and the resulting angular uncertainty. The uncertainty arises from detector position and energy resolution as well as the inherent Doppler broadening effect.

The probability of single Compton scattering was numerically calculated based on a simple two-layer $\text{LaBr}_3(\text{Ce})$ configuration where the attenuation of $\text{LaBr}_3(\text{Ce})$ on incident and scattered

photons has been taken into account[10]. It shows that at the thickness of ~ 1.25 cm the probability of single Compton scatter reaches the maximum for 662 keV photons. For higher energy photons, the thickness for maximum probability is even larger, which indicates that $\text{LaBr}_3(\text{Ce})$ is a better choice than Si from the efficiency point of view.

Contributions for the angular uncertainty come from the uncertainty in interaction positions. The uncertainties are about the half of the size of the individual detectors, because we assume no position sensing capability is applied. In general, for larger separations, the position uncertainty contributes less to overall angular uncertainty as seen in Chapter 2 and [80].

The contribution of energy resolution to angular uncertainty is a function of scatter angle in Chapter 2 and [81]. This calculation incorporates the measured energy resolution as a function of incident gamma-ray energy. For photons with higher energy, the contribution of energy uncertainty is less significant than that for lower energy photons since the relative energy resolution improves with $1/\sqrt{E}$.

Double differential cross section of Compton scattering over binding electrons [82] is used to determine the uncertainty due to the Doppler broadening effects. For $\text{LaBr}_3(\text{Ce})$ our results show that at scattering angles above 30° and below $\sim 150^\circ$, the contribution of Doppler broadening effects is less than that at other angles Chapter 3, and [83].

Based on the previous results in Chapter 2, a prototype of Compton camera was designed to achieve an angular resolution of about 0.3 radians in which a thickness of 1.3 cm was selected for scattering detectors to achieve a high efficiency. The radius of $\text{LaBr}_3(\text{Ce})$ crystals of both the scattering- and absorbing-layer detectors was selected as 1.27 cm, while the thickness of the absorbing detectors was 2.57 cm for absorbing detectors to achieve high efficiency in absorbing the scattered photons. The separation between scattering and absorbing detectors was set to 30

cm to contribute uncertainty less than <0.2 radians uncertainty, (Figure 2-13). Considering the angular uncertainties induced from energy resolution and Doppler broadening are less than ~ 0.15 radians, the over all angular resolution of the imager is expected to achieve ~ 0.3 radians.

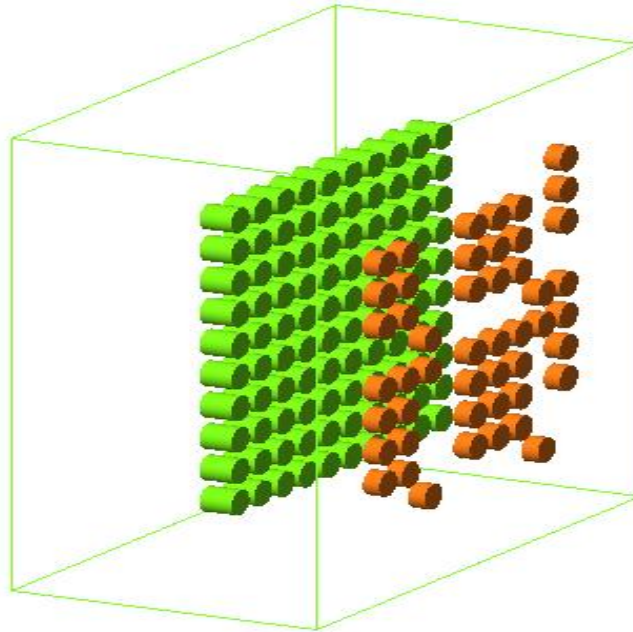


Figure 7-1 The configuration of the hybrid gamma camera used for evaluation with Monte Carlo simulation.

In comparison with the virtual nine detectors in the benchtop setup, we proposed and simulated a prototype hybrid imager that has forty eight scattering and one hundred absorbing detectors, the ring artifacts were less significant in the back-projection image as shown in Figure 7-1 than that in Figure 6-7.

One option to improve the quality of image is an iterative algorithm method, which has been previously applied to reconstruct the image for Compton cameras [71, 91]. Iterative algorithms allow detailed physical-modeling and noise modeling which deliver better angular resolution than that of filtered back-projection algorithms. Detailed physical-modeling of our system is ongoing in which the geometrical shape of detectors will be considered. Therefore,

while this algorithm will be investigated as part of the future work for this system, our research to date has focused on demonstrating the capabilities of imaging and spectroscopy with straightforward algorithms and integrating a Compton camera with a coded aperture scattering layer.

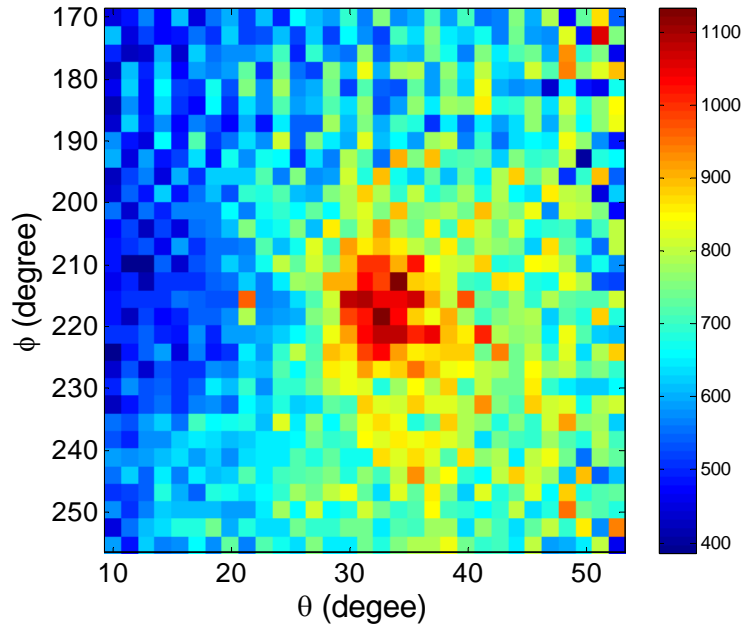


Figure 7-2. The image obtained in Compton camera approach with back-projection method on the right. In this image, the background level is about 400. The FWHM level at ~ 800 , and the FWHM is about 20° that exceeds the goal for the prototype design.

Coded Aperture

The coded aperture was implemented under the constraints of the optimized Compton camera, described previously. For ideal imaging properties it is necessary to record a complete cycle of the basic pattern for every position in the observed field of view (FOV). This can be accomplished by configuring the mask and detector, such as the mosaic of 2×2 of the basic pattern with $2p-1 \times 2q-1$ mask elements, while the detector is as large as the mask. Our coded

aperture pattern was a basic 5×5 ($q = 3$) mosaic pattern of a Modified Uniformly Redundant Array (MURA) [74].

The FOV is a function of the size of detector d_d and distances of source to the aperture a and the aperture to the detector b [74],

$$\Delta\vartheta = \arctan\left(\frac{FOV}{2a}\right); \quad (7.1)$$

the angular resolution can be defined as

$$\delta\theta = \arctan\left(\frac{\lambda_g}{a}\right) = \arctan\left(m\frac{p_m}{b}\right), \quad (7.2)$$

where p_m is the size of an aperture hole.

In order to achieve the angular resolution of 0.3 radians or better, the ratio p_m/b was determined to be 0.31. According to the design and initial models of the Compton camera, the distance between the coded aperture and the detector should then be 30 cm. With this separation, the size of hole on the coded aperture was determined to be less than 9 cm. In this case, angular field of view was $\Delta\vartheta = \arctan(d_d/2b)$. If the size of a detector for a real application was $d_d=100$ cm then $\Delta\vartheta \approx 70^\circ$. The open angle of the FOV of about 140° should be wide enough for most homeland security applications, particularly for screening vehicles.

To implement a coded aperture imaging approach, we selected the one-hit events which were recorded only by the absorbing detectors. In order to reconstruct the image from the shading pattern of $\{A_{i,j} \ i, j=1,2,3,\dots,10\}$ resolved with the 10×10 absorbing detectors, we utilized the cross correlation method

$$c^{l,m} = \sum_{i,j=0}^{n-1} A_{i,j} B_{i,j}^{l,m}, \quad (7.3)$$

in which $B^{l,m}$ is the decoding pattern for the incident directions of $\{l, m=1,2,3,\dots,10\}$ generated from the GEANT4 Monte Carlo simulation package [105].

Prototype Hybrid Gamma Camera and Simulation

Based on the considerations above, a prototype Compton imaging system with $\text{LaBr}_3(\text{Ce})$ detectors for the scatter and absorber planes was simulated (assuming the use of photodiodes to eliminate photon scatter from the PMTs), as seen in Figure 7-5. In the front layer, there were 48 cylindrical crystals distributed in a Modified Uniformly Redundant Array (MURA) that served as the Compton scattering and coded aperture layers. The rear 10 X 10 array served as absorbing and position sensing detectors. The shadow of the front detectors on the absorbing detector array was calculated based on projection. An example is shown in Figure 7-3.

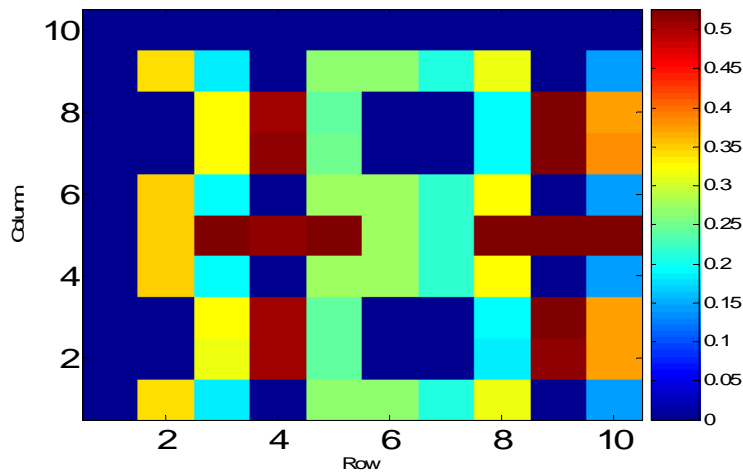


Figure 7-3 The shadows of the scattering detectors on the 10 x 10 array of absorbing detectors when the camera was centered at (0, 0, 0) and irradiated by a point source at (250cm, 0 cm, 1500 cm).

As mentioned above, the geometries were optimized to achieve a high efficiency for the required angular resolution of ~ 0.3 radians. Again, the distance between the scattering and absorbing layers was selected to be 30 cm; the thicknesses were 1.3 cm for scatter and 2.54 cm for absorber, respectively. The radius of all crystals was 2.54 cm. The distance between the

centers of two adjacent elements was 3.81 cm for both layers. All the element sites in the absorbing layer were filled with $\text{LaBr}_3(\text{Ce})$ detectors while only the opaque element sites were filled with LaBr_3 in the front scattering layer. Decoded images with the method described in Chapter 4 showed two point sources at energies of 100 keV and 662 keV are shown in Figures 7-4, 5.

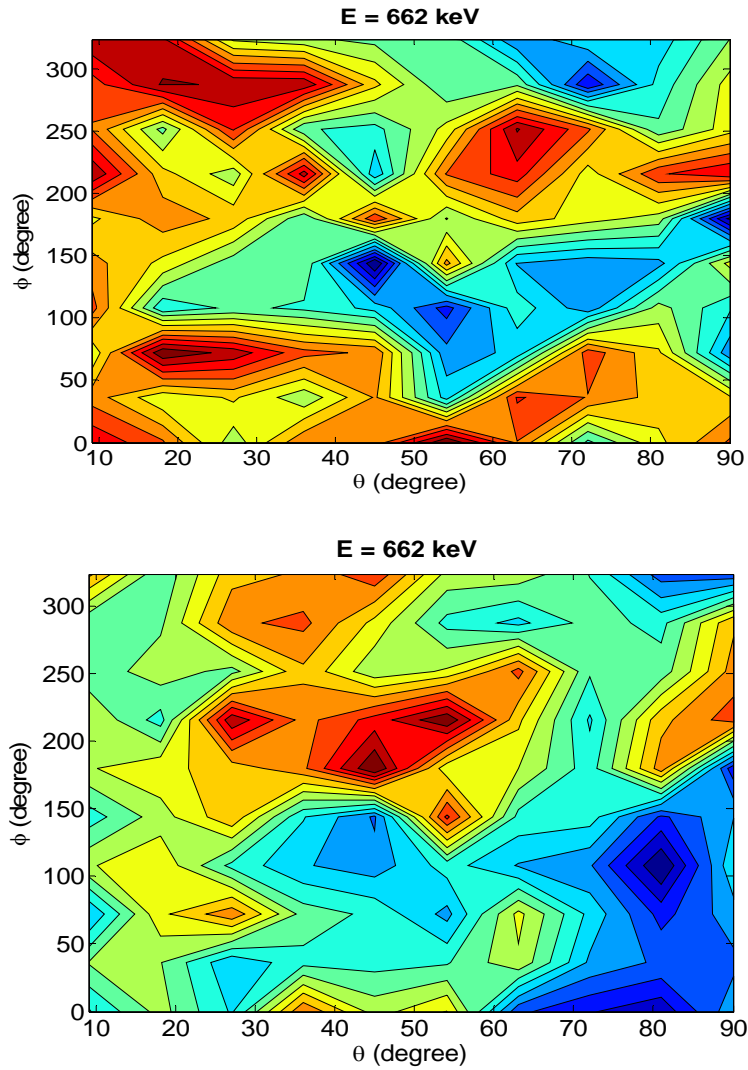


Figure 7-4. The image reconstructed by decoded the shading pattern on the bottom layer resolved with the detector array approach. On the top it was obtained from 2×10^4 events at 662 keV; on the bottom layer resolved with the detector array approach form 2×10^5 events at 662 keV.

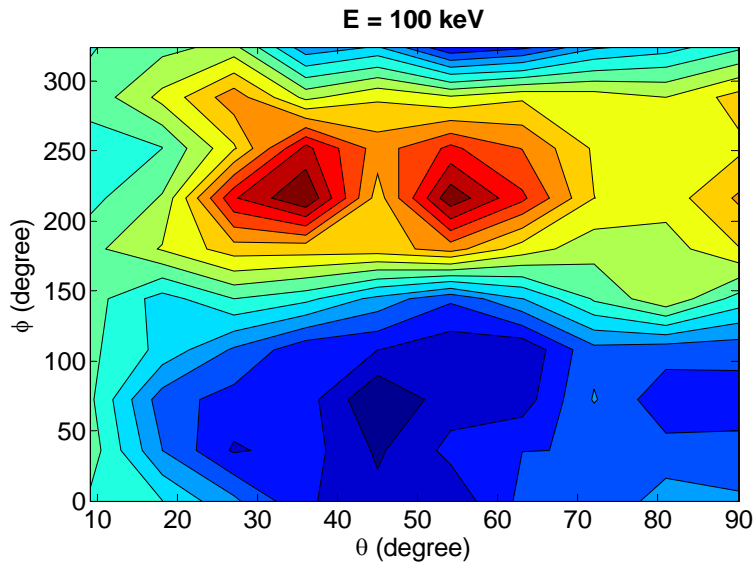


Figure 7-5. The image reconstructed by decoded the shading pattern from 2×10^4 events at 100 keV.

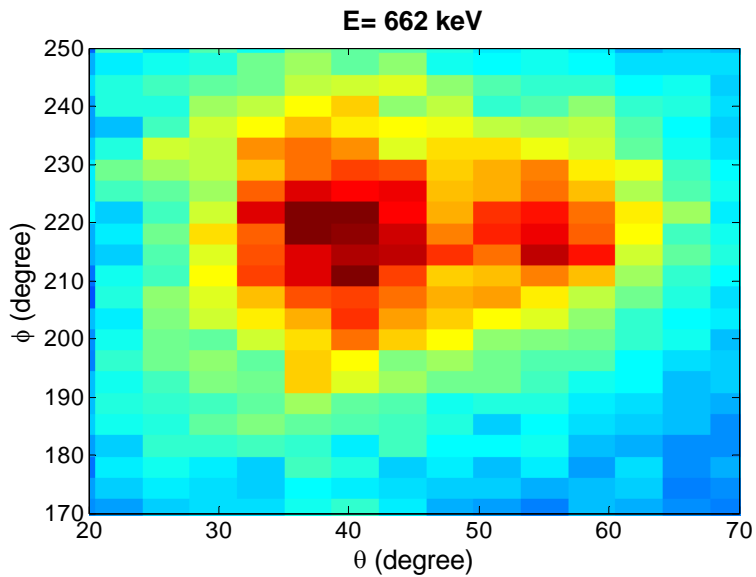


Figure 7-6. The reconstructed image of the same two sources at 662 keV with back-projection method implemented in Compton camera approach.

For incident photons at the energies of 662 keV and 100 keV, the decoded images are shown in Figures 7-4, 5. Since the decoded image of multiple point sources suffered from coincident correlation, contours of decoded image were plotted which illustrated the evolution of correlation coefficients well. Two point sources with the angular separation of ~ 0.3 radians were

resolved at 100 keV, but not at 662 keV, even with a factor of 10 increases in exposure time, due to the increase in scattering of higher energy gamma-rays. The two point sources with separation of ~0.3 radians were not noticeably resolved at 662 keV with Compton camera approach with the back-projection method, as shown in Figure 7-6.

Filtered back projection or iterative image reconstruction algorithms (such as MLEM) are needed to improve the image quality and to resolve the two point sources reliably. To apply filtered back-projection method, we need to assume that imaging system can be represented as

$$g'(\vec{\Omega}') = \int_{s^2} d\vec{\Omega} g(\vec{\Omega}) h(\cos \omega), \quad (7.4)$$

in this formula $g'(\vec{\Omega}')$ and $g(\vec{\Omega})$ were the observed and source angular distributions, respectively. The filtered back-projection method was implemented on SO(3) the group of rotations in three dimensions. Fourier Transforms and represented as

$$G_l^m = \frac{2l+1}{4\pi H_l} G_l'^m, \quad (7.5)$$

where

$$\begin{aligned} H_l &= \left(\frac{2l+1}{2} \right) f(\vec{\Omega}) = \sum_{l=0}^{+\infty} \sum_{m=-l}^l F_l^m Y_l^m(\vec{\Omega}) \\ G_l^m &= \int_{s^2} d\vec{\Omega} g(\vec{\Omega}) Y_l^{m*}(\vec{\Omega}) \\ G_l'^m &= \int_{s^2} d\vec{\Omega} g(\vec{\Omega}') Y_l^{m*}(\vec{\Omega}) \\ Y_l^m(\vec{\Omega}) &= \sqrt{\frac{(2l+1)(l-m)!}{4\pi(l+m)!}} P_l^m(\cos \theta) e^{im\phi}, \end{aligned}$$

and $P_l^m(\cos \theta)$ is the associated Legendre polynomial. The kernel $h(\cos(\omega))$ was only a function of the angle ω between $\vec{\Omega}'$ and $\vec{\Omega}$. The formula used to derived this kernel was

$$h(\cos \omega) = \frac{1}{2 \sin \frac{\omega}{2}} \sum_{in=1}^N \sum_{out=in}^N \left\{ \begin{array}{l} e^{\mu_{E_0} d_{mean}(\theta_{in}, \phi_{in})} K(\theta) \\ \times e^{\mu_{E_0-E_1} L_{out}(\theta_{out}, \phi_{out})} \\ \times (1 - e^{\mu_{E_0-E_1} d_{mean}(\theta_{out}, \phi_{out})}) \\ \times \Delta \Omega_{in,out} \end{array} \right\}, \quad (7.6)$$

where

$$K(\theta) = \begin{cases} \frac{1}{\sqrt{\cos^2 \frac{\omega}{2} - \cos^2 \theta}} \cdot \frac{1}{\sin \theta} \frac{d\sigma}{d\theta} & \text{if } \omega \in \{\omega_1, \omega_2\} \\ \frac{1}{\sqrt{4 \sin^2 \theta f(\theta) - \left[\sin^2 \theta + f(\theta) - 4 \sin^2 \frac{\omega}{2} \right]^2}} \frac{1}{\sin \theta} \frac{d\sigma}{d\theta} & \text{if } \omega \in \{[0, \omega_1] \cup [\omega_2, \pi]\} \end{cases};$$

$$\frac{1}{\sin \theta} \frac{d\sigma}{d\theta} = Z r_0^2 \pi \left(\frac{E_{\gamma_1}}{E_{\gamma_0}} \right)^2 \left(\frac{E_{\gamma_0}}{E_{\gamma_1}} + \frac{E_{\gamma_1}}{E_{\gamma_0}} - \sin^2(\theta) \right);$$

θ is the angle between (θ_{in}, ϕ_{in}) and $(\theta_{out}, \phi_{out})$;

$$f(\theta) = \frac{2}{\alpha^2 (1 - \cos \theta)} - \frac{1}{\alpha^4 (1 - \cos \theta)^2};$$

$$\omega_1 = \arccos(1 - \alpha^{-2} / 2); \quad \omega_2 = \arccos(1 - \alpha^{-1}); \quad \alpha = \frac{E}{mc^2};$$

$d_{mean}(\theta_{in}, \phi_{in})$ is the mean distance for a photon, incident from direction (θ_{in}, ϕ_{in}) , to pass before scattering; $L_{out}(\theta_{out}, \phi_{out})$ is the attenuation-path-length for a scattering photon escaping at direction $(\theta_{out}, \phi_{out})$; $\Delta \Omega_{in,out}$ is the solid angle of an absorbing detector (*out*) subtended by the scattering detector (*in*); N is the number of detectors.

These formulae take into account the attenuation in detector for both incident and scattering photons at different scattering angles and limited coverage of scattering angles [93] that corresponded to the specified locations of different detectors. The filtered back-projection was implemented with the Soft 2.0 software package [94].

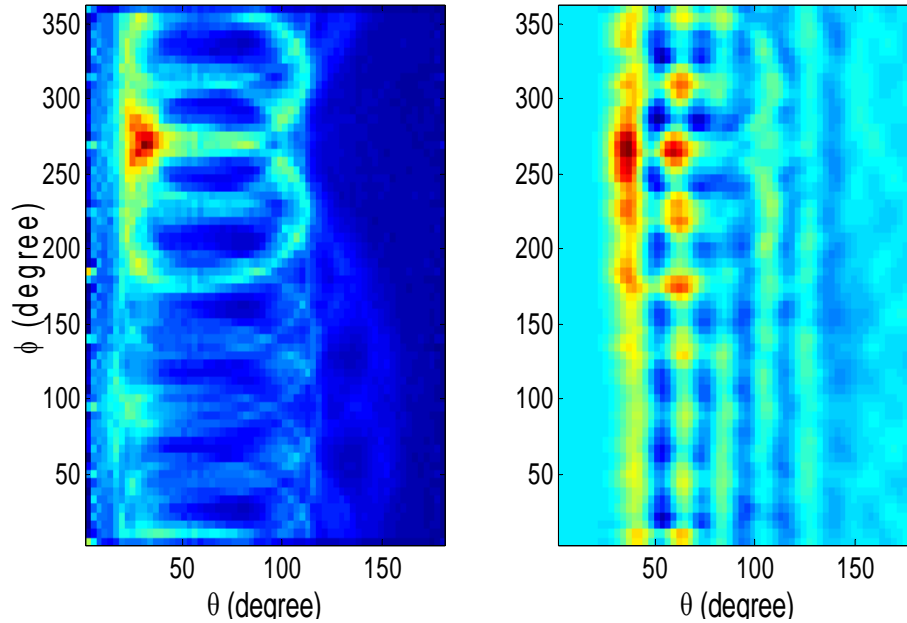


Figure 7-7 The image reconstructed with back-projection method is on the left. The image on the right is obtained with filtered back-projection method.

The image reconstructed with back-projection method is filled with artifacts. It is understandable because in our experiment with the bench top system, the back-projection image indicated that this kernel was strongly dependent on both Ω' and Ω . Therefore, the image obtained with the filtered back-projection method has other miss-resolved regions as seen in Figure 7-7.

To improve the quality of image, an iterative algorithm method was one of the choices, and has been previously applied to reconstruct the image for Compton cameras [80]. The response function of the bench top setup to two-hit events was approximated as

$$\tilde{H}_{xyzE_0}^{i,j,E_1,E_2} \propto \int_0^{E_0} \left(\Omega_{eff}(x,y,z,E_0,i) \times \frac{\partial^2 \sigma_{incoh}}{\partial(E_0-E')\partial\Omega_1} \Gamma(E_1,E') \times (1-P_{int}(i,E_0-E',j)) \times \Omega_{eff}(i,E_0-E',j) \right) \left(\int_{\Omega_2} \frac{\partial^2 \sigma_{incoh}}{\partial(E_0-E'-E'')\partial\Omega_2} \Gamma(E_2,E'') \Gamma(E_1,E') (1-P_{int}(j,E_0-E''-E'',\Omega_2)) d\Omega_2 \right) dE' \quad (7.7)$$

$$+ \int_0^{E_0-E'} \frac{d\sigma_{ph}(E_0-E',E'')}{dE''} \Gamma(E_2,E'') dE''$$

Since we were not able to distinguish which detector was interacted first among the two hit detectors, the response function of this Compton camera was proportional to the summation of the two cases: 1) an incident photon hit detector i first; and 2) the photon hit j first.

$$H_{xyzE_0}^{i,j,E_1,E_2} = \tilde{H}_{xyzE_0}^{i,j,E_1,E_2} + \tilde{H}_{xyzE_0}^{j,i,E_1,E_2} \quad (7.8)$$

$\Omega_{eff}(x,y,z,E_0,i)$ is the effective solid angle of the detector i to the point of (x,y,z) which takes into account the impact of the geometric shape of the detector i and the energy of incident photon on the interaction probability; $\Omega_{eff}(i,E_0-E',j)$ is effective solid angle of the absorbing detector j to the detector i which takes into account the impact of the geometric shape of the detectors and the energy of incident photon on the interaction probability; $P_{int}(i,E_0-E',j)$ is the average probability of a photon with energy of E_0-E' interacting with detector i ; $\Gamma(E,E')$ is the probability of photon with actual energy of E' measured as E ; $P_{int}(j,E_0-E''-E'',\Omega_2)$ is the probability of a photon interacting with detector j and escaping along the direction of Ω_2 . In our calculation, we assumed that only one interaction, either photoelectric absorption or Compton scattering, occurred and located in the center of each hit detector (to account for the fact we are not utilizing position sensitive electronics). In the image reconstruction, the efficiency (F_{eff}) of the system is needed that can be expressed as:

$$F_{eff}(x,y,z,E_0) = \sum_{\{i,j,E_1,E_2\}} H_{xyzE_0}^{i,j,E_1,E_2} \quad (7.9)$$

The calculated efficiency $F_{eff}(x, y, z, E_0)$ at $z = 1500$ cm and $E_0 = 100$ keV is shown in Figure 7-8.

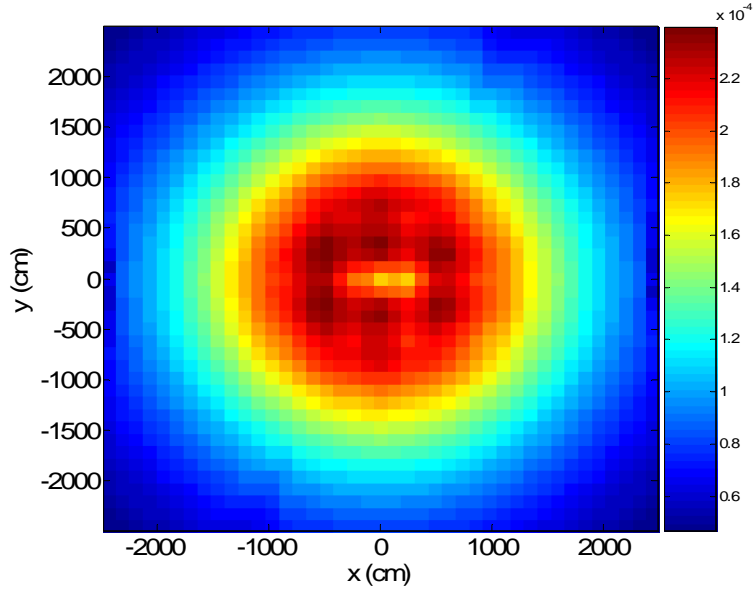


Figure 7-8. The efficiency of the hybrid camera as function of the original location of incident photons with 100 keV on XY plan at $z = 1500$ cm.

The reconstruction image of 100 keV photons from two-hit events is shown in Figure 7-12.

The two point sources were evident with the highest intensity, but artifacts were significant.

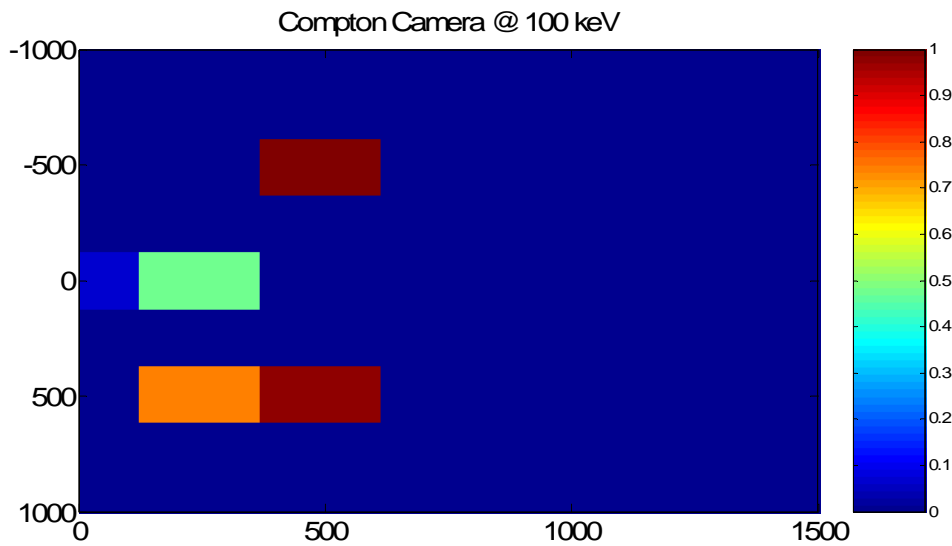


Figure 7-9. The reconstructed image of 100 keV photons from two-hit events.

Discussion

In comparison with conventional hybrid gamma camera, our design has three major advantages. First, our design does not induce additional background from scattering on an inactive coded aperture mask. Second, the active coded aperture allows us to utilize the recorded hits to improve the opaqueness of the mask elements by eliminating the events with double hits (one in scattering detector and one in absorbing detector layer). These two advantages were inherited from active coded aperture elements that were evaluated in 1980 for a coded aperture imager in 50 - 500 MeV [92]. Third, the efficiency of the hybrid camera in our design is not affected by the attenuation of the additional coded aperture in front of the scattering detectors used in conventional hybrid imaging system.

The coded aperture approach was successfully applied for 100 keV photons, but not for 662 keV photons. Our simulation showed that the modulation ratios (defined as the ratio between the difference of the maximum and the minimum counts and the mean count) were 2 and 0.4 for 100 keV and 662 keV photons, respectively. These results suggest that the coded aperture approach is capable of finding fainter sources at 100 keV because of more significant modulation than that at 662 keV.

To compare the efficiencies of the Compton camera and coded aperture, we calculated the ratios of events with one-hit at the absorbing layer and events with two-hits of any two detectors which were found to be 0.007 and 0.2 for 100 keV and 662 keV photons, respectively. This indicates that the Compton Camera approach is applicable for photons above ~ 500 keV, while the coded aperture method best serves photon energies less than 500 keV, which was consistent with the image results presented in Figures. 7-4, 5 and 7-6.

The angular resolution of this hybrid system, ~ 0.3 radians, can be achieved with simple back-projection reconstruction method, which was determined by the angular uncertainty for a

single source. Advanced image reconstruction algorithms combined detail modeling improved the spatial and contrast resolutions of image further, as seen in Figure 7-9

Conclusions

Our hybrid camera prototype with $\text{LaBr}_3(\text{Ce})$ detectors was capable of serving as both imager and spectrometer in a broad energy range from about one hundred keV to a few MeV. The angular resolution of ~ 0.3 radians was achievable with simple back-projection reconstruction method. The cycle cross correlation was successfully applied in constructing the image in the coded aperture approach implemented with one hit events. The shadow patterns used for coded aperture decoding were generated via Monte Carlo simulation at the reasonable expense of computer time when limited directions are involved and the required angular-resolution was about $\sim 10^\circ$. The feasibility of this design was demonstrated by the experimental results of the bench top configuration with two $\text{LaBr}_3:\text{(Ce)}$ detectors. In addition, iterative image algorithms were developed that improved image quality significantly.

In the future, we will investigate the possibilities and advantages of applying position sensing techniques to $\text{LaBr}_3(\text{Ce})$ detectors, such as use of a position sensitive PMT or APD. The filtered back-projection algorithm will be further investigated for a prototype with increased coverage of scattering angles. Combining one-hit data and two-hit data will also be studied, as well as combining coded aperture and Compton images.

CHAPTER 8 DESIGN OF A COMPTON IMAGING CAMERA FOR MEDICAL APPLICATIONS

Introduction

With development of 3D conformal delivering techniques of radiation dose, such as IMRT and IGRT approaches with medial of photon and proton beams, radiation therapy has become a more and more favored method to combine with chemotherapy and surgery in tumor control. With a *sharp distal* fall off in depth dose distribution, proton therapy provides a superior conformal dose compared with that of photon beams which is necessary to treat the tumor in the vicinity of critical organs, such as spinal cord, as seen in Figure 8-1 [110]. Due to the large gradient of dose, miss-location in dose delivering leads to significant change in treatment outcomes [95, 96]. In order to assure the outcome, advanced treatment planning systems and dose verification methods are crucial. The accurate and detail physical modeling assured the accuracy and precision in the calculation of the stopping power of tissues, such as that used in Monte Carlo simulation approach that is the technique near horizon of clinical application [97]. However, uncertainty in dose delivering is unavoidably induced in clinical applications from uncertainties of stopping power calculated based on the electron density derived from CT numbers, motion of patients, patient setup, and etc. Verification of dose delivering during or after treatment is highly desirable but it is still an on-going research area.

Gamma ray emission from patients during or after treatment can disclose the trace of the proton beam. There is a promising and ongoing research area in which dose distribution is reconstructed after treatment with positron emission tomography (PET) by imaging nuclear reaction products of positron emitters [98]. However, recent findings showed that biological wash out effects were difficult to model and impacted the precision of the approach with PET after treatment [99, 100, 101, and 102]. Furthermore, the work load and time-consuming

acquisition process of PET limits this approach. Imaging the prompt gamma emission during the treatment overcome those shortages with PET after treatment.

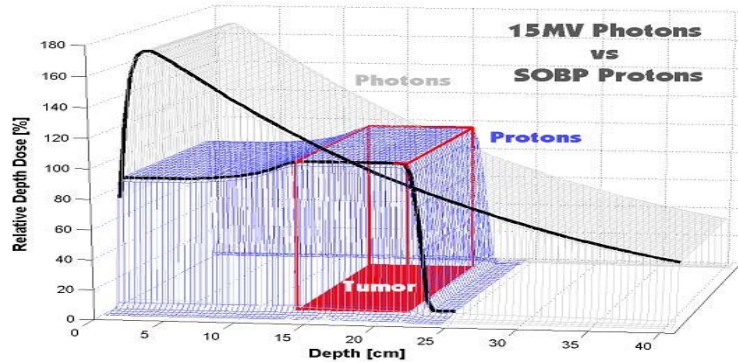


Figure 8-1. The comparison the dose delivery with proton and photon beams.

The prompt gamma rays are emitted due to inelastic scattering of protons with nuclei, neutron capture, and decay of radioisotopes generated via nucleic reaction induced by high energy protons as well known. The energy spectrum of the gamma emission is shown in Figure 8-2 and was obtained via Monte Carlo simulation based on MCNPX 2.5. Among the photons there are many gamma lines. Two gamma ray lines of 511 keV and 2.2 MeV are particularly interesting, in that they are associated with the positron emission and neutron capture, respectively.

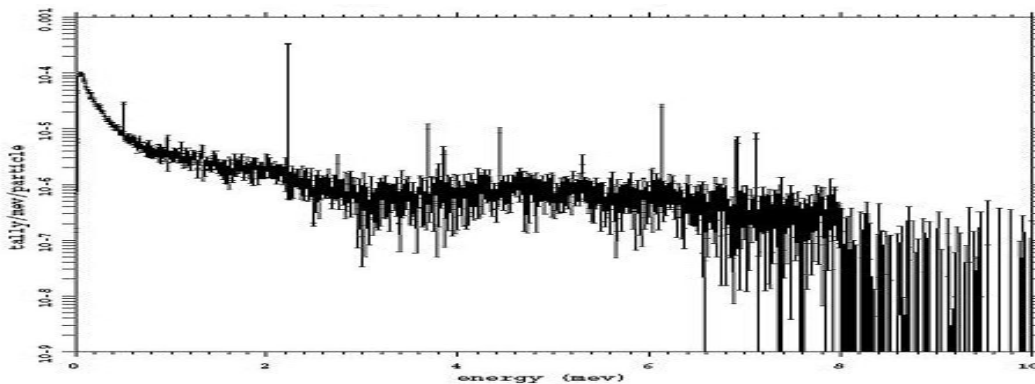


Figure 8-2. The energy spectrum of the prompt gamma emission induced by 200 MeV proton beam in water.

Although, there is large number of photons emitted during treatment with proton beam especially for photons with energies above 1 MeV, as seen in Figure 8-3, it is challenging to image gamma rays with energies above a few hundred keV because of their penetration power. Mechanical collimators have been widely applied for imaging photons below a few hundred keV but its efficiency decreases and angular resolution degrades as the energy of photons increasing. There is an alternative approach to image high energy photons with high efficiency and good resolution is the Compton camera approach which has been explored in single photon emission tomography (SPECT) and gamma-ray astrophysics. For SPECT, low Z Si material with good energy resolution is used as scattering material in order to reduce the Doppler broadening effects in imaging photons around 140 keV. For photons in high energy range, such as above 500 keV, the Doppler broadening effects are reduced and have insignificant impact on the angular resolution of Compton cameras because the energy and momentum of bounded electrons are very small compared to that of the incident photons [29].

The new scintillation material LaBr₃ with high atomic number and density provides high efficiency at a reasonable thickness. Furthermore, the good energy resolution of ~3% at 662 keV achieved in LaBr₃ detectors makes LaBr₃ to be a desirable material for Compton cameras. With the development of position sensing readout in scintillation detectors, pixelated LaBr₃ crystals have been developed for the application of TOF PET by Kuhn, *et al.* [103, 104]. The improved precision in position sensing allows LaBr₃ to be applied in the high resolution Compton cameras.

High Resolution Compton Cameras for High Energy Photons

In order to achieve a high resolution, pixelated LaBr₃ crystals were used for scattering and absorbing detectors to reduce the uncertainty in locating scattering and absorbing positions. In our design each LaBr₃ crystal module used in front layer has the size of 2.5cm x 2.5cm x 0.5cm

that was segmented into 4 mm x 4 mm x 2 mm on its top to enhance the spatial resolution based on the differential response of PSPMT that receives light. Each detector in the rear layer has the size of 2.5cm x 2.5cm x 3.0cm and was segmented into 4 mm x 4 mm x10 mm. The position resolution in locating interaction is about 2mm laterally and 2.5mm vertically in the front detectors while the resolutions are 2mm and 15 mm in the rear detectors. The efficiency and angular uncertainty of this Compton camera was investigated for photons with energies of 511 keV to 2 MeV based on numerical calculation. The geometry of the detectors and distance between detectors were optimized to achieve high efficiency or high angular resolution. The configuration of this design was combination of simplexes to assurance that the scattered photons have more chance observed at 25° - 60° scattering angles for incident photons from the region of interested which located in the center of the camera. The sizes of detectors and pixel were shown in Figure 8-3.

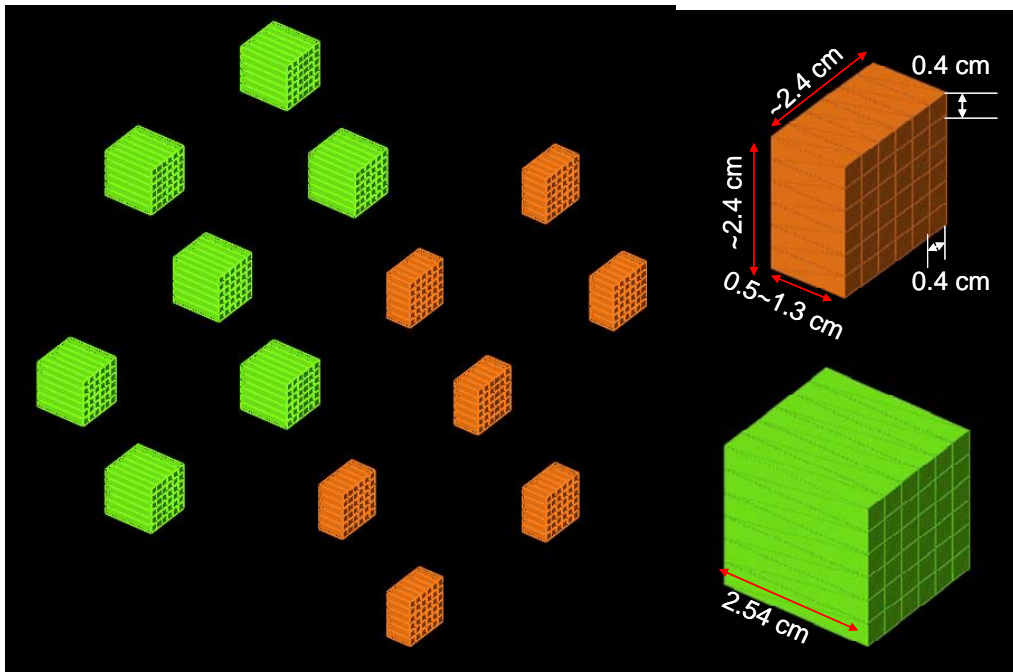


Figure 8-3. The configuration of the Compton camera is on the left. The sizes of detectors and the pixel are on the right.

During designing, we took into account the relationships between the geometries, efficiency, as seen in Figure 8-4, and angular uncertainty in order to optimize the thickness of crystals and separation of detectors to achieve the highest efficiency for a required angular resolution and vice versa. The feasibility of using LaBr_3 to build Compton camera was evaluated with the experiment of a bench top setup in Chapter 6. A prototype of Compton cameras was presented and simulated. Image reconstruction algorithms of ordered subset EM (OSEM) were applied based on physical modeling of the designed camera [53].

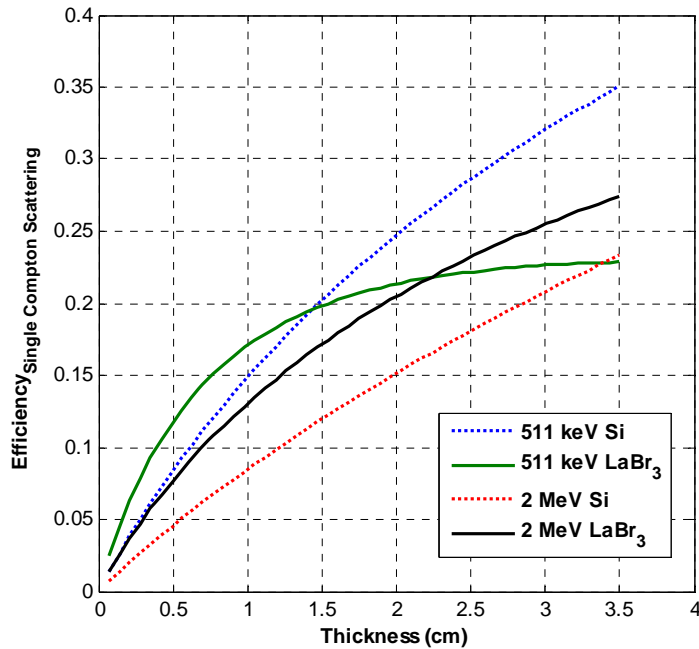


Figure 8-4. The efficiency of single Compton scattering as function of thickness of the detector.

Compton Camera Approach

In general, a Compton camera approach is implemented based on the observation of the scattering of initial photons and absorbing of the scattered photons. Therefore, the efficiency of a Compton camera is determined by the efficiency of single Compton scattering and the observing efficiency of the scattered photons. LaBr_3 crystal as scattering detector has advantages over Si

(the conventional scattering material) in efficiency of single Compton scattering at the thickness of less than 1.5 cm for photons at 511 keV (Figure 8-5). Above 2 MeV this efficiency advantage extends to a larger range of thickness from 0 to 3.5 cm.

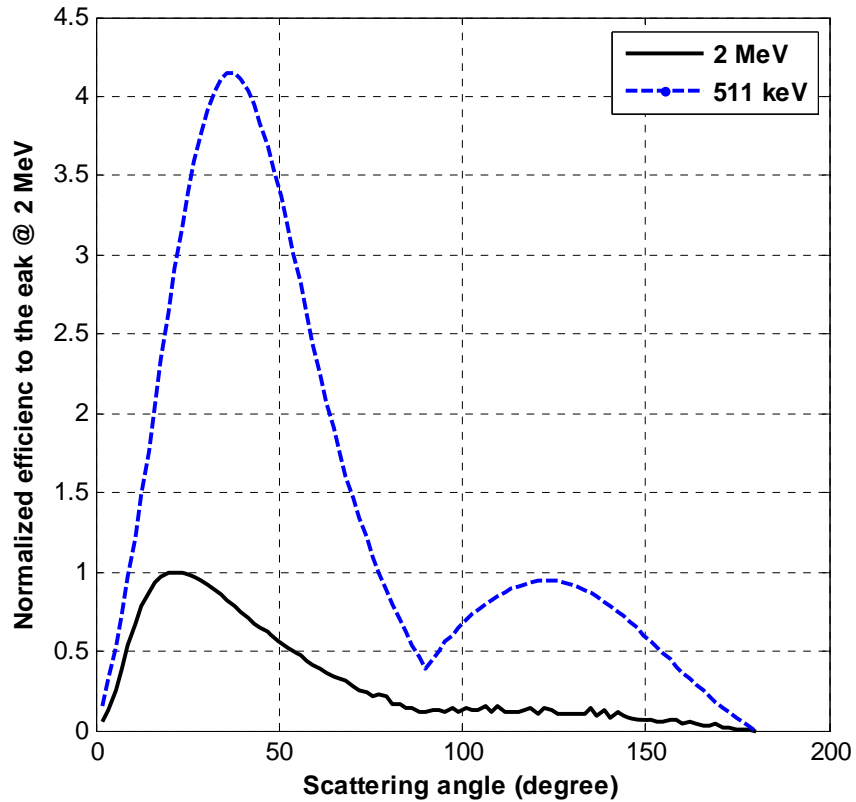


Figure 8-5. The relative efficiency as function of scattering angle for LaBr₃ Compton imaging system.

The observed efficiency of the scattered photons depends on where the absorbing detectors were placed because the probability of scattering depends on the scattering angle. The calculation shows that the probability is higher for scattering angle 40° for gamma rays at 511 keV while that is more forward to 20° for 2 MeV, as seen in Figure 8-6. However, taking into account the angular field of view of ~90°, the sensitivity of the efficiency to incident angles can

be reduced by increasing coverage of absorbing detector. That helps to suppress the artifacts in reconstructed images, especially for low statistic (poor count) cases.

The angular uncertainty in the determination scattering angle is an indicator of angular resolution that is attributed to uncertainty in positioning the interaction sites, uncertainty in the measurement of energies, and Doppler broadening. According to Figure 8-6, the separation of 10 cm between detectors in the same layer can assurance that the angular uncertainty induced from positioning uncertainty is less than 0.04 radians. The angular uncertainty induced from uncertainty in energy measurement can be constrained below 0.06 radians for 511 keV and 0.02 radians for 2 MeV gamma rays when the gamma rays are scattered with 10° to 60° , respectively, as seen in Figure 8-7. For 511-keV gamma rays, the lower limit of angular uncertainty is 0.03 radians due to the Doppler broadening effects, as shown in Figure 8-8 (the uncertainty drop above 165 degrees was attributed to truncated of energies of scattered photons above the energy of incident photons), that is 0.02 radians for 2 MeV gamma rays.

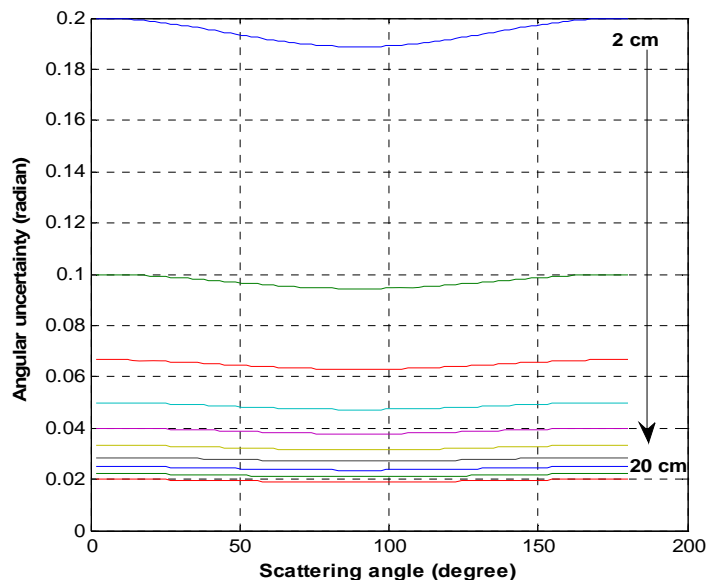


Figure 8-6. The angular uncertainty induced from positioning as function of the distance between detectors.

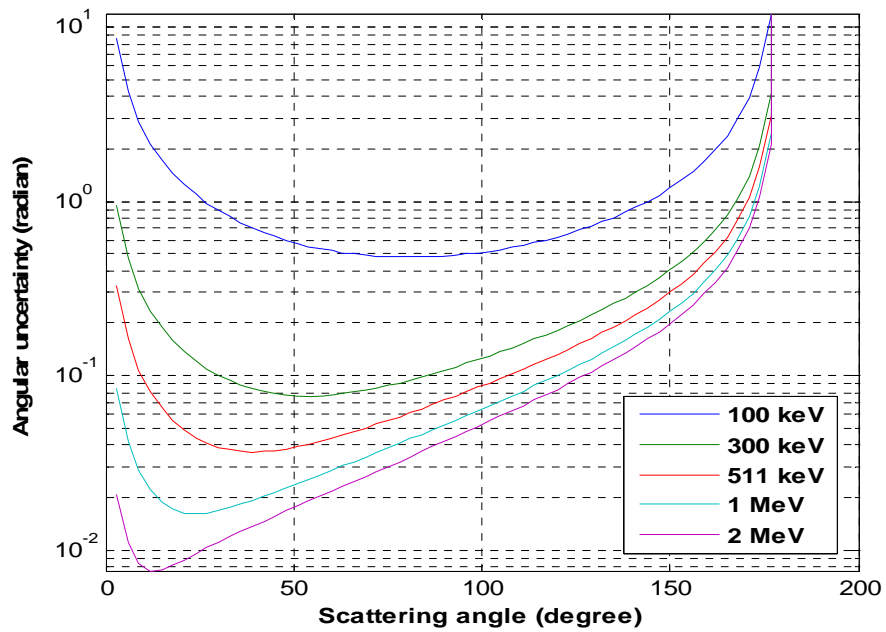


Figure 8-7. The angular uncertainty induced from uncertainty in measurement of energies as function of scattering angle.

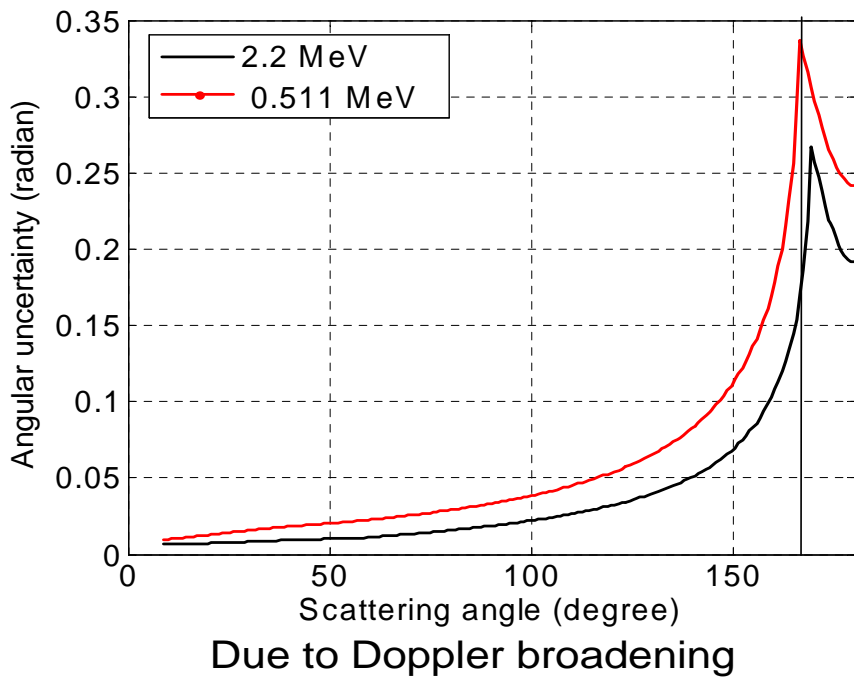


Figure 8-8. The angular uncertainty induced from Doppler broadening.

Image Reconstruction

Image reconstruction algorithms applied on the Compton camera included direct back projection, filtered back projection and iterative approaches. The back projection approaches were usually applied to obtain angular projection image of emission sources in 2D when the point spread function is approximately independent of incident direction. In order to reconstruct image in 3D, iterative algorithms were conventional choices in which detail modeling of the Compton camera in physics is allowed. Expectation maximum of likelihood (EML) method as iterative approach has been widely used in Compton cameras [53]. The general form of imaging process in Compton cameras can be represented as

$$\bar{g}_{P_1 P_2 E_1 E_2} = \sum_{xyz E_0} f_{xyz E_0} H_{xyz E_0}^{P_1 P_2 E_1 E_2} \quad (8.1)$$

An approximation of the response function of the system is represented as

$$H_{xyz E_0}^{P_1 P_2 E_1 E_2} \propto \int_0^{E_0} \left(\left(1 - P_{Absorbing}(x, y, z, E_0, P_1) \right) \Omega(x, y, z, P_1) \frac{\partial^2 \sigma_{incoh}}{\partial(E_0 - E') \partial \Omega_1} \Gamma(E_1, E') \times \left(1 - P_{Absorbing}(P_1, E_0 - E', P_2) \right) \times \right. \\ \left. \Omega(P_1, P_2) \int_0^{E_0 - E'} \left(\int_{\Omega_2} \frac{\partial^2 \sigma_{incoh}}{\partial(E_0 - E' - E'') \partial \Omega_2} \Gamma(E_2, E'') \Gamma(E_1, E') \left(1 - P_{Absorbing}(P_2, E_0 - E'' - E'', \Omega_2) \right) d\Omega_2 \right) dE'' \right) dE' \\ \left. + \int_0^{E_0 - E'} \frac{d\sigma_{ph}(E_0 - E', E'')}{dE''} \Gamma(E_2, E'') \right) dE'' \\ + \int_0^{E_0} \left(\left(1 - P_{Absorbing}(x, y, z, E_0, P_2) \right) \Omega(x, y, z, P_2) \frac{\partial^2 \sigma_{incoh}}{\partial(E_0 - E') \partial \Omega_1} \Gamma(E_2, E') \times \left(1 - P_{Absorbing}(P_2, E_0 - E', P_1) \right) \times \right. \\ \left. \Omega(P_2, P_1) \int_0^{E_0 - E'} \left(\int_{\Omega_2} \frac{\partial^2 \sigma_{incoh}}{\partial(E_0 - E' - E'') \partial \Omega_2} \Gamma(E_1, E'') \Gamma(E_2, E') \left(1 - P_{Absorbing}(P_1, E_0 - E'' - E'', \Omega_2) \right) d\Omega_2 \right) dE'' \right) dE' \\ \left. + \int_0^{E_0 - E'} \frac{d\sigma_{ph}(E_0 - E', E'')}{dE''} \Gamma(E_1, E'') \right) dE'' \quad (8.2)$$

where P1 and P2 are the two pixels points in one or two arbitrary detectors; $\Gamma(E_1, E_2)$ is probability of measuring a photon with the energy of E_1 at energy E_2 ; $P_{absorbing}(P_1, E, P_2)$ is the absorption probability of a photon with the energy of E travelling from point P₁ to P₂;

$\Omega_{eff}(x, y, z, P_1)$ is effective solid angle of the pixel I to the point of (x, y, z) which takes into account the impact of the geometric shape of the detector, location of the two pixels, and the energy of incident photon on the interaction probability; $\Omega_{eff}(P_1, P_2)$ is effective solid angle between pixel 1 and pixel 2, which takes into account the impact of the geometric shape of the detectors, location of the two pixels, and the energy of the scattered photon based on the interaction probability. In our modeling the response function, we assumed interaction located at the center of the hit pixel. The EML for the Compton camera can be represented by:

$$\hat{f}_{xyzE_0}^{n+1} = \frac{\hat{f}_{xyzE_0}^n}{\sum_{P_1P_2E_1E_2} H_{xyzE_0}^{P_1P_2E_1E_2}} \sum_{P_1P_2E_1E_2} H_{xyzE_0}^{P_1P_2E_1E_2} \frac{\mathcal{G}_{P_1P_2E_1E_2}}{\sum_{x'y'z'E} \hat{f}_{x'y'z'E}^n H_{x'y'z'E}^{P_1P_2E_1E_2}} \quad (8.3)$$

However, the large size of the response matrix of Compton cameras, there is great advantage to apply list mode approach where only the observed two-hit events appeared in summation[52, 53]:

$$\hat{f}_{xyzE_0}^{n+1} = \frac{\hat{f}_{xyzE_0}^n}{\sum_{P_1P_2E_1E_2} H_{xyzE_0}^{P_1P_2E_1E_2}} \sum_{\{P_1P_2E_1E_2: \mathcal{G}_{P_1P_2E_1E_2} \neq 0\}} H_{xyzE_0}^{P_1P_2E_1E_2} \frac{\mathcal{G}_{P_1P_2E_1E_2}}{\sum_{x'y'z'E} \hat{f}_{x'y'z'E}^n H_{x'y'z'E}^{P_1P_2E_1E_2}} \quad (8.4)$$

Another acceleration approach in image reconstruction is promising is the ordered subset where the detector bins were divided in to nG subsets

$$\{S\alpha: \alpha = 1, 2, \dots, nG\}.$$

Each iteration step divided into nG sub-steps and each sub-step involving a sut-data set whose size is nG fraction of origin data set. The OSEM iteration is represented by

$$\hat{f}_{xyzE_0}^{\alpha, n+1} = \frac{\hat{f}_{xyzE_0}^{\alpha, n}}{\sum_{P_1P_2E_1E_2 \in S\alpha} H_{xyzE_0}^{P_1P_2E_1E_2}} \sum_{P_1P_2E_1E_2 \in S\alpha} H_{xyzE_0}^{P_1P_2E_1E_2} \frac{\mathcal{G}_{P_1P_2E_1E_2}}{P^\alpha} \quad (8.5)$$

Results and Discussion

To evaluate the validation of the investigation above in guild of our design, we propose a prototype design, as seen in Figure 8-3 that is composed of two layers. Each of the layers is composed of 7 detectors of LaBr₃. The thickness of the detectors in the front layer was 0.5 cm to achieve approximately 0.25 cm of spatial resolution vertically. The detectors in the rear layer have thickness of 2.54 cm to achieve high efficiency of absorption. The separation of the detectors in the same layer was 10 cm, while the distance between the two layers was 15 cm~20 cm to reduce the angular uncertainty induced from the uncertainty of positioning vertically in the absorbing detectors because of their large thickness.

In the image reconstruction, the efficiency of the system is needed that can be expressed as:

$$F_{eff}(x, y, z) = \sum_{P_1 P_2 E_1 E_2} H_{xyz E_0}^{P_1 P_2 E_1 E_2} \quad (8.6)$$

It is a function of the original location and energy of incident photons, as shown in Figure 8-10 as an example of the efficiency map at XY plan of $z=15$ cm for photons with energy of 511 keV with arbitrary unity because we did not normalize it.

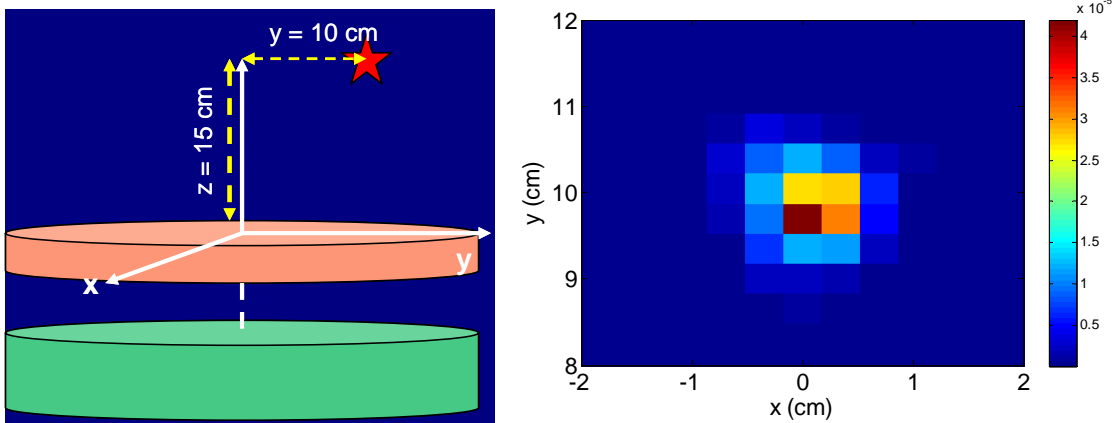


Figure 8-9. The point source and the Camera setup for simulation on the left. The point source reconstructed with OSEML from two-hit events on the right.

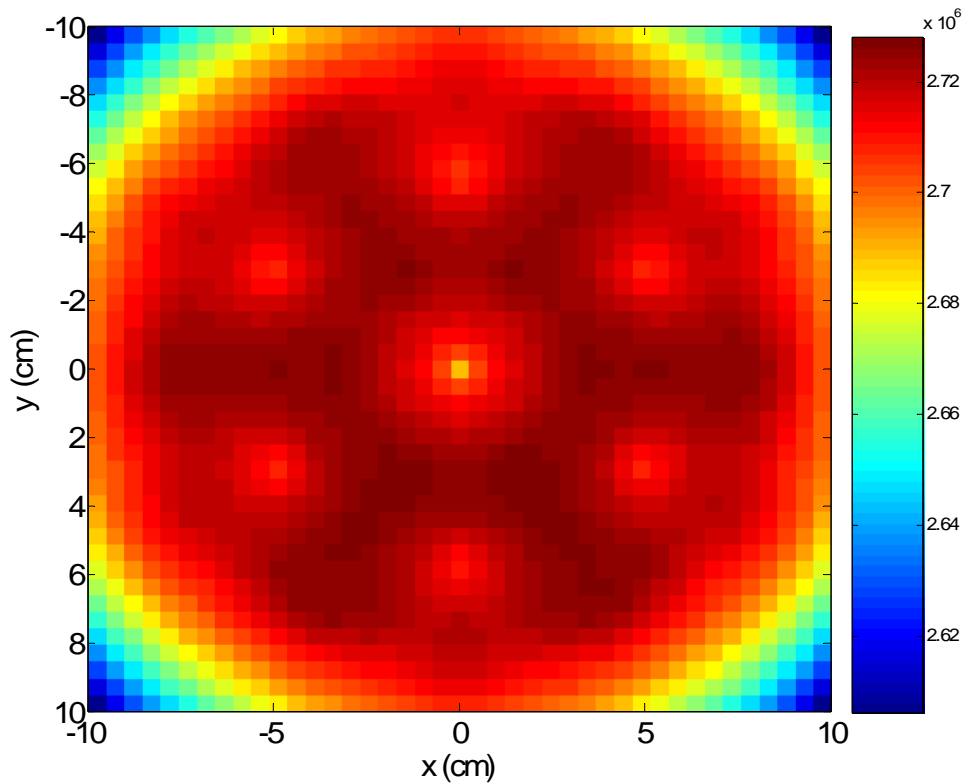


Figure 8-10 The map of the Compton camera as function of the original location of incident photons on XY plan at $z=15$ cm.

The Simulations were conducted with Geant4 (v4.92) toolkit where the deposited energies of two-hit events were recorded. The interaction locations were determined into individual pixel. The reconstructed image from a point source as shown in Figure 8-9 indicated that the spatial resolution at 15 cm depth is about 5mm. Since the large size of scattering detector array, 3-D image reconstruction was proper and the 3-D image of a point source reconstructed with OSEML was shown in Figure 8-11. In order to evaluate the acceleration rate with OS approach, the subset sizes of 100 and 1000 events were applied and the converge processes were shown in Figure 8-12. It indicated that the significant acceleration in converge speed with smaller size of

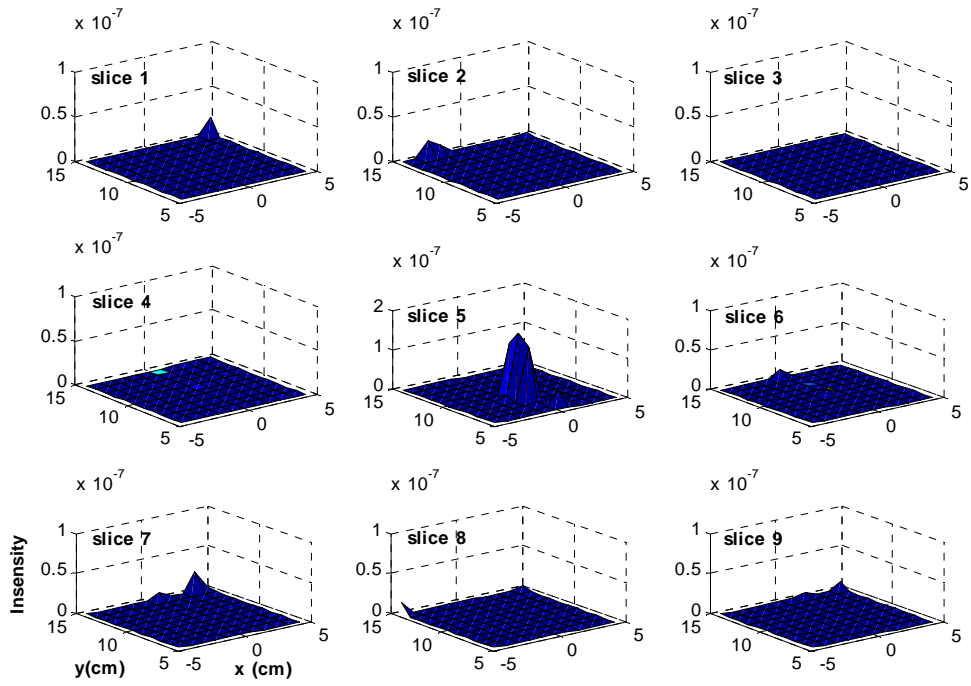


Figure 8-11. 3-D image reconstruction of a point source with OSEML algorithm. The different slices correspond to different depths.

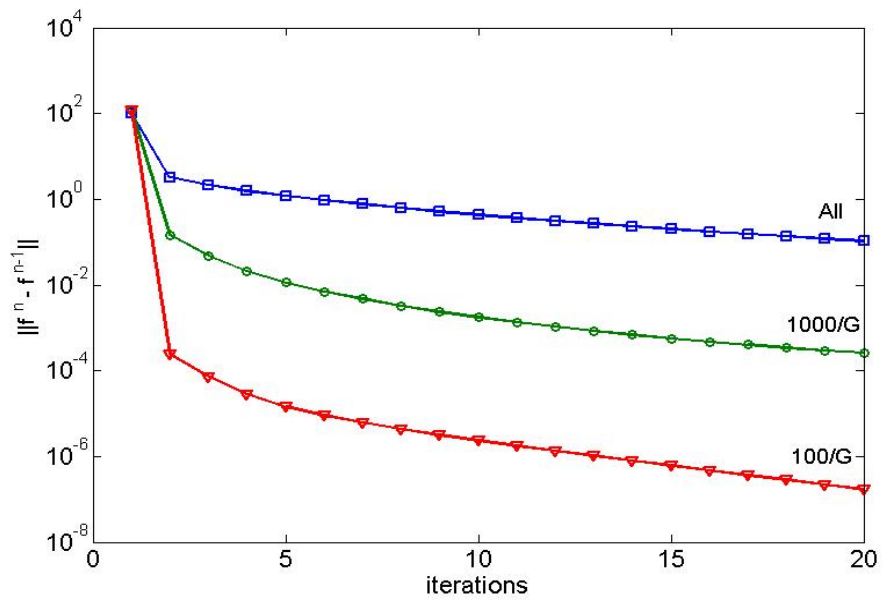


Figure 8-12. The converge speed of OSEML algorithm increased with decreasing of the size of subset.

subset. Since in medical application continuously distributed emission sources were common, we evaluated the performance of our designed camera by simulation a line source. The reconstructed images, shown in Figure 8-14, indicated that our designed camera was capable to resolve continue sources with reasonable accuracy. For 2.2 MeV photons, the image quality was degraded by poor statistics.

The low efficiency in detection of high energy photons, such as 2.2 MeV, was attributed to the lower efficiency on single Compton scattering and the adjacent two-hit events generated by high energy recoiled electrons. In order to improve the efficiency and angular resolution, we may increase the number density of detectors in both scattering and absorbing layers.

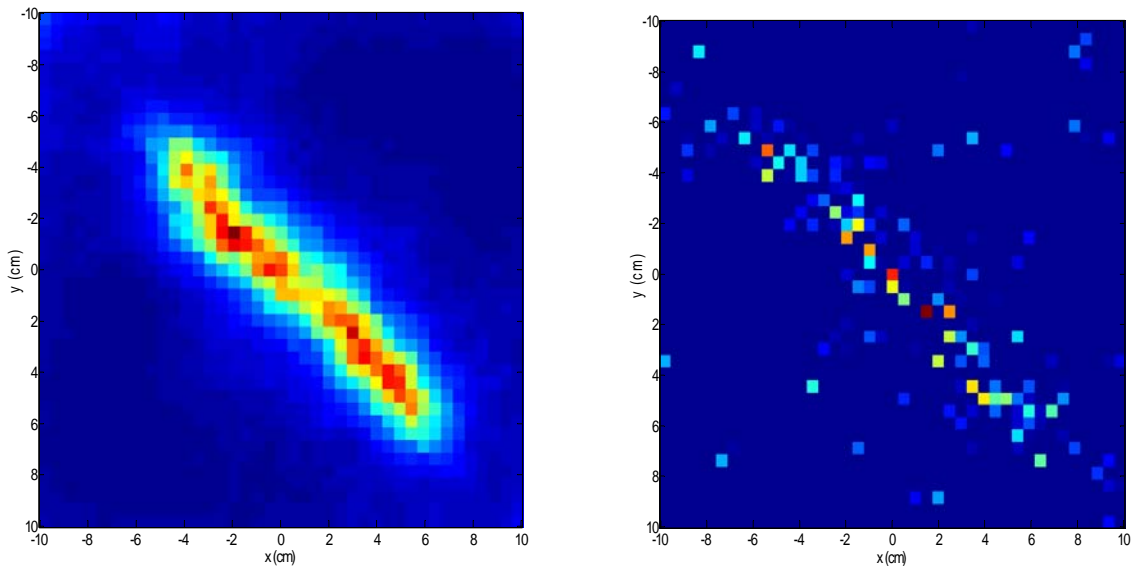


Figure 8-13. The images reconstructed with OSEML algorithm for 2×10^7 incident photons at 511 keV on the left and 2.2 MeV on the right.

The other approach is to add another Compton camera with the same configuration as shown in Figure 8-3. The two modules are arranged orthogonally, as seen in Figure 8-14. This arrangement may improve the spatial resolution in the both directions of lateral and depth,

because source position change along either direction can introduce the maximum change of incident angle to either of the module.

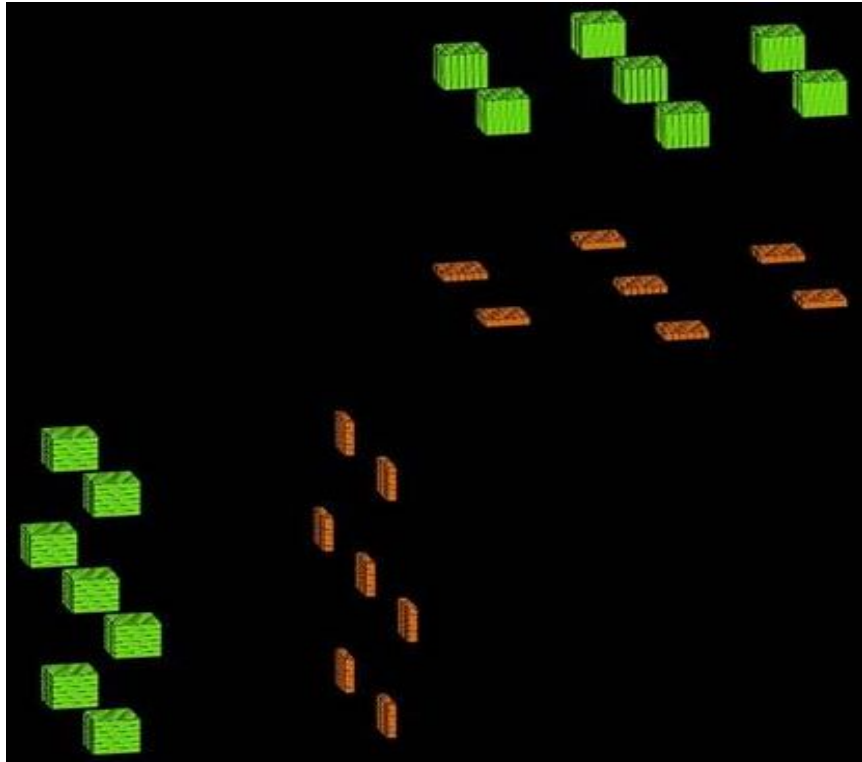


Figure 8-14. Two orthogonal Compton cameras with the same configuration of Figure 8-4.

Conclusions

The prototype Compton camera was designed based on the considerations of the efficiency and angular uncertainty. The evaluation of this design with Monte Carlo showed that imaging 0.5 – 2.2 MeV gammas can be achieved. The image reconstruction algorithm of OSEML was developed for this design and 3D image reconstruction was accomplished. The OS approach did speed up the converge speed in image reconstruction process. The spatial resolution of ~5 mm resolution was achievable at the depth of 15 cm. LaBr₃ can be used in Compton camera as both scattering and absorbing detectors for imaging high energy photons.

In order to improve the efficiency and angular resolution, we may increase the density of detectors in both scattering and absorbing layers. The other approach is to add another Compton

camera with the same configuration but put orthogonally that will improve the spatial resolution in the both directions of lateral and depth, as seen in Figure 8-15.

CHAPTER 9 CONCLUSIONS & FUTURE WORKS

Imaging and spectroscopy of gamma rays have key applications for environment and medicine. The availability of $\text{LaBr}_3:\text{Ce}$ crystals with their high light yield, fast decay provides a new opportunity for developing gamma ray imagers and spectrometers with superior performance. In my dissertation, firstly, we investigated with numerical calculations of the efficiency and angular uncertainty of Compton cameras that may be built with LaBr_3 . It showed that in high energy range Compton cameras of $\text{LaBr}_3:\text{Ce}$ can achieve higher efficiency with less thickness than that of Si the conventional material used as scattering material. Furthermore, the angular Doppler broadening effects were significantly reduced when the energies of incident photons increased to above 500 keV that means that $\text{LaBr}_3:\text{Ce}$ is an excellent material to build Compton cameras. The relationship between the efficiency, angular uncertainty, and geometries of detectors were presented also that could be used to optimize the geometries, such as the sizes of detector and separation between detectors of Compton cameras.

Secondly, the feasibility of using LaBr_3 in Compton cameras was evaluated with the experiment of the benchtop where LabView software controlled data acquisition card was used to sample the pulse profile from each detector and pulse height was measured online. After calibrating the energy of the benchtop with series of radioactive sources, the energy deposited was determined in each detector. The energy spectra of individual detector and summation of all hit detectors were constructed.

Image of a point source of $\text{Cs } 137$ was reconstructed with back-projection, filtered back-projection, iterative method of EM. Ring artifacts were evident in the image obtained with back-projection method. The filter back-projection method may apply to image systems with the response that were independent of the directions of incident photons. The low quality of image

and artifacts in reconstructed image with filtered back-projection method was obtained. It was attributed to that the response, in our case, was significantly dependent on incident directions because of the limited coverage of scattered photons observed with the absorbing detectors.

Iterative method of EML did show the promising of good quality of reconstructed images. The angular resolution was improved from ~ 0.3 radians to ~ 0.1 radians. Further more the contrast resolution of the reconstructed image was improved also, because the remove of artifacts due to physical modeling of the camera. However, artifacts were still existed that was attributed to the deviation between the real camera and approximation in its modeling because the complex geometry of the detectors.

Based on our studies of Compton cameras of LaBr_3 above, a novel design of a hybrid image system was presented for the applications of environmental and home land security with $\text{LaBr}_3:\text{Ce}$. This system composed of Compton camera and coded aperture camera. In this design an angular uncertainty of ~ 0.3 radians was achieved. In our design we used $\text{LaBr}_3:\text{Ce}$ for both scattering and absorbing detectors. The one-hit records of the absorbing detectors were utilized for implementation of coded aperture camera in which image was decoded with cycle cross correlation method or iterative method of EM. Again, the iterative did proved better image quality than that of directive decoded that was simple and fast.

The two-hit events were recorded as coincident two hits of two detectors which were utilized for implementation of Compton cameras. To reconstruct the image, we developed the image reconstruction algorithms of simple back projection and OSLEML. With the simple back projection algorithm, the angular resolution of reconstruction image was similar to the angular uncertainty about 0.3 radians, while the resolution was improved to about 0.1 radians with

OSLEML algorithm. The OSLEML method did speed up converge, but different selections of subsets may lead to local minimum because the biased sampling of data set in ordered subsets.

Our hybrid camera we used so called active elements as the coded apertures that have advantage to improve the oblique of aperture by removing the multiple hits records. Our design did not use passive aperture in the front Compton cameras which introduced scattering background to Compton cameras as that in conventional hybrid camera. The coded aperture image approach showed high efficiency and high resolution in the detection of low energy photons in the range of about 100 keV. The Compton camera approach showed high efficiency and high resolution in the detection of high energy photons in the range of about 500 keV. Combination the two approaches allowed us to achieve better quality of reconstructed image at the expense computation time.

Proton therapy with its capability of deliver shape dose distribution has gained more and more attention. Each year more and more Proton therapy facilities were built and planned to be built. However, the issue of verification of dose delivered became more crucial for proton therapy because the shape dose distributions. In order to address the issues we studied the interaction between proton beam and water with Monte Carlo simulation (MCNPX) and found prompt gamma ray emission during proton therapy treatment is closely related to energy deposition of proton beam. We proposed to image the gamma ray emission as means for dose verification in proton therapy in vivo. In order to achieve high spatial resolution for medical applications, we presented a novel design of Compton camera with pixelated $\text{LaBr}_3:\text{Ce}$ that allowed position sensing in each individual detectors and significantly reduced the angular uncertainty induce from errors in the locations of interactions. In this design spatial resolution of $\sim 5\text{mm}$ was achieved for point sources at 15 cm depth based our Monte Carlo simulation with

Geant4 toolkits. Because large area of scattering detector array, the gamma ray emission sources were able reconstructed in 3-D that was achieved with image reconstruction algorithm of OSEML. The combination of the design Compton camera and the developed OSLEML image reconstruction algorithm showed desirable performance in resolving the continue sources was demonstrated with line sources.

Generally, a Compton camera must be a spectrometer because the image process dependent on the energy resolution id each detector in the camera. In principle, the source distributions in space and energy can be reconstructed. In deed, the response functions of the Compton image systems depended on the energy of incident photons. Therefore, the simultaneous reconstruction of the image and energy spectrum of gamma ray sources was straight forward with the algorithm of OSLEML. However, the high dimension of response matrixes and their huge sizes made this simultaneous approach difficult and time consuming. With the development of computer architectures, this difficulty may be solved with application GPC or cell machine etc. Although it was difficult, it was still worth to develop this simultaneous approach, because this approach was required form applications where the energies of incident photons were unknown, such as gamma emission in proton therapy treatment.

For high resolution applications, position sensing in each individual detector was critical. The pixelated $\text{LaBr}_3:\text{Ce}$ was the one possible approach to achieved the position sensing. The mircocolumn $\text{LaBr}_3:\text{Ce}$ may be another promising approach to achieve position sensing.

APPENDIX A
CODES FOR HYBRID CAMERA IN GEANT

```
#include <stdio.h>

#include <stdlib.h>

#include "DetectorConstruction.hh"

#include "DetectorMessenger.hh"

#include "G4Material.hh"

#include "G4Box.hh"

#include "G4Tubs.hh"

#include "G4LogicalVolume.hh"

#include "G4PVPlacement.hh"

#include "G4PVReplica.hh"

#include "G4UniformMagField.hh"

#include "G4GeometryManager.hh"

#include "G4PhysicalVolumeStore.hh"

#include "G4LogicalVolumeStore.hh"

#include "G4SolidStore.hh"

#include "G4MultiFunctionalDetector.hh"

#include "G4SDManager.hh"

#include "G4VisAttributes.hh"

#include "G4Colour.hh"

//=====

DetectorConstruction::DetectorConstruction()

:ScatterMaterial(0),AbsorberMaterial(0),GapMaterial(0),defaultMaterial(0),
```

```

solidWorld(0),logicWorld(0),physiWorld(0),
solidCamera(0),logicCamera(0),physiCamera(0),
solidLayer(0),logicLayer(0),physiLayer(0),
solidScatter(0),
solidAbsorber(0),solidGap (0),logicGap (0),physiGap (0),
magField(0)
{
// default parameter values of the Cameraimeter
AbsorberThickness = 2.54 *cm;
AbsorberRadius   = 2.54/2 *cm;
ScatterThickness = 1.3 *cm;
ScatterRadius    = 2.54/2 *cm;
Distance_Z       = 30. *cm;
Distance_Y       = AbsorberRadius*5;
GapThickness     = 60.0*cm;
NbOfLayers       = 1;
NbOfScatters     = 40;
NbOfAbsorbers    = 100;
CameraSizeXY     = (ScatterRadius*8 + AbsorberRadius*10)*2;
ComputeCameraParameters();
// materials
DefineMaterials();
SetScatterMaterial("LaBr3");

```

```

SetAbsorberMaterial("LaBr3");

SetGapMaterial("Air");

// create commands for interactive definition of the Cameraimeter

detectorMessenger = new DetectorMessenger(this);

}

//=====

DetectorConstruction::~DetectorConstruction()
{ delete detectorMessenger;}

//=====

G4VPhysicalVolume* DetectorConstruction::Construct()
{
return ConstructCameraimeter();
}

//=====

void DetectorConstruction::DefineMaterials()
{
//This function illustrates the possible ways to define materials

G4String symbol;      //a=mass of a mole;
G4double a, z, density; //z=mean number of protons;

```

```

G4int iz, n;          //iz=number of protons in an isotope;
                      // n=number of nucleons in an isotope;

G4int ncomponents, natoms;

G4double abundance, fractionmass;

//

// define Elements

G4Element* H = new G4Element("Hydrogen",symbol="H" , z= 1., a= 1.01*g/mole);
G4Element* C = new G4Element("Carbon" ,symbol="C" , z= 6., a= 12.01*g/mole);
G4Element* N = new G4Element("Nitrogen",symbol="N" , z= 7., a= 14.01*g/mole);
G4Element* O = new G4Element("Oxygen" ,symbol="O" , z= 8., a= 16.00*g/mole);
G4Element* Si = new G4Element("Silicon",symbol="Si" , z= 14., a= 28.09*g/mole);
G4Element* Br = new G4Element("Bromine",symbol="Br" , z= 35., a= 79.904*g/mole);
G4Element* La = new G4Element("Lanthanum",symbol="La" , z= 57., a= 138.90547*g/mole);

//

// define simple materials

new G4Material("Aluminium" , z=13., a=26.98*g/mole, density=2.700*g/cm3);
new G4Material("liquidArgon" , z=18., a= 39.95*g/mole, density= 1.390*g/cm3);
new G4Material("Lead" , z=82., a= 207.19*g/mole, density= 11.35*g/cm3);

//

// define a material from elements. case 1: chemical molecule

G4Material* LaBr3 =
new G4Material("LaBr3",density= 5.300*g/cm3, ncomponents=2);
LaBr3->AddElement(La, natoms=1);

```

```

LaBr3->AddElement(Br , natoms=3);

// define a material from elements.  case 2: mixture by fractional mass
//

G4Material* Air =
new G4Material("Air" , density= 1.290*mg/cm3, ncomponents=2);
Air->AddElement(N, fractionmass=0.7);
Air->AddElement(O, fractionmass=0.3);

// vacuum

G4Material* Vacuum =
new G4Material("Galactic", z=1., a=1.01*g/mole,density= universe_mean_density,
               kStateGas, 2.73*kelvin, 3.e-18*pascal);

G4Material* beam =
new G4Material("Beam", density= 1.e-5*g/cm3, ncomponents=1,
               kStateGas, STP_Temperature, 2.e-2*bar);

beam->AddMaterial(Air, fractionmass=1.);

G4cout << *(G4Material::GetMaterialTable()) << G4endl;

//default materials of the World

defaultMaterial = Air;

ScatterMaterial = LaBr3;

AbsorberMaterial = LaBr3;

}

// =====

```

```

G4VPhysicalVolume* DetectorConstruction::ConstructCameraimeter()
{
    G4double pi=3.14159265;

    // Clean old geometry, if any
    //

    G4GeometryManager::GetInstance()->OpenGeometry();
    G4PhysicalVolumeStore::GetInstance()->Clean();
    G4LogicalVolumeStore::GetInstance()->Clean();
    G4SolidStore::GetInstance()->Clean();

    // complete the Camera parameters definition
    ComputeCameraParameters();

    //

    // World
    //

    solidWorld = new G4Box("World", //its name
                          WorldSizeXY/2,WorldSizeXY/2,WorldSizeZ/2); //its size

    logicWorld = new G4LogicalVolume(solidWorld, //its solid
                                     defaultMaterial, //its material
                                     "World"); //its name

    physiWorld = new G4PVPlacement(0, //no rotation
                                   G4ThreeVector(), //at (0,0,0)

```

```

        logicWorld,           //its logical volume
        "World",             //its name
        0,                   //its mother volume
        true,                //no boolean operation
        0);                 //copy number

//

// Camera

solidCamera=0; logicCamera=0; physiCamera=0;
if (CameraThickness > 0.)
{
    solidCamera = new G4Box("Cameraimeter",           //its name
        CameraSizeXY/2, CameraSizeXY/2, CameraThickness/2); //size
    logicCamera = new G4LogicalVolume(solidCamera,     //its solid
        defaultMaterial, //its material
        "Cameraimeter"); //its name

    physiCamera = new G4PVPlacement(0,                //no rotation
        G4ThreeVector(0,0,WorldSizeZ/2-CameraThickness/2), //at (0,0,0)
        logicCamera, //its logical volume
        "Cameraimeter", //its name
        logicWorld, //its mother volume
        true, //no boolean operation
        0); //copy number
}

```

```
//  
  
// Scatter  
  
if (ScatterThickness > 0.)  
  
    {  
  
        solidScatter = new G4Tubs("Scatter",           //its name  
  
                                0.0, ScatterRadius, ScatterThickness/2,0.0,2*pi); //size  
  
G4int PS[40]= {  
  
    1,  
  
    4,  
  
    6,  
  
    9,  
  
    11,  
  
    12,  
  
    16,  
  
    17,  
  
    20,  
  
    21,  
  
    25,  
  
    26,  
  
    28,  
  
    31,  
  
    33,
```

36,
37,
38,
39,
40,
42,
43,
44,
45,
46,
49,
51,
54,
56,
57,
61,
62,
65,
66,
70,
71,
73,
76,

```

78,
81};

G4int iy;

G4int ix;

for(size_t i=0;i<40;i++)
{
    char IDS[20];

    sprintf(IDS,"%d",i+1);

    logicScatter[i] = new G4LogicalVolume(solidScatter, //its solid
                                         ScatterMaterial, //its material
                                         IDS); //its name

    iy=ceil(PS[i]/9);
    ix=PS[i]-9*(iy);

    G4cout<< "Xs= "<< 2.5*ScatterRadius*(ix)-2.5*ScatterRadius*4<<" Ys=
"<<2.5*ScatterRadius*(iy)-2.5*ScatterRadius*4.5<< " Zs = "<<-
CameraThickness/2+ScatterThickness/2<< G4endl;

    physiScatter[i] = new G4PVPlacement(0, //no rotation
                                         G4ThreeVector(2.5*ScatterRadius*(ix)-
2.5*ScatterRadius*4,2.5*ScatterRadius*(iy)-2.5*ScatterRadius*4.5,-
CameraThickness/2+ScatterThickness/2), //its position
                                         logicScatter[i], //its logical volume
                                         IDS, //its name
                                         logicCamera, //its mother

```

```

true, //no boolean operat
0); //copy number

}
}
//
// Absorber
if (AbsorberThickness > 0.)
{
char IDA[20];
solidAbsorber = new G4Tubs("Absorber", //its name
0.0, AbsorberRadius, AbsorberThickness/2,0.0,2*pi);
G4int ii=100;
for(int i=0;i<10;i++)
{
for(size_t j=0;j<10;j++)
{
sprintf(IDA,"%d",ii);
ii++;
logicAbsorber[i*10+j] = new G4LogicalVolume(solidAbsorber, //its solid
AbsorberMaterial, //its material
AbsorberMaterial->GetName()); //name

```

```

G4cout<<" Xa= "<< 2.5*AbsorberRadius*(i)-2.5*ScatterRadius*4.5<<"
Ya="<<2.5*AbsorberRadius*(j)-2.5*ScatterRadius*4.5<<" Za = "<<-
CameraThickness/2+ScatterThickness/2+AbsorberThickness/2+Distance_Z<<G4endl;

    physiAbsorber[i*10+j] = new G4PVPlacement(0,                //no rotation
        G4ThreeVector(2.5*AbsorberRadius*(i)-
2.5*ScatterRadius*4.5,2.5*AbsorberRadius*(j)-2.5*ScatterRadius*4.5,-
CameraThickness/2+ScatterThickness/2+AbsorberThickness/2+Distance_Z), //its position
        logicAbsorber[i*10+j], //its logical volume
        IDA, //its name
        logicCamera, //its mother
        true, //no boolean operat
        0); //copy number
    }
}
}
PrintCameraParameters();

//
// Visualization attributes
//

logicWorld->SetVisAttributes (G4VisAttributes::Invisible);
G4VisAttributes* simpleBoxVisAtt= new G4VisAttributes(G4Colour(1.0,1.0,1.0));
simpleBoxVisAtt->SetVisibility(false);

```

```

logicCamera->SetVisAttributes(simpleBoxVisAtt);

// with the interactive expansion / contraction geometry system of the
// vis/OpenInventor driver :

{G4VisAttributes* simpleBoxVisAtt= new G4VisAttributes(G4Colour(0.5,1.0,0.15));
simpleBoxVisAtt->SetVisibility(false);

  logicCamera->SetVisAttributes(simpleBoxVisAtt);}

{G4VisAttributes* atb= new G4VisAttributes(G4Colour(1.0,.5,0.1));
atb->SetForceSolid(true);
for(int i=0;i<40;i++)
  {
  logicScatterer[i]->SetVisAttributes(atb);
  }
}

{G4VisAttributes* atb= new G4VisAttributes(G4Colour(0.5,2.0,0.1));
atb->SetForceSolid(true);
for(int i=0;i<100;i++)
  {
  logicAbsorber[i]->SetVisAttributes(atb);
  }
}

//
return physiWorld;
}

```

```

//=====
void DetectorConstruction::PrintCameraParameters()
{
    G4cout << "\n-----"
        << "\n--> The camera is " << NbOfScatters << " scatters of: [ "
        << ScatterThickness/mm << "mm of " << ScatterMaterial->GetName()
        << " + "
        << NbOfAbsorbers<<" absorbers of: ["
        <<AbsorberThickness/mm << "mm of " << AbsorberMaterial->GetName()
        << "\n-----\n";
}

```

```

//=====
void DetectorConstruction::SetScatterMaterial(G4String materialChoice)
{
    // search the material by its name
    G4Material* pttoMaterial = G4Material::GetMaterial(materialChoice);
    if (pttoMaterial) ScatterMaterial = pttoMaterial;
}

```

```

//=====
void DetectorConstruction::SetAbsorberMaterial(G4String materialChoice)
{
    // search the material by its name
    G4Material* pttoMaterial = G4Material::GetMaterial(materialChoice);

```

```

    if (pttoMaterial) AbsorberMaterial = pttoMaterial;
}

//=====

void DetectorConstruction::SetGapMaterial(G4String materialChoice)
{
    // search the material by its name

    G4Material* pttoMaterial = G4Material::GetMaterial(materialChoice);
    if (pttoMaterial) GapMaterial = pttoMaterial;
}

//=====

void DetectorConstruction::SetScatterThickness(G4double val)
{
    // change Scatter thickness and recompute the Cameraimeter parameters

    ScatterThickness = val;
}

//=====

void DetectorConstruction::SetAbsorberThickness(G4double val)
{
    // change Absorber thickness and recompute the Cameraimeter parameters

    AbsorberThickness = val;
}

//=====

void DetectorConstruction::SetGapThickness(G4double val)

```

```

{
    // change Gap thickness and recompute the Cameraimeter parameters
    GapThickness = val;
}

//=====

void DetectorConstruction::SetCameraSizeXY(G4double val)
{
    // change the transverse size and recompute the Cameraimeter parameters
    CameraSizeXY = val;
}

//=====

void DetectorConstruction::SetNbOfLayers(G4int val)
{
    NbOfLayers = val;
}

//=====

#include "G4FieldManager.hh"
#include "G4TransportationManager.hh"

void DetectorConstruction::SetMagField(G4double fieldValue)
{
    //apply a global uniform magnetic field along Z axis
    G4FieldManager* fieldMgr
    = G4TransportationManager::GetTransportationManager()->GetFieldManager();
}

```

```

if(magField) delete magField;           //delete the existing magn field
if(fieldValue!=0.)                      // create a new one if non nul
{
  magField = new G4UniformMagField(G4ThreeVector(0.,0.,fieldValue));
  fieldMgr->SetDetectorField(magField);
  fieldMgr->CreateChordFinder(magField);
} else {
  magField = 0;
  fieldMgr->SetDetectorField(magField);
}
}

//=====

#include "G4RunManager.hh"

void DetectorConstruction::UpdateGeometry()
{
  G4RunManager::GetRunManager()->DefineWorldVolume(ConstructCameraimeter());
}

```

APPENDIX B
CODES FOR COMPTON CAMER IN GEANT

```
#include <stdio.h>

#include <stdlib.h>

#include "DetectorConstruction.hh"

#include "DetectorMessenger.hh"

#include "G4Material.hh"

#include "G4Box.hh"

#include "G4Tubs.hh"

#include "G4LogicalVolume.hh"

#include "G4PVPlacement.hh"

#include "G4PVReplica.hh"

#include "G4UniformMagField.hh"

#include "G4GeometryManager.hh"

#include "G4PhysicalVolumeStore.hh"

#include "G4LogicalVolumeStore.hh"

#include "G4SolidStore.hh"

#include "G4MultiFunctionalDetector.hh"

#include "G4SDManager.hh"

#include "G4VisAttributes.hh"

#include "G4Colour.hh"

//=====
```

```

DetectorConstruction::DetectorConstruction()
:ScatterMaterial(0),AbsorberMaterial(0),GapMaterial(0),defaultMaterial(0),
solidWorld(0),logicWorld(0),physiWorld(0),
solidCamera(0),logicCamera(0),physiCamera(0),
solidLayer(0),logicLayer(0),physiLayer(0),
solidScatterPixel(0),
solidAbsorberPixel(0),solidGap (0),logicGap (0),physiGap (0)
{
// default parameter values of the Cameraimeter
N_X_Pixel_Abs = 6;
N_Y_Pixel_Abs = 6;
N_X_Pixel_Scat =6;
N_Y_Pixel_Scat =6;
NbOfAbsorbers = 7;
NbOfScatters= 7;
AbsorberThickness   = 2.54 *cm;
AbsPixelThickness = AbsorberThickness;
AbsPixelSizeXY      = 0.4 *cm;
AbsorberSizeXY      = AbsPixelSizeXY*N_X_Pixel_Abs;
ScatterThickness    = 0.5 *cm;
ScatPixelThickness  = ScatterThickness;
ScatPixelSizeXY     = 0.4 *cm;
ScatterSizeXY       = ScatPixelSizeXY*N_X_Pixel_Scat;

```

```

Distance_Z      = 15.0 *cm;
Distance_Scatter = 10.0 *cm;
Distance_Absorber = 10.0 *cm;
GapThickness    = 30.0*cm;
NbOfAbs_Pixel   = N_X_Pixel_Abs*N_X_Pixel_Abs*NbOfAbsorbers;
NbOfScat_Pixel  = N_X_Pixel_Scat*N_X_Pixel_Scat*NbOfScatters;
CameraSizeXY    = Distance_Scatter*3;
CameraThickness = 1.2*(ScatterThickness + AbsorberThickness+Distance_Z);
ComputeCameraParameters();

// materials
DefineMaterials();
SetScatterMaterial("LaBr3");
SetAbsorberMaterial("LaBr3");
SetGapMaterial("Air");

// create commands for interactive definition of the Cameraimeter
detectorMessenger = new DetectorMessenger(this);
}

//=====

DetectorConstruction::~DetectorConstruction()
{ delete detectorMessenger;}

//=====

G4VPhysicalVolume* DetectorConstruction::Construct()
{

```

```

return ConstructCamera();

}

//=====

void DetectorConstruction::DefineMaterials()
{
//This function illustrates the possible ways to define materials

G4String symbol;      //a=mass of a mole;

G4double a, z, density; //z=mean number of protons;

G4int iz, n;          //iz=number of protons in an isotope;

                        // n=number of nucleons in an isotope;

G4int ncomponents, natoms;

G4double abundance, fractionmass;

//

// define Elements

G4Element* H = new G4Element("Hydrogen",symbol="H" , z= 1., a= 1.01*g/mole);
G4Element* C = new G4Element("Carbon" ,symbol="C" , z= 6., a= 12.01*g/mole);
G4Element* N = new G4Element("Nitrogen",symbol="N" , z= 7., a= 14.01*g/mole);
G4Element* O = new G4Element("Oxygen" ,symbol="O" , z= 8., a= 16.00*g/mole);
G4Element* Si = new G4Element("Silicon",symbol="Si" , z= 14., a= 28.09*g/mole);
G4Element* Br = new G4Element("Bromine",symbol="Br" , z= 35., a= 79.904*g/mole);
G4Element* La = new G4Element("Lanthanum",symbol="La" , z= 57., a= 138.90547*g/mole);
new G4Material("Aluminium" , z=13., a=26.98*g/mole, density=2.700*g/cm3);
G4Material* LaBr3 =

```

```

new G4Material("LaBr3",density= 5.300*g/cm3, ncomponents=2);
LaBr3->AddElement(La, natoms=1);
LaBr3->AddElement(Br , natoms=3);

// define a material from elements. case 2: mixture by fractional mass
G4Material* Air =
new G4Material("Air" , density= 1.290*mg/cm3, ncomponents=2);
Air->AddElement(N, fractionmass=0.7);
Air->AddElement(O, fractionmass=0.3);

// define a material from elements and/or others materials (mixture of mixtures)
G4Material* Aerog =
new G4Material("Aerogel", density= 0.200*g/cm3, ncomponents=3);
Aerog->AddMaterial(SiO2, fractionmass=62.5*perCent);
Aerog->AddMaterial(H2O , fractionmass=37.4*perCent);
Aerog->AddElement (C , fractionmass= 0.1*perCent);

// vacuum
G4Material* Vacuum =
new G4Material("Galactic", z=1., a=1.01*g/mole,density= universe_mean_density,
              kStateGas, 2.73*kelvin, 3.e-18*pascal);

G4Material* beam =
new G4Material("Beam", density= 1.e-5*g/cm3, ncomponents=1,
              kStateGas, STP_Temperature, 2.e-2*bar);
beam->AddMaterial(Air, fractionmass=1.);

G4cout << *(G4Material::GetMaterialTable()) << G4endl;

```

```

//default materials of the World

defaultMaterial = Air;

ScatterMaterial = LaBr3;

AbsorberMaterial = LaBr3;

}

//=====

G4VPhysicalVolume* DetectorConstruction::ConstructCamera()

{

    G4double pi=3.14159265;

    // Clean old geometry, if any

    //

    G4GeometryManager::GetInstance()->OpenGeometry();

    G4PhysicalVolumeStore::GetInstance()->Clean();

    G4LogicalVolumeStore::GetInstance()->Clean();

    G4SolidStore::GetInstance()->Clean();

    // World

    //

    solidWorld = new G4Box("World", //its name

        WorldSizeXY/2,WorldSizeXY/2,WorldSizeZ/2); //its size

    logicWorld = new G4LogicalVolume(solidWorld, //its solid

        defaultMaterial, //its material

        "World"); //its name

    physiWorld = new G4PVPlacement(0, //no rotation

```

```

        G4ThreeVector(), //at (0,0,0)
        logicWorld, //its logical volume
        "World", //its name
        0, //its mother volume
        true, //no boolean operation
        0); //copy number

// Cameraimeter

solidCamera=0; logicCamera=0; physiCamera=0;
if (CameraThickness > 0.)
{ solidCamera = new G4Box("Camera", //its name
        CameraSizeXY/2, CameraSizeXY/2, CameraThickness/2); //size
        logicCamera = new G4LogicalVolume(solidCamera, //its solid
        defaultMaterial, //its material
        "Camera"); //its name
        physiCamera = new G4PVPlacement(0, //no rotation
        G4ThreeVector(0,0,0), //at (0,0,0)
        logicCamera, //its logical volume
        "Camera", //its name
        logicWorld, //its mother volume
        true, //no boolean operation
        0); //copy number
}
//

```

```

// Scatter
//
G4double xp,yp,zp;
G4int i_Pixel_Scat=0;
char IDS[20];
G4double XScat, YScat, ZScat;
ZScat = -CameraThickness/2 + ScatPixelThickness/2;
if (ScatterThickness > 0.)
{
solidScatterPixel = new G4Box("Scatter", //its name
ScatPixelSizeXY/2, ScatPixelSizeXY/2,ScatPixelThickness/2); //size
for(size_t i_Scat=0; i_Scat < NbOfScatters;i_Scat++)
{
if (i_Scat>0)
{
XScat=Distance_Scatter*cos(pi/3*i_Scat);
YScat=Distance_Scatter*sin(pi/3*i_Scat);
}
else
{
XScat=0.0;
YScat=0.0;
}
}
}

```

```

XScat= -ScatterSizeXY/2 + XScat + ScatPixelSizeXY/2;
YScat= -ScatterSizeXY/2 + YScat + ScatPixelSizeXY/2;
for(size_t ix=0; ix < N_X_Pixel_Scat;ix++)
{
for(size_t iy=0; iy < N_Y_Pixel_Scat;iy++)
{
sprintf(IDS,"%d",i_Pixel_Scat+1);
logicScatter[i_Pixel_Scat] = new G4LogicalVolume(solidScatterPixel, //its solid
                                                ScatterMaterial, //its material
                                                IDS); //its name

xp= XScat + ix*ScatPixelSizeXY*1.001;
yp= YScat + iy*ScatPixelSizeXY*1.001;
zp= ZScat;

G4cout<< "Xs= " << xp/mm << " Ys= " << yp/mm << " Zs = " << zp/mm<< G4endl;

physiScatter[i_Pixel_Scat] = new G4PVPlacement(0, //no rotation
                                                G4ThreeVector(xp,yp,zp), //its position
                                                logicScatter[i_Pixel_Scat], //its logical volume
                                                IDS, //its name
                                                logicCamera, //its mother
                                                true, //no boolean operat
                                                0); //copy number

i_Pixel_Scat++;
}
}

```

```

    }
}
}
//
// Absorber
//
if (AbsorberThickness > 0.)
{
    G4int i_Pixel_Abs=0;
    char IDA[20];
    G4double XAbs, YAbs, ZAbs;
    ZAbs = ZScat + Distance_Z;
    solidAbsorberPixel = new G4Box("Absorber", //its name
        AbsPixelSizeXY/2, AbsPixelSizeXY/2, AbsPixelThickness/2);
for(size_t i_Abs=0; i_Abs<NbOfAbsorbers;i_Abs++)
{
    if (i_Abs>0)
    {
        XAbs=Distance_Absorber*cos(pi/3*i_Abs);
        YAbs=Distance_Absorber*sin(pi/3*i_Abs);
    }
    else
    {

```

```

XAbs=0.0;

YAbs=0.0;

}

XAbs= -AbsorberSizeXY/2 + XAbs + AbsPixelSizeXY/2;

YAbs= -AbsorberSizeXY/2 + YAbs + AbsPixelSizeXY/2;

for(size_t ix=0; ix <N_X_Pixel_Abs;ix++)

{

for(size_t iy=0; iy <N_Y_Pixel_Abs;iy++)

    {

    sprintf(IDA, "%d",i_Pixel_Abs+252+1);

logicAbsorber[i_Pixel_Abs] = new G4LogicalVolume(solidAbsorberPixel,    //its solid

                                                AbsorberMaterial,    //its material

                                                AbsorberMaterial->GetName()); //name

    xp= XAbs + 1.001*AbsPixelSizeXY*ix;

    yp= YAbs + 1.001*AbsPixelSizeXY*iy;

    zp= ZAbs;

G4cout<<" Ya= " << xp/mm <<" Ya=" <<yp/mm<<" Za = " <<zp/mm<<G4endl;

physiAbsorber[i_Pixel_Abs] = new G4PVPlacement(0    //no rotation

                                                G4ThreeVector(xp,yp,zp),    //its position

                                                logicAbsorber[i_Pixel_Abs], //its logical volume

                                                IDA,    //its name

                                                logicCamera,    //its mother

                                                true,    //no boolean operat

```

```

                                0);           //copy number

    i_Pixel_Abs++;
        }
    }
}
}

PrintCameraParameters();

// Visualization attributes
//

logicWorld->SetVisAttributes (G4VisAttributes::Invisible);

G4VisAttributes* simpleBoxVisAtt= new G4VisAttributes(G4Colour(1.0,1.0,1.0));
simpleBoxVisAtt->SetVisibility(false);

logicCamera->SetVisAttributes(simpleBoxVisAtt);

{G4VisAttributes* simpleBoxVisAtt= new G4VisAttributes(G4Colour(0.5,1.0,0.15));
simpleBoxVisAtt->SetVisibility(false);

    delete logicCamera->GetVisAttributes();

logicCamera->SetVisAttributes(simpleBoxVisAtt);}

{G4VisAttributes* atb= new G4VisAttributes(G4Colour(1.0,.5,0.1));
atb->SetForceSolid(true);

for(int i=0;i<NbOfScat_Pixel;i++)
    {

logicScatter[i]->SetVisAttributes(atb);

    }
}

```

```

}
{G4VisAttributes* atb= new G4VisAttributes(G4Colour(0.5,2.0,0.1));
atb->SetForceSolid(true);
for(int i=0;i<NbOfAbs_Pixel;i++)
{
logicAbsorber[i]->SetVisAttributes(atb);
}
}
return physiWorld;
}
//=====

void DetectorConstruction::PrintCameraParameters()
{
G4cout << "\n-----"
<< "\n--> The camera is " << NbOfScat_Pixel << " scatter pixels of: [ "
<< ScatterThickness/mm << "mm of " << ScatterMaterial->GetName()
<< " + "
<< NbOfAbs_Pixel<<" absorber pixels of: ["
<<AbsorberThickness/mm << "mm of " << AbsorberMaterial->GetName()
<< "\n-----\n";
}
//=====

```

```

void DetectorConstruction::SetScatterMaterial(G4String materialChoice)
{
    // search the material by its name

    G4Material* pttoMaterial = G4Material::GetMaterial(materialChoice);
    if (pttoMaterial) ScatterMaterial = pttoMaterial;
}

//=====

void DetectorConstruction::SetAbsorberMaterial(G4String materialChoice)
{
    // search the material by its name

    G4Material* pttoMaterial = G4Material::GetMaterial(materialChoice);
    if (pttoMaterial) AbsorberMaterial = pttoMaterial;
}

//=====

void DetectorConstruction::SetGapMaterial(G4String materialChoice)
{
    // search the material by its name

    G4Material* pttoMaterial = G4Material::GetMaterial(materialChoice);
    if (pttoMaterial) GapMaterial = pttoMaterial;
}

//=====

void DetectorConstruction::SetCameraSizeXY(G4double val)
{

```

```

// change Scatter thickness and recompute the Cameraimeter parameters
CameraThickness = val;
}

//=====

void DetectorConstruction::SetScatterThickness(G4double val)
{
// change Scatter thickness and recompute the Cameraimeter parameters
ScatterThickness = val;
}

//=====

void DetectorConstruction::SetAbsorberThickness(G4double val)
{
// change Absorber thickness and recompute the Cameraimeter parameters
AbsorberThickness = val;
}

//=====

void DetectorConstruction::SetGapThickness(G4double val)
{
// change Gap thickness and recompute the Cameraimeter parameters
GapThickness = val;
}

//=====

void DetectorConstruction::SetScatterDistance(G4double val)

```

```

{
    // change the transverse size and recompute the Cameraimeter parameters
    Distance_Scatter = val;
}

void DetectorConstruction::SetAbsorberDistance(G4double val)
{
    // change the transverse size and recompute the Cameraimeter parameters
    Distance_Absorber = val;
}

//=====

#include "G4RunManager.hh"

void DetectorConstruction::UpdateGeometry()
{
    G4RunManager::GetRunManager()->DefineWorldVolume(ConstructCamera());
}

```

APPENDIX C
AN EXAMPLE OF IMAGE RECONSTRUCTION CODES

```
global E_LaBr3 Tot_w_LaBr3 ph_ab_LaBr3 density_LaBr3 Height_A Height_S f0
NDetectors V_Detector V_Center width_X width_Y NB NBZ V4

global xs ys zs NbOfScatters Height_S Height_A XYZ Part1_S Part1_A

global N1 N2 E1 E2 NbOfEvents_OS

[E_LaBr3 Coh_LaBr3 Incoh_LaBr3 ph_ab_LaBr3 Nu_p_LaBr3 Ele_p_LaBr3 Tot_w_LaBr3
Tot_wo_LaBr3]=textread('LaBr3_ph.m','%f%f%f%f%f%f%f%f', 94);
[N01 E01 N02 E02]=textread('line_2.2MeV_2', '%d%f%d%f', 2000000);

N1=N01;

N2=N02;

E1=E01;

E2=E02;

NEV=numel(N1);

NbOfScatters=252;

density_LaBr3=5.2;

NbOfAbsorbers = 7;

N_iterative=20;

width_X=6*0.4;

width_Y=6*0.4;

NDetectors=252*2;

Height_A=2.54;

Height_S=1.3;

V4=[[width_X/2, width_Y/2,0]
```

```

        [-width_X/2, width_Y/2,0]
        [-width_X/2,-width_Y/2,0]
        [ width_X/2,-width_Y/2,0]];
[Vscat Vabs V_Center]=Dposition();
V_Detector=[Vscat
            Vabs];
E_Source=2200/1000;
LX=20.;
LY=20.;
LZ=5.;
NB=51;
NBZ=1;
f=zeros(NB,NB,NBZ)+1;
f0=f;
ff=zeros(N_iterative,NB,NB,NBZ);
SUM1=zeros(NB,NB,NBZ);
NN=floor(NB/2);
NNZ=floor(NBZ/2)
xs=[-NN:NN]*LX/NB;
ys=[-NN:NN]*LY/NB;
zs=Vscat(1,3)-15+[-NNZ:NNZ]*LZ/NBZ;
XYZ=zeros(NB*NB*NBZ,3);
ii=1;

```

```

for iz=1:NBZ
    for iy=1:NB
        for ix=1:NB
            XYZ(ii,:)=[xs(ix),ys(iy),zs(iz)];
            ii=ii+1;
        end
    end
end

SUM1=real(SUM_DEN(E_Source))

[P_Scat1 P_Abs1]=SUM_32P1(E_Source);
ND=find(abs(ceil(N01/36)-ceil(N02/36))>=1);
N1=N01(ND);
N2=N02(ND);
E1=E01(ND);
E2=E02(ND);
NbOfEvents=numel(ND);
NbOfOsEV=1000;
NbOfSet=floor(NbOfEvents/NbOfOsEV);
Part1_S=P_Scat1(ND,:);
Part1_A=P_Abs1(ND,:);
T_total=0.0;
for I_iterative=1:N_iterative
    for i_Set=1:NbOfSet

```

```

NbOfEvents_OS=NbOfOsEV;
Index_Start=(i_Set-1).*NbOfOsEV+1;
Index_End=i_Set.*NbOfOsEV+1;
Part1_S=P_Scat1(ND(Index_Start:Index_End),:);
Part1_A=P_Abs1(ND(Index_Start:Index_End),:);
N1=N01(ND(Index_Start:Index_End));
N2=N02(ND(Index_Start:Index_End));
E1=E01(ND(Index_Start:Index_End));
E2=E02(ND(Index_Start:Index_End));
SUM32=SUM_32P2_OS(E_Source)
f=f0./SUM1.*SUM32;
f0=f.*NbOfOsEV./sum(sum(sum(f)))

```

end

```
DF(I_iterative)=sum(sum(sum(abs(f-f00))));
```

```
    f00=f;
```

```
ff(I_iterative, :, :, :)=f;
```

```
T_total=T_total+toc;
```

end

APPENDIX D
AN EXAMPLE OF RESPONSE MATRIXES GENERATION CODES

```
function Coeff=SUM_DEN(E_Source)

global V_Detector E0 E_LaBr3 NB NBZ xs ys zs Tot_w_LaBr3 ph_ab_LaBr3 density_LaBr3
Radius Height_A Height_S V_Center

global J_Br_Q J_La_Q Q XYZ NbOfScatters width_X width_Y V_Second

mc2=0.511;

sc=137.0387;

width=width_X;

NEB=10;

Nf=9;

Coeff=zeros(NB,NB,NBZ);

D1=[36:36:252]-18;

D2=D1+252;

D=[D1,D2];

mu_s_in=mu(E_Source);

    for i=1:14-1

        j0=i+1;

        for j=j0:14

            IEE=1;

            while IEE<3

                if IEE==1

                    i_Scat=D(i);

                    i_Sec=D(j);
```

```

        else

            i_Scat=D(j);

            i_Sec=D(i);

        end

        IEE=IEE+1;

        V_Scatter=V_Center(ceil(i_Scat/36),:);

        V_Second=V_Center(ceil(i_Sec/36),:);

    if i_Scat<NbOfScatters

        height_scat=Height_S;

    else

        height_scat=Height_A;

    end

    if i_Sec<NbOfScatters

        height_sec=Height_S;

    else

        height_sec=Height_A;

    end

    V1=[V_Scatter
        V_Second];

    V2=[V_Second
        V_Scatter];

    ID=[i_Scat
        i_Sec];

```

```

LSA=PassLengthNDE(V1,V2,ID);
Ls_out = LSA(1);
La_in = LSA(2);
VSout=V_Second-V_Scatter;
Ls_in=PassLengthN3DNDE(V_Scatter,i_Scat);
P_S_in=exp(-mu_s_in.*Ls_in).*(Ls_in>0)+(1-exp(-
    mu_s_in.*height_scat)).*(Ls_in==0);
V_Sin=[V_Scatter(1)-XYZ(:,1),V_Scatter(2)-XYZ(:,2),V_Scatter(3)-XYZ(:,3)];
V_SinMVSout=[V_Sin(:,1)*VSout(1),V_Sin(:,2)*VSout(2),V_Sin(:,3)*VSout(3)];
cos_theta_S=(sum(V_SinMVSout,2)./sqrt(sum(V_Sin.*V_Sin,2).*sum(VSout.*VSout)));
alpha0=E_Source/.511;
Nff=find(cos_theta_S==1);
if numel(Nff)>0
cos_theta_S(Nff)=0.99999;
end
er=1.0./(1+alpha0.*(1-cos_theta_S));
E_Scat=E_Source.*er;
P1=sqrt(E_Source.*E_Source+E_Scat.*E_Scat
+2.0*E_Source.*E_Scat.*cos_theta_S);
pz=-(E_Source-E_Scat-E_Source.*E_Scat.*(1-cos_theta_S)/mc2)./P1;
q=abs(pz*sc);
NS=find(q<=100);
NL=find(q>100);

```

```

J(NS)= interp1q(Q',J_La_Q',q(NS))+ 3.*interp1q(Q',J_Br_Q',q(NS));

J(NL) = 0.0;

st=sin(acos(cos_theta_S));

ver=1./er;

sigma_KN_DB= er.*er.*(er+ver-st.*st).*E_Source./P1.*J'./E_Scat;

CrossS=sigma_KN_DB.*st/19.0;

mu_s_out=mu(E_Scat);

P_S_out=exp(-mu_s_out.*Ls_out);

P_A_in=exp(-mu_s_out.*La_in).*(La_in>0)+(1-exp(-
                    mu_s_out.*height_sec)).*(La_in==0);

E000=E_Scat;

alpha=E000/.511;

height=height_scat;

Dist_sqoo=sum(VSin.*VSin,2);

cos_theta_inoo=(VSin(:,3)./sqrt(Dist_sqoo));

Omega_Top=width*height*sqrt(1-cos_theta_inoo.*cos_theta_inoo);

Omega_Side=width*width*abs(cos_theta_inoo);

Omega_in=(Omega_Top+Omega_Side)*36./Dist_sqoo;

%-----

height=height_sec;

Vin=V_Second-V_Scatter;

Dist_sq=sum(Vin.*Vin);

cos_theta_in=(Vin(:,3)/sqrt(Dist_sq));

```

```

Omiga_Side=width.*height.*sqrt(1-cos_theta_in.*cos_theta_in);
Omiga_Top=width.*width.*abs(cos_theta_in);
Omiga_out=(Omiga_Top+Omiga_Side)*36./Dist_sq;
Part1=P_S_out.*P_A_in.*Omiga_out;
E02=zeros(NB*NB*NBZ,NEB);
for ieng=1:NEB
    Eo2(:,ieng)=ieng.*E_Scat/NEB;
end
for m=1:NEB
    E_Sec=Eo2(:,m);
    E_out=E_Scat-E_Sec;
    Vp=(E_Scat./(1+2*alpha)<=E_out).*(E_out<E00);
    NP= find(Vp==1);
    if numel(NP) >0
        E00=E_Scat(NP);
        E_outp=E_out(NP);
        alphap=alpha(NP);
        cos_theta_A_out0=1.-(E00-E_outp)./(E_outp.*alphap);
        theta_A_out0=acos(cos_theta_A_out0);
        CrossS_Sec0=DBKNN(theta_A_out0,E00,E_outp);
        DV=sqrt(sum(VSout.*VSout));
        theta_p=acos(VSout(3)./DV);
        DD=sqrt(VSout(1)*VSout(1)+VSout(2)*VSout(2));
    end
end

```

```

if DD==0
    phi_p=0.0;
else
    cos_phi_p=VSout(1)./DD;
    phi_p=acos(cos_phi_p);
    phi_p=phi_p.*(VSout(2)>=0)+(2*pi-phi_p).*(VSout(2)<0);
end

NNP=numel(NP);
phi_pV=zeros(NNP,1);
theta_pV=zeros(NNP,1);
phi_pV(:,1)=phi_p;
theta_pV(:,1)=theta_p;

[theta_A_out,phi_A_out]=angleprojectN(Nf,theta_A_out0,theta_pV,phi_pV);
phi_A_out=phi_A_out/180*pi;
XA=sin(theta_A_out).*cos(phi_A_out);
YA=sin(theta_A_out).*sin(phi_A_out);
ZA=cos(theta_A_out);
IDp=zeros(NNP,Nf,1);
V1p=zeros(NNP,Nf,3);
V2=[XA,YA,ZA];
for ii=1:Nf
    V1p(:,ii,1)=V_Second(1);
    V1p(:,ii,2)=V_Second(2);

```

```

V1p(:,ii,3)=V_Second(3);
IDp(:,ii)=i_Sec;
end

V1=reshape(V1p,NNP*Nf,3);
ID=reshape(IDp,NNP*Nf,1);
La_out0= PassLengthN(V1,V2+V1,ID);
La_out=reshape(La_out0,NNP,Nf);
Coefexp=zeros(NNP,Nf);
mu_A_out=mu(E_outp);
for iii=1:Nf
    Coefexp(:,iii)=mu_A_out.*La_out(:,iii);
end
P_A_outp=sum(exp(-Coefexp),2)*2*pi/Nf;
P_A_out=Vp;
P_A_out(NP)=P_A_outp;
CrossS_Sec=Vp;
CrossS_Sec(NP)=CrossS_Sec0;

% twice Compton Scattering
Part1_S=Part1.*CrossS_Sec.*P_A_out;
else
    Part1_S=zeros(NB*NB*NbZ,1);
end

% Once Compton Scattering Once photoelectric absorbing

```

```

CrossS_A=interp1q(E_LaBr3,ph_ab_LaBr3,E_Scat);
Part1_A=Part1.*CrossS_A.*E_reps(E_Scat,E_Sec, i_Sec);
% twice Comptom Scattering
pp=Omiga_in.*CrossS;
F1=P_S_in.*reshape(pp,NB,NB,NBZ);
P_Scat_Scat=F1.*reshape(Part1_S,NB,NB,NBZ);
% Once Compton Scattering Once photoelectric absorbing
P_Scat_Abs=F1.*reshape(Part1_A,NB,NB,NBZ);
Coeff=Coeff+P_Scat_Scat+P_Scat_Abs;

end

end

end

end

end

```

LIST OF REFERENCES

- [1] B. Aschenbach, 1985, Rep. Prog. Phys., 48, 579
- [2] L.P. Van Speybroeck, 1987, Astroph. Lett. Communications 26, 127
- [3] E. Caroli, J.B. Stephen, Di Cocco, G., Natalucci, L., Spizzichino, A.: 1987, SSR, 45, 349
- [4] F. Makino, Astro-C team: 1987, Institute of Space and Astronautical Science, Tokyo, , Research Note No. 326
- [5] V. Schönfelder, et al. "Instrument description and performance of the Imaging Gamma-Ray Telescope COMPTEL aboard the Compton Gamma-Ray Observatory," Astrophysical Journal Supplement Series, vol. 86, pp. 657–692, June 1993.
- [6] M. Forot, et al." "The Astrophysical Journal (ApJ), 668:1259-1265, 2007"
- [7] R. W. Todd, J. M. Nightingale, and D. B. Everett, "A proposed gamma camera," Nature, vol. 251, no. 5471, pp. 132–134, 1974
- [8] W.L. Rogers, N.H. Clinthorne and A.Bokozdynia, "Compton Cameras for Nuclear Medical Imaging", Book Chapter v3 (2001)
- [9] M. Singh, "An electronically collimated gamma camera for single photon emission computed tomography. Part I: Theoretical considerations and design criteria," Medical Physics, vol. 10, no. 4, pp. 421–427, 1983.
- [10] A. Braem, et al., "Novel design of a parallax free Compton enhanced PET scanner", NIM. 525, pp. 268, 2004
- [11] M. Burks, et al., "Imaging Performance of the Si/Ge Hybrid Compton Imager," Nuclear Science Symposium Conference Record, 2005 IEEE, vol. 1, pp. 6–10, 2005.
- [12] R. Orito, et al., "Electron-tracking Compton telescope with a gaseous TPC", 2005 IEEE Nuclear Science Symposium Conference Record N14-53
- [13] J.B. Martin, et al., "A ring Compton scatter camera for imaging medium energy gamma rays," IEEE Transactions on Nuclear Science, vol. 40, no. 4, pp. 972–978, 1993
- [14] Y.F. Du, Z. He, G. F. Knoll, D. K. Wehe, and W. Li, "Evaluation of a Compton scattering camera using 3-D position sensitive CdZnTe detectors," Nuclear Instruments and Methods in Physics Research, Section A: Accelerators, Spectrometers, Detectors and Associated Equipment, vol. 457, no. 1-2, pp. 203–211, 2001.
- [15] M. S. Tom Hebert, Richard Leahy, "Three-dimensional maximum-likelihood reconstruction for an electronically collimated single-photon-emission imaging system," Optical Society of America, vol. 7, no. 7, pp. 1305–1313, 1990.

- [16] F. Zhang, Z. He, and C. E. Seifert, "A Prototype Three-Dimensional Position Sensitive CdZnTe Detector Array" IEEE TRANSACTIONS ON NUCLEAR SCIENCE, 54, 843, 2007
- [17] E.V.D. van Loef, et al "Scintillation properties of LaBr₃ crystal: fast, efficient and high-energy resolution scintillators" NIM. A 486, pp254-258, 2002.
- [18] G. Bizarri, J. T. M. de Haas, P. Dorenbos, and C. W. E. van Eijk, "Scintillation Properties of Ø 1 1 Inch LaBr₃ : 5%Ce Crystal" IEEE Trans. Nucl. Sci., vol. 53, no. 2, pp.615-619, April, 2006.
- [19] Yuxin Feng, R. S. Detwiler J. E. Baciak, and W. Kernan, "Optimized Geometry and Limitations of Compton Cameras with LaBr₃", Nuclear Science Symposium Conference Record, 2007. NSS '07. IEEE Vol. 2, pp. 1227-1233
- [20] K. Pinkau, "Die Messung solare und atmosphärischer Neutronen", Zeitschrift Naturforschung Teil A, Vol. 21, p.2100, 1966
- [21] V. Schonfelder, A. Hirner, K. Schneider, "A telescope for soft gamma ray astronomy", Nucl. Instrum. Methods, Vol. 107, p. 385 – 394, 1973
- [22] R. W. Todd, J. M. Nightingale, and D. B. Everett, "A proposed gamma camera," Nature, vol. 251, no. 5471, pp. 132–134, 1974.
- [23] J.W. LeBlanc, N.H. Clinthorne, C.-H. Hua, E. Nygard, W.L. Rogers, D.K. Wehe, P. Weilhammer, S.J. Wilderman, "C-SPRINT: a prototype Compton camera system for low energy gamma ray imaging", IEEE Trans. Nucl. Sci., vol. 45, no. 3, pp. 943-949, 1998.
- [24] E. A. Wulf, B. F. Philips, J. D. Kurfess, E. I. Novikova, and C. M. Fitzgerald, "A Silicon Compton Imager," Nuclear Science Symposium Conference Record, 2005 IEEE, vol. 1, pp. 1–5, 2005.
- [25] S. Chelikani, J. Gore, G. Zubal, "Optimizing Compton camera geometries", Physics in Medicine and Biology, Volume 49, Issue 8, pp. 1387-1408, 2004.
- [26] E.V.D. van Loef, et al "Scintillation properties of LaBr₃ crystal: fast, efficient and high-energy-resolution scintillators" Nucl. Instrum. Methods. A 486, pp254-258, 2002.
- [27] G. Bizarri, J. T. M. de Haas, P. Dorenbos, and C. W. E. van Eijk, "Scintillation Properties of Ø 1 1 Inch LaBr₃: 5%Ce Crystal" IEEE Trans. Nucl. Sci., vol. 53, no. 2, pp. 615-619, April, 2006.
- [28] R. D. Evans, *The atomic nucleus*. New York: McGraw-Hill, 1955.
- [29] R. Ribberfors, "Relationship of the relativistic Compton cross section to the momentum distribution of bound electron states," *Physical Review B*, vol. 12, pp. 2067–2074, 1975.

- [30] F. Biggs, L.B. Mendelsohn and J.B. Mann, “Hartree-Fock Compton profiles for the elements,” *At. Data and Nucl. Data Tables*, vol. 16, pp. 201-309, 1975.
- [31] M. Singh, “An electronically collimated gamma camera for single photon emission computed tomography. Part I: Theoretical considerations and design criteria,” *Medical Physics*, vol. 10, no. 4, pp. 421–427, 1983.
- [32] C.E. Ordonez, W. Chang, and A. Bolozdynya, “Angular Uncertainties due to Geometry and Spatial Resolution in Compton Cameras”, *IEEE Transactions on Nuclear Science*, vol. 46, issue 4, pp. 1142-1147, 1999
- [33] Mertz, L., Young, in "Proc. Int. Conf. on Opt. Instr. 1961
- [34] Dicke, R.H.: 1968, *APJL*, 153, L101
- [35] Ables, J.G.: 1968, *Proc. Astron. Soc. Australia*, 1, 172
- [36] Fenimore, E.E., Cannon, T.M.: 1978, *APO*, 17, 337
- [37] Gunson, J., Polychronopoulos, B.: 1976, *MNRAS*, 177, 485
- [38] Baumert, L.D.: 1971, *Lecture Notes in Mathematics No. 182: Cyclic*
- [39] Hall, M.: 1967, *Combinational Theory*, (Waltham: Blaisdell)
- [40] Peterson, W.W.: 1961, *Error Correcting Codes*, (Massachusetts: : MIT Press)
- [41] Hammersley, A.P.: 1986, "The Reconstruction of Coded-mask Data under Conditions Realistic to X-Ray Astronomy Observations", Ph.D. Thesis, University of Birmingham
- [42] Hammersley, A., Ponman, T., Skinner, G.K.: 1992, *NIM*, A311, 585
- [43] Smith L.E., Chen, C. Wehe D.K., *He Z. NIM*, A462, 576, 2001
- [44] Lee W., Wehe D. *NIM.*, A 579, p. 200-204, 2007
- [45] M. J. Cree and P. J. Bones, “Towards direct reconstruction from a gamma camera based on Compton scattering,” *IEEE Transactions on Medical Imaging*, vol. 13, no. 2, pp. 398–407, 1994.
- [46] R. Basko, G. L. Zeng, and G. T. Gullberg, “Application of spherical harmonics to image reconstruction for the Compton camera,” *Physics in Medicine and Biology*, vol. 43, no. 4, pp. 887–894, 1998.
- [47] R. D. Evans, *The atomic nucleus*. New York: McGraw-Hill, 1955.
- [48] T. Tomitani and M. Hirasawa, “Image reconstruction from limited angle Compton camera data,” *Physics in Medicine and Biology*, no. 12, pp. 2129–2145, 2002.

- [49] M. Singh, “An electronically collimated gamma camera for single photon emission computed tomography. Part I: Theoretical considerations and design criteria,” *Medical Physics*, vol. 10, no. 4, pp. 421–427, 1983.
- [50] M. S. Tom Hebert, Richard Leahy, “Three-dimensional maximum-likelihood reconstruction for an electronically collimated single-photon-emission imaging system,” *Optical Society of America*, vol. 7, no. 7, pp. 1305–1313, 1990.
- [51] J. M. Fitzpatrick and M. Sonka, *Handbook of Medical Imaging, Volume 2. Medical Image Processing and Analysis*. SPIE Press, 2000
- [52] H. M. Hudson and R. S. Larkin, “Accelerated image reconstruction using ordered subsets of projection data,” *IEEE Transactions on Medical Imaging*, vol. 13, no. 4, pp. 601–609, 1994.
- [53] S.M. Kim, J.S. Lee and S.J. Lee “Fully Three-Dimensional Image Reconstruction for Compton Imaging Using Ordered Subsets of Conical Projection Data”, *IEEE Nuclear Science Symposium Conference Record*, M13-273, 2007
- [54] E.E. Fenimore, and T.M. Cannon, “Coded aperture imaging: many holes make light work”, *Optical Engineering*, 19, pp. 283-289, 1980.
- [55] E.E. Fenimore, and T.M. Cannon, “Coded aperture imaging with uniformly redundant arrays”, *Applied Optics*, 17, pp. 4344-4352, 1978.
- [56] J. R. Driscoll and D. M. Healy, “Computing Fourier Transforms and Convolutions on the 2-Sphere,” *Advances in Applied Mathematics*, vol. 15, no. 2, pp. 202–250, 1994.
- [57] O. Guillot-Noël, J. T. M. de Haas, P. Dorenbos, C. W. E. van Eijk, K. W. Krämer, and H. U. Güdel, *J. Lumin.* 85, 21 (1999).
- [58] E. V. D. van Loef, P. Dorenbos, and C. W. E. van Eijk, *Appl. Phys. Lett.* 79, 1573 (2001).
- [59] B. Morosin, *J. Chem. Phys.* 49 (7) (1968) 3007.
- [60] W.M. Higgins et al. *J. Crystal Growth* 287 390. 2006
- [61] G. Bizarri, J. T. M. de Haas, P. Dorenbos, and C. W. E. van Eijk, *Phys. Rev. B* 75, pp. 184302, 2007
- [62] K. S. Song and R. T. Williams, *Self-trapped Excitons*, Springer series in Solid State Sciences 105 (Springer- Verlag, Berlin, 1993).
- [63] *SGC Br Technical Note 1207*
- [64] E Series User Manual, National Instruments Corporate Headquarters
- [65] W. J. Kernan, “Self-Activity in Lanthanum Halides,” *IEEE Trans. Nucl. Sci.*, vol. 53, no. 1, pp. 395-399, Feb. 2006.

- [66] S.J. Wilderman, W. L. Rogers, G. F. Knoll, and J. C. Engdahl, “Fast algorithm for list mode back-projection of Compton scatter camera data”, *IEEE Trans. Nucl. Sci.* 45, no. 3, 957-61, 1998
- [67] D. Xu, Z. He, C. E. Lehner, and F. Zhang, “4-pi Compton imaging with single 3D position sensitive CdZnTe detector,” *Proceedings SPIE*, vol. 5540, pp. 144–155, 2004.
- [68] M. J. Cree and P. J. Bones, “Towards direct reconstruction from a gamma camera based on Compton scattering,” *IEEE Transactions on Medical Imaging*, vol. 13, no. 2, pp. 398–407, 1994.
- [69] T. Tomitani and M. Hirasawa, “Image reconstruction from limited angle Compton camera data,” *Physics in Med. and Bio.*, no. 12, pp. 2129–2145, 2002.
- [70] D.L. Gunter, L. Mihailescu, M. Burks, K. A. Vetter, “Filtered Backprojection Algorithm for Compton Telescopes”, *IEEE NSS-MIC*, pp. J03-47, 2005
- [71] R. W. Todd, J. M. Nightingale, and D. B. Everett, “A proposed gamma camera,” *Nature*, vol. 251, no. 5471, pp. 132–134, 1974..
- [72] M. Singh, “An electronically collimated gamma camera for single photon emission computed tomography. Part I: Theoretical considerations and design criteria,” *Medical Physics*, vol. 10, no. 4, pp. 421–427, 1983.
- [73] Y. F. Du, Z. He, G. F. Knoll, D. K. Wehe, and W. Li, “Evaluation of a Compton scattering camera using 3-D position sensitive CdZnTe detectors,” *Nucl. Instrum. Methods A*, vol. 457, no. 1-2, pp. 203–211, 2001.
- [74] E.E. Fenimore, T.M. Cannon, "Coded aperture imaging with uniformly redundant arrays (ET)," *APO*, 17, pp. 337, 1978
- [75] M. Forot, et al. "High-Energy Particles in the Wind Nebula of Pulsar B1509-58 as seen by INTEGRAL," *ApJ*, vol.668, pp.1259, 2007
- [76] L. E. Smith, C. Chen, D. K. Wehe, and Z. He, “Hybrid collimation for industrial gamma-ray imaging: combining spatially coded and Compton aperture data,” *Nucl. Instrum. Methods A*, vol. 462, 576, 2001.
- [77] W. Lee, and D. Wehe, “Hybrid gamma ray imaging Model and results,” *Nucl. Instrum. Methods A*, vol.579, pp.200-204, 2007.
- [78] E.V.D. van Loef, et al “Scintillation properties of LaBr₃ crystal: fast, efficient and high-energy-resolution scintillators” *Nucl. Instrum. Methods A*, vol.486, pp. 254-258, 2002.
- [79] A. Nassalski, M. Kapusta, T. Batsch, D. Wolski, D. Möckel, W. Enghardt, M. Moszyński, “Comparative study of scintillators for PET/CT detectors”, *IEEE Trans. Nucl. Sci.* 45 (1998), no. 3, pp. 957-61.

- [80] C.E. Ordonez, W. Chang, A. Bolozdynya, "Angular uncertainties due to geometry and spatial resolution in Compton cameras", *IEEE Nucl Sci. Symp.* vol: 3, pp. 1535-1540, 1998
- [81] C. E. Ordonez, A. Bolozdynya, and W. Chang "Dependence of Angular Uncertainties on the Energy Resolution of Compton Cameras", *IEEE Nucl. Sci. Symp.* , vol. 2, pp. 1122-1125, 1998
- [82] R. Ribberfors, "Relationship of the relativistic Compton cross section to the momentum distribution of bound electron states," *Physical Review B*, vol. 12, pp. 2067–2074, 1975
- [83] C. E. Ordonez, A. Bolozdynya, and W. Chang, "Doppler broadening of energy spectra in Compton cameras", 1997 *IEEE Nucl Sci. Symp.* vol. 2, pp. 1361-1365, 1998.
- [84] W. J. Kernan, "Self-Activity in Lanthanum Halides," *IEEE Trans. Nucl. Sci.*, vol. 53, no. 1, pp. 395-399, Feb. 2006.
- [85] S.J. Wilderman, W. L. Rogers, G. F. Knoll, and J. C. Engdahl, "Fast algorithm for list mode back-projection of compton scatter camera data", *IEEE Trans. Nucl. Sci.* 45, no. 3, 957-61, 1998
- [86] D. Xu, Z. He, C. E. Lehner, and F. Zhang, "4-pi Compton imaging with single 3D position sensitive CdZnTe detector," *Proceedings SPIE*, vol. 5540, pp. 144–155, 2004.
- [87] M. J. Cree and P. J. Bones, "Towards direct reconstruction from a gamma camera based on Compton scattering," *IEEE Transactions on Medical Imaging*, vol. 13, no. 2, pp. 398–407, 1994.
- [88] T. Tomitani and M. Hirasawa, "Image reconstruction from limited angle Compton camera data," *Physics in Med. and Bio.*, no. 12, pp. 2129–2145, 2002.
- [89] D.L. Gunter, L. Mihailescu, M. Burks, K. A. Vetter, "Filtered Backprojection Algorithm for Compton Telescopes", *IEEE NSS-MIC*, pp. J03-47, 2005
- [90] P. Kostelec and D. Rockmore, FFTs on the Rotation Group, Santa Fe Institute's Working Papers series, Paper #: 03-11-060, 2003.
- [91] M. S. Tom Hebert, Richard Leahy, "Three-dimensional maximum-likelihood reconstruction for an electronically collimated single-photon-emission imaging system," *Optical Society of America*, vol. 7, no. 7, pp. 1305–1313, 1990.
- [92] A. Johansson et al., "The use of an active coded aperture for improved directional measurements in high energy gamma-ray Astronomy," *IEEE Trans. Nucl. Sci.*, vol. NS-27, pp. 375, 1980.
- [93] T. Tomitani and M. Hirasawa, "Image reconstruction from limited angle Compton camera data," *Physi.in Med. and Bio.*, no. 12, pp. 2129–2145, 2002.

- [94] P. Kostelec and D. Rockmore, FFTs on the Rotation Group, Santa Fe Institute's Working Papers series, Paper #: 03-11-060, 2003.
- [95] D. Olsen, Ø. Bruland, G. Frykholm, I. Norderhaug, "Proton therapy – A systematic review of clinical effectiveness", *Radiotherapy and Oncology*, Volume 83, Issue 2, pp. 123-132, 2007
- [96] Schaffner, B; Pedroni, E. The precision of proton range calculations in proton radiotherapy treatment planning: Experimental verification of the relation between CT-HU and proton stopping power. *Phys Med Biol*. 1998; 43, pp.1579–1592.
- [97] Fassò, A; Ferrari, A; Ranft, J; Sala, PR. In: Kling A, Barao F, Nakagawa M, Tavora L, Vaz P. , editors. FLUKA: Status and prospective for hadronic applications; Proc Monte Carlo 2000 Conference; Lisbon. Berlin: Springer-Verlag; 2001. pp. 955–960.
- [98] Kitwanga, SW; Leleux, P; Lipnik, P; Vanhorenbeeck, J. "Production of ^{13}N radioactive nuclei from $^{13}\text{C}(p,n)$ or $^{16}\text{O}(p,\alpha)$ reactions", *Phys Rev C*. 1989;40:35–83.
- [99] Paans, AMJ; Schippers, JM. "Proton therapy in combination with PET as monitor: A feasibility study", *IEEE Trans Nucl Sci*. 1993;40:1041–1044.
- [100] Enghardt, W; Debus, J; Haberer, T; Hasch, BG; Hinz, R; Jäkel, O; Krämer, M; Lauckner, K; Pawelke, J; Pönisch, F. "Positron emission tomography for quality assurance of cancer therapy with light ion beams", *Nucl Phys A*. 1999;654:1047–1050.
- [101] Pönisch, F; Parodi, K; Hasch, BG; Enghardt, W. "The description of positron emitter production and PET imaging during carbon ion therapy", *Phys Med Biol*. 2004;49:5217–5232.
- [102] Parodi, K; Bortfeld, T. A "filtering approach based on Gaussian-power law convolutions for local PET verification of proton radiotherapy", *Phys Med Biol*. Vol. 51, pp.1991–2009, 2006
- [103] Kuhn, A; Surti, S; Karp, JS; Raby, PS; Shah, KS, et al. "Design of a lanthanum bromide detector for time-of-flight PET", *IEEE Trans Nucl Sci*. 2004;NS-51:2550–2557.
- [104] Kuhn, A; Surti, S; Karp, JS; Muehllehner, G; Newcomer, FM, et al. "Performance assessment of pixellated LaBr₃ detector modules for TOF PET", In: Siebert A. , editor. *Proceedings of the IEEE 2004 Nuclear Science Symposium*; Rome, Italy. 2004. pp. M9–59.
- [105] S. Agostinelli, et al. "G4—a simulation toolkit", *Nuclear Instruments and Methods in Physics Research Section A: Accelerators, Spectrometers, Detectors and Associated Equipment*, Volume 506, Issue 3, 1 July 2003, Pages 250-303
- [106] <http://physics.nist.gov/PhysRefData/Xcom/Text/XCOM.html>

- [107] G. N. Ramachandran and A. V. Lakshminarayanan. Three dimensional reconstruction from radiographs and electron micrographs: Application of convolution instead of Fourier transform. Proc. Nat. Acad. Sci, Vol. 68, pp. 2236-2240, 1971.
- [108] H. Barrett, L. Parra, and T. White, "List-mode likelihood," *J. Optical Soc. Amer. A*, vol. 14, no. 11, pp.2914-2923, 1997.
- [109] L. Parra and H. H. Barrett, "Maximum-likelihood image reconstruction from list-mode data," *J. Nucl. Med.*, vol. 37, no. 5, p. 486, 1996.
- [110] <http://www2.massgeneral.org/cancer/about/providers/radiation/proton/principles.asp>

BIOGRAPHICAL SKETCH

I graduated with B.S. from Yunnan University in physics and M.S. in laser physics from Zhejiang University. After working in Physics department, Yunnan University as teacher and research scientist, I was enrolled in Ph.D. program in Institute of High Energy Physics, Chinese Academy of Sciences. I was rewarded Ph.D degree on particle and nuclear physics in 1999. Since 2005 I have been enrolled in medical physics program in Nuclear & Radiological Engineering department in University of Florida. I received M.S. in medical physics in July 2008.